Doctorate Dissertation
博士論文

The initial abundance of niobium-92 in the outer solar system

（外側太陽系におけるニオブ 92 の初生存在度）

A Dissertation Submitted for Degree of Doctor of Philosophy
December 2018

平成 30 年 12 月博士（理学）申請

Department of Earth and Planetary Science, Graduate School of Science,
The University of Tokyo

東京大学大学院理学系研究科 地球惑星科学専攻

Yuki Hibiya
日比谷　由紀

Abstract

One of the major goals of cosmochemistry is to understand the origin of short-lived radionuclides, as it is essential for constraining the time-scale and the genealogy of our solar system. Among the short-lived radionuclides, what is of particular interest to this thesis is niobium-92 (^{92}Nb). The *p*-process ^{92}Nb decays to zirconium-92 (^{92}Zr) by electron capture with a half-life of 37 million years. The system is promising chronometer for dating early solar system events accompanied by niobium and zirconium fractionation. Moreover, once the initial abundance of ^{92}Nb and its distribution in the early solar system are well established, it provides valuable constraints on the origin of *p*-process nucleosynthesis.

In order to determine the initial abundance of ^{92}Nb from one meteorite, we need to calibrate the Nb-Zr chronometer with an absolute precise U-Pb chronometer. Therefore, it is essential to establish a meteorite to which high precision U-Pb chronometer can be applied and in which the initial abundances of ^{92}Nb can be determined, the so called "*Time anchor*". One meteorite must satisfy the following conditions to tie Nb-Zr age to an absolute U-Pb chronology: (1) a precise U-Pb age can be obtained; (2) an internal Nb-Zr isochron age can be obtained; (3) a cooling rate is rapid enough to make the difference of closure temperature between the two chronometers insignificant; (4) the meteorite has not been affected by secondary alternation or exotic components that disturb the ages.

First evidence for live ^{92}Nb with the initial ^{92}Nb/^{93}Nb of $(1.6 \pm 0.3) \times 10^{-5}$ was reported in rutile in Toluca iron meteorite. Although subsequently proposed initial ^{92}Nb/^{93}Nb vary between 10^{-3} to 10^{-5}, the current paradigm is that the initial ^{92}Nb/^{93}Nb at the solar system formation is $(1.7 \pm 0.6) \times 10^{-5}$, obtained using Nb-Zr *Time anchor* NWA 4590 angrite (U–Pb age: 4557.93 ± 0.36 Ma), and also that ^{92}Nb was homogeneously distributed in the solar system. However, all of the samples previously studied for internal Nb-Zr isochron dating are thought to have originated from the inner solar system. Thus, it is still unclear whether ^{92}Nb was homogeneously distributed in the outer solar system such as the accretion regions of carbonaceous chondrites.

Northwest Africa (NWA) 6704 is a recently found achondrite having unbrecciated and fresh igneous texture. The pristine chondrite-like characteristics of this meteorite, coupled with its ancient U-Pb age (4562.76 ± 0.30 Ma), and its igneous texture different from any known achondrite make it ideal for exploring whether it is the first "*Time anchor* from the outer solar system".

The purpose of this study is to evaluate the initial abundance and distribution of ^{92}Nb in the early solar system, on the largest scale to date. To achieve this goal, the NWA 6704 ungrouped primitive achondrite has been investigated. Developing NWA 6704 as the first *Time anchor* from the outer solar system, and applying the Nb-Zr internal isochron approach, we could determine the initial abundance of ^{92}Nb in the outer solar system. This allowed us to evaluate the distribution of ^{92}Nb

between the inner and outer solar system, and to provide new constraints on the early solar system chronology and on early solar system processes related to ^{92}Nb.

In Chapter 2, we developed a new method for combined Cr-Ti isotope analysis applicable to various planetary materials. Both the utility and the validity of the method have been verified by its application to compositionally varied terrestrial and meteorite samples, including terrestrial basalt JB-1b, terrestrial peridotite JP-1, Allende carbonaceous chondrite, and Juvinas non-cumulate eucrite. The developed method enables the combined isotope analyses of 3 μg of Cr and 1.5 μg of Ti, highlighting its potential application to various types of planetary materials.

In Chapter 3, the new method developed in Chapter 2 was applied to NWA 6704, and the origin of this meteorite was investigated in terms of the petrology, geochemistry and ^{187}Re-^{187}Os and O-Cr-Ti isotope systematics. On the basis of our results, we discussed the crystallization process of NWA 6704, the nature and provenance of its parent body, and its potential utility as a "*Time anchor*". Our results indicated that the parent asteroid of NWA 6704 underwent significant but instantaneous melting followed by cooling at a high rate (1–10^2 ˚C/hour) in the initial stage but a significantly lower rate (<10^{-4}–10^{-2} ˚C/hour at below ~1100 ˚C) in the later stage owing to blanketing effect of impact ejecta piled up on the parent body. Furthermore, since the mineral assemblage includes chromite grains with high Nb/Zr, and orthopyroxene and awaruite grains with low Nb/Zr, the internal Nb-Zr isochron can be expected to be obtained. The O, Cr and Ti stable isotope compositions indicated that the parent body of NWA 6704 sampled the same reservoirs to those of carbonaceous chondrites and distinct from the reservoirs of all meteorites previously studied for internal Nb-Zr isochron dating. Consequently, the results revealed that the NWA 6704 ungrouped primitive achondrite is a viable, new "*Time anchor* from the outer solar system".

In Chapter 4, the Nb-Zr internal isochron dating was applied to NWA 6704, and the initial ^{92}Nb abundance at the start of our solar system was determined. The results yielded an initial ^{92}Nb/^{93}Nb of (2.8 ± 0.3) × 10^{-5} at the time of NWA 6704 formation (4562.76 ± 0.30 Ma), which corresponds to an initial ^{92}Nb/^{93}Nb of (3.0 ± 0.3) × 10^{-5} at the time of solar system formation. The ratio is distinctly higher than the value in the inner solar system, which significantly affects the interpretation of the Nb–Zr early solar system chronology. This value can serve as the reference point for the Nb–Zr chronometry in the outer solar system. Using the obtained value, we further investigated the nucleosynthetic origin of ^{92}Nb. The results suggested that the *ν*-process in Type II supernova (SNII) is the most probable origin for ^{92}Nb, and imply that nuclides synthesized in the last SNII were preferentially implanted or preserved in the outer solar system rather than the inner solar system.

Contents

1. Introduction

Meteorites and their components are the most ancient objects that we can study in terrestrial laboratories. Within the last decade, meteorite studies have greatly advanced our understanding of the early solar system evolution. These include the chronological constraints on the time period extending from the condensation of the oldest objects calcium-alminum-rich inclusions (hereafter, CAI) at 4567.3 ± 0.16 million years ago (Ma) (Connelly et al., 2012) to the Moon forming event at ~4.47 billion years ago (e.g., Bottke et al., 2015); the decays of ^{26}Al and ^{60}Fe as the possible heat source responsible for the early and extensive differentiation of planetesimals (e.g., Ghosh et al., 2006; McCoy et al., 2006); and the presence of freshly synthesized short-lived nuclides as a vestige from an evolved star (Goswami, 2004), which might have triggered the formation of the solar system. These current understanding of our solar system evolution is largely based on recent studies of various systematics of short-lived radionuclides, which can provide high-resolution chronology of events and astrophysical context of our solar system, and can be preserved in meteorites and their components.

The major tasks for cosmochemists are to reconstruct the evolution of the solar system by determining the (isotopic) compositions of materials through high-precision analytical chemistry, and to understand the significance of the determined compositions in terms of the interdisciplinary research with astrophysics, astronomy, etc.

The scope of this study is to evaluate the initial isotopic abundance of niobium-92

(^{92}Nb) and its distribution in the early solar system through combined petrology, geochemistry, stable-isotope chemistry, and the Nb-Zr isotopic analysis of a meteorite and to understand its significance in terms of the evolution of our solar system.

1. 1. Short-lived radionuclides and the solar system evolution

Short-lived radionuclides are radioactive nuclides with half-lives ($T_{1/2}$ ~ 0.1 to 100 Myr) significantly shorter than history of our solar system. Because of their short half-lives, they were present in the early solar system, but they have decayed away. Records of these now-extinct radionuclides are now preserved as excesses or deficits of their daughter nuclides in meteorites, and their initial abundances can be determined with high-precision via mass spectrometry. Their initial abundances at the time of solar system formation are of great interest in the study of our solar system evolution, because they provide (I) high-resolution chronometers for events in the early solar system (see the following section 1.1.1); and (II) the valuable information on the astrophysical setting of our solar system formation and evolution (see section 1.1.2).

1. 1. 1. Chronological aspect

Short-lived radionuclides provide high-resolution chronometers for events in the

early solar system, because the abundances of their daughter nuclides changed drastically over short time intervals. In one decay system (P: parent nuclide → D: daughter nuclide), the decay equation is written as follows (Carlson and Boyet, 2009):

$$(D / D_n)_{present} = (D / D_n)_{initial} + (P / D_n)_{initial} \times (1 - e^{-\lambda T}) \qquad \text{(i)}$$

where subscript “n" refers a non-radiogenic stable isotope, subscripts “present” and “initial” refer at the present and the time of the system closure (at T), and λ is the decay constant for the parent nuclide.

Because the age T is much larger than the half-life of short-lived parent nuclide, $(P / D_n)_{initial} \times (1 - e^{-\lambda T})$ approaches to the value of $(P / D_n)_{initial}$, and equation (i) is rewritten as follows;

$$(D / D_n)_{present} = (D / D_n)_{initial} + (P / P_n)_{initial} \times (P_n / D_n)_{present} \qquad \text{(ii)}$$

Hence, a regression line (so called isochron) on a plot of $(D / D_n)_{present}$ vs. $(P_n / D_n)_{present}$ gives a slope corresponding to $(P / P_n)_{initial}$. Furthermore, $(P / P_n)_{initial}$ can be related to the ratio at the time of solar system formation $(P / P_n)_0$:

$$(P / P_n)_{initial} = (P / P_n)_0 \times e^{-\lambda \Delta t} \qquad \text{(iii)}$$

where Δt is the time interval between the system closure and solar system formation (Δt

= 4567.3 Ma – T; Connelly et al., 2012)). This equation is rewritten as follows:

$$\Delta t = -(\ln [(P / P_n)_{initial} / (P / P_n)_0]) / \lambda \qquad \text{(iv)}$$

It is obvious from this equation that the short-lived radionuclides alone can provide only relative ages (Δt). Thus, for the application of the short-lived radionuclides as absolute chronometers, it is necessary to link relative ages derived from short-lived chronometers to the absolute timescale with a precise long-lived chronometer. In other words, the ratio of the now-extinct short-lived radionuclides to its stable partner isotope must be determined at some known ancient time while they were still alive. As a precise long-lived chronometer, the uranium-lead (U-Pb) system is particularly useful because it involves two radioactive decay chains, ^{238}U and ^{235}U decay to ^{206}Pb and ^{207}Pb at different rates, respectively, and both of the decay constants were determined with high precision (Jaffey et al., 1971; Mattinson et al., 2010). These two decay chains can be combined and the absolute age of meteorite can be determined by the ratio of radiogenic isotopes of ^{206}Pb and ^{207}Pb without using U/Pb ratios. Therefore, it is essential to establish a "*Time anchor*", i.e., a meteorite in which the initial abundances of short-lived radionuclides can be determined and to which the high precision U-Pb chronometer can be applied.

To be the "*Time anchor*", one meteorite must satisfy the following conditions (Fig. 1) (see McKeegan and Davis, 2003; Wadhwa et al., 2009; Davis and McKeegan, 2014):

(1) The U-Pb age can be obtained; (2) an (internal) isochron of the short-lived radionuclide can be obtained; (3) a cooling rate is rapid enough so as to make the difference of closure temperature between the two chronometers negligible; (4) the meteorite has not been affected by secondary alternation or exotic components that disturb the ages. Whether one meteorite satisfies all these conditions of (1)~(4) or not has to be investigated by both high-precision isotopic dating and petrological studies (cooling rate, mineral chemistry, texture etc.).

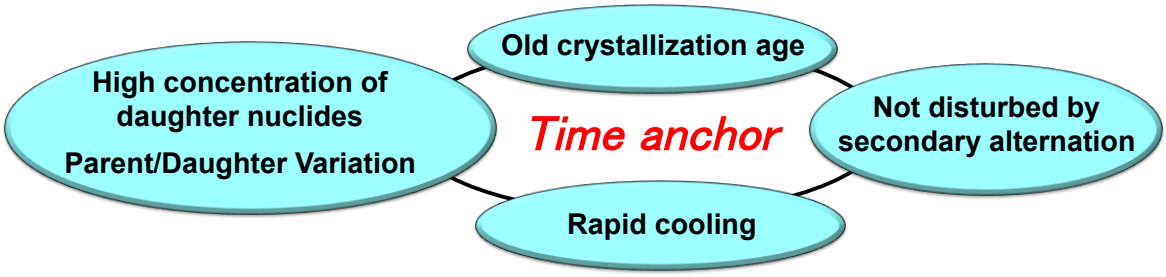

Fig. 1. The conditions needed for one meteorite to be used as a *Time anchor*.

As shown in the equation (iii), the application of the chronometer based on short-lived radionuclide further requires that the initial abundance of parent isotope $(P / P_n)_0$ must be demonstrated to be uniform among the regions where the samples originated from. Whether the short-lived isotopes were uniformly distributed in the solar system or not has been a main topic of cosmochemistry (e.g., Srinivasan et al.,

1994; Tachibana and Huss, 2003; Larsen et al., 2011; Wasserburg et al., 2012). This can be checked only by establishing multiple *Time anchors* that originated from different regions of the solar system. A good example of most widely used *Time anchor* includes a relatively small number of exceptionally old and unmetamorphosed igneous meteorites, such as the angrite D'Orbigny (4563.37 ± 0.25 Ma; Brennecka and Wadhwa, 2012), angrite NWA 2976 (4562.89 ± 0.59 Ma; Bouvier et al., 2011a,b), and CAIs from well-preserved unequilibrated chondrites Efremovka and Allende (CV3; Amelin et al., 2010; Connelly et al., 2012). Establishing a new *Time anchor* having a distinct origin allows more rigorous evaluation of the spatial distribution of short-lived radionuclides in our solar system.

With the recent improvements of precision and accuracy of isotopic measurements using multicollector inductively coupled plasma mass spectrometry (MC-ICPMS), and thermal ionization mass spectrometry (TIMS), we can now resolve small stable-isotopic heterogeneity. In particular, the recent findings of mass-independent isotopic variations of nucleosynthetic origin among different solar system reservoirs (*e.g.,* O, Ti, Cr, Sr, Mo, Zr; Clayton et al., 1973; Trinquier et al., 2009; Akram et al., 2013; Yokoyama et al., 2015; Yokoyama and Walker, 2016; Kruijer et al., 2017) provide a means to trace the genetic relationships between the planetary materials (*e.g.,* Warren, 2011, see section 2.1.). Thus, the combined analyses of short-lived isotope systems and stable isotopes, together with petrology, and geochemistry, are indispensable for establishing *Time anchors* and, in turn, evaluating the spatial distribution of short-lived radionuclides in the early solar system.

1. 1. 2. Nucleosynthetic aspect

The initial abundance and distribution of short-lived radionuclides, deduced from the study of meteorites, provide important constraints on the astrophysical context of our solar system formation. From theoretical point of view, a nucleosynthesis in nearby dying star (supernova, asymptotic giant branch star, or Wolf-Rayet star; see *e.g.,* Wasserburg et al., 2006; Huss et al., 2009; Ouellette et al., 2009; Dauphas and Chaussidon, 2011) contributed to the primary source of most short-lived radionuclides. Some of them may have been inherited from the background molecular cloud (e.g., ^{26}Al, ^{36}Cl; Young, 2014) or produced through irradiation by spallation-induced nuclear reactions between high-energy cosmic rays (proton, α-particle, heavy nucleus) and ambient gas/solid near the proto-Sun (e.g., ^{10}Be; Gounelle et al., 2006). This also applies to the abundances of stable or long-lived nuclides. The isotopic heterogeneities between bulk meteorites are interpreted to result from the mechanical incomplete mixing and/or local thermal processing of different presolar nucleosynthetic carrier phases (e.g., Qin et al., 2011; Trinquier et al., 2009; Yokoyama et al., 2015). Yet, there is no unified model for the interaction between nucleosynthetic source and the molecular cloud from which the solar system formed.

In stars born with about 1~10 $M_{\odot}$, nuclear burning processes do not typically proceed, but the production of nuclei occurs actively during the final phases of the lives of stars, namely a thermally pulsating asymptotic giant branch (AGB) phase (Lugaro et al., 2018). However, the probability of an AGB star injecting dust in a given forming

protoplanetary system is very low (Ouellette et al., 2009). When the most of the original stellar mass is lost, the core of the star is left as a white dwarf (WD). The lifetimes of such stars are typically several tens of Myr to 1000 Myr (Lugaro et al., 2018).

On the other hand, more massive stars live shorter, from a few Myr to a few tens of Myr (Lugaro et al., 2018); instead the temperature in the core increases further. These massive stars end up their lives with the final core collapse explosion (CCSN explosion), which are known as Type II supernovae (SNeII). Binary interaction can also result in nucleosynthesis, if the accretion of mass from a stellar companion brings about thermonuclear explosions of a carbon-oxygen white dwarf, which is classified as Type Ia supernovae (SNeIa; Pan et al., 2012). In these stars, a large variety of reactions including C, Ne, and O burning, and nuclear statistical equilibrium (NSE) can occur, and most intermediate to Fe-peak mass nuclei are produced.

The origin of heavy elements beyond Fe-peak is one of the main open questions in science. The slow neutron-capture process of nucleosynthesis (*s*-process; Käppler et al., 2011), occurring primarily in He and C burning in low-mass AGB or in the hydrostatic burning massive-mass AGB stars, produces about half of the heavy element abundances in the universe. The remaining requires a more violent process known as the rapid neutron-capture process of nucleosynthesis (*r*-process; Arnould et al., 2007). The *r*-process occurs in much higher neutron densities, and isotopes can rapidly capture many neutrons before those neutrons β-decay into protons. Unlike the *s*-process, there is little consensus on the astrophysical origin of the *r*-process, but SNeII, neutron star mergers, and neutron star/black hole mergers are currently being considered (e.g.,

Arnould et al. 2007; Thielemann et al. 2011; Papish et al. 2015; Liccardo et al. 2018). A few tens of nuclei located on the proton-rich side of the valley of β-stability, the so-called *p*-process nuclei cannot be produced by neutron captures, and typically one to two orders of magnitude less than the *s*- and *r*- process components in the same element. The astrophysical origin of the *p*-process is also still uncertain: there are several models (see section 4.4.2.) including photodisintegration reactions during explosive O/Ne shell burning in SNeIa (γ-process; Travaglio et al., 2014), and the α-rich freezeout (Meyer, 2003) or neutrino-induced reactions (so called *v*-process) in the core-collapse SNeII (Hayakawa et al., 2013). The *p*-process nuclides are, therefore, sensitive monitors for the distribution of supernova material, and the initial abundances of them deduced from meteorites (i.e., *Time anchors*), are expected to place constraints on the origin of nucleosynthetic isotope variations in the early solar system.

1. 2. Niobium-92

Among the short-lived radionuclides, what is of particular interest to this study is niobium-92 (^{92}Nb). ^{92}Nb is a proton-rich radionuclide that cannot be synthesized by the rapid(r) or slow(s) neutron captures unlike other majority of nuclei. Although several models (Meyer 2003; Hayakawa et al. 2013; Travaglio et al., 2014) have been proposed to account for the initial ^{92}Nb/^{93}Nb in the early solar system, the exact nucleosynthetic origin of ^{92}Nb remains unknown.

^{92}Nb decays to zirconium-92 (^{92}Zr) by electron capture with a half-life of 37 million years (My) (Holden, 1990). Both Nb and Zr are refractory (Lodders, 2003) and strongly incompatible elements. The system is sensitive to silicate partial melting and the metal-silicate separation (e.g., Tiepolo et al., 2001; Münker et al., 2017), making the Nb–Zr system to be a promising chronometer for addressing the early solar system evolution. The initial abundance of now-extinct ^{92}Nb and its distribution at the start of solar system are, therefore, required to be clearly determined through the meteoritic analyses.

Evidence for the former presence of ^{92}Nb was first identified in a well-resolved ε^{92}Zr = 8.8 ± 1.7 excess in a Nb-rich rutile grain from the Toluca IAB iron meteorite (Harper, 1996). Based on this excess, initial $(^{92}Nb/^{93}Nb)_0 = (1.6 \pm 0.3) \times 10^{-5}$ at the time of solar system formation was inferred. Three following studies using MC-ICPMS reported substantially higher initial $(^{92}Nb/^{93}Nb)_0 \sim 10^{-3}$ (Münker et al., 2000; Sanloup et al., 2000; Yin et al., 2000). This value is almost two orders of magnitude higher than that in Harper (1996), and limits the possible sites for p-process nucleosynthesis. In contrast, a combined Zr isotopic and U-Pb age study of zircon grains from the Camel Donga eucrite using LA-ICPMS indicated that the initial $(^{92}Nb/^{93}Nb)_0$ was $< 10^{-4}$ at the time of solar system formation (Hirata, 2001). The situation was broken through by Schönbachler et al. (2002), which reported the first internal ^{92}Nb-^{92}Zr isochron study. They applied the internal isochron dating to the Estacardo H6 chondrite and Vaca Muerta mesosiderite, and inferred the initial $(^{92}Nb/^{93}Nb)_0 \sim 10^{-5}$. Yin and Jacobsen (2002) then suggested that Estacado and Vaca Muerta may have been suffered from

secondary events ~ 150 ± 20 Ma after the formation of solar system, and that the lower initial ratio reported by Schönbachler et al. (2002) could be reconciled with the previously reported higher value of $(^{92}Nb/^{93}Nb)_0 \sim 10^{-3}$ (Münker et al., 2000; Sanloup et al., 2000; Yin et al., 2000). As such, the initial abundance of ^{92}Nb had been uncertain and debated topic. The situation was broken through again by the work of Iizuka et al. (2016). While Schönbachler et al. (2002) used the samples with different origins and their formation ages are uncertain, Iizuka et al. (2016) used three unbrecciated achondrites with known U-Pb absolute ages and with reasonably constrained thermal history: the NWA 4590 angrite, Agoult eucrite, and Ibitira ungrouped achondrite. All initial values of $(^{92}Nb/^{93}Nb)_0$ estimated by applying the internal ^{92}Nb-^{92}Zr isochron approach to these meteorites were consistent with each other, and Iizuka et al. (2016) concluded that the ^{92}Nb was homogeneously distributed in their source regions of the protoplanetary disk. Since Agoult and Ibitira were subjected to chemical equilibration during secondary processes (Yamaguchi et al., 2009; Iizuka et al., 2013, 2014, 2015), only NWA 4590 satisfied all the conditions (1)~(4) to be used as a "*Time anchor*" (Kuehner and Irving, 2007; Riches et al., 2012), so they concluded that NWA 4590 serves as the best estimate for the initial ^{92}Nb abundance at the time of solar system formation. This yielded an initial $(^{92}Nb/^{93}Nb)_0 = (1.7 \pm 0.6) \times 10^{-5}$, which is consistent with the value obtained for other meteorites including eucrites, ordinary chondrites, and mesosiderites (Hirata, 2001; Schönbachler et al. 2002; Iizuka et al. 2016). Therefore, to determine the initial ^{92}Nb isotopic abundance and evaluate the homogeneity in the early solar system, it is crucial to apply the internal isochron approach to meteorites that

satisfy the conditions to be used as a *Time anchor*. Recently, Haba et al. (2017) obtained a highly precise initial ^{92}Nb abundance of $(^{92}Nb/^{93}Nb)_0 = (1.6 \pm 0.1) \times 10^{-5}$ using rutiles and zircons separated from several mesosidsrites with a known absolute age. Although this is not the internal isochron from a single meteorite, the result is also consistent with the current canonical value of $(^{92}Nb/^{93}Nb)_0 = (1.7 \pm 0.6) \times 10^{-5}$. Thus, the current paradigm is that the initial ^{92}Nb abundance at the solar system formation was $(1.7 \pm 0.6) \times 10^{-5}$ (Iizuka et al. 2016) obtained from the NWA 4590 angrite (4557.93 ± 0.36 Ma; Amelin et al., 2011a), and ^{92}Nb was homogeneously distributed in the solar system (including eucrites, ordinary chondrites, and mesosiderites).

However, all of these previously studied meteorites (angrites, eucrites, ordinary chondrites, and mesosiderites) are depleted in volatile elements relative to CI chondrites and are thought to have originated from < ~5 astronomical units (AU) (Warren, 2011), and so should provide field records only from the inner solar system. This means that we still cannot achieve the evaluation of the initial abundance and distribution of ^{92}Nb in the accretion region of carbonaceous chondrites (i.e., the outer solar system). Therefore, a new *Time anchor* from the outer solar system is essential to evaluate the distribution of the now-extinct ^{92}Nb in the wide regions of our solar system.

1. 3. Composition of this thesis

The purpose of this study is to evaluate the initial abundance and distribution of ^{92}Nb in the early solar system, on the largest scale to date. To achieve this purpose, a recently found ungrouped primitive achondrite NWA 6704 has been investigated. Developing NWA 6704 as the first "*Time anchor*" from the outer solar system, and applying the Nb-Zr internal isochron approach to NWA 6704, we could determine the initial abundance of ^{92}Nb in the outer solar system. This allowed us to evaluate the distribution of ^{92}Nb between the inner and outer solar system, and to provide new constraints on the early solar system chronology and on the astrophysical context of early solar system processes related to ^{92}Nb.

This thesis is organized as follows. In Chapter 2, before getting down to the analysis of NWA 6704, we developed a new method for combined Cr–Ti isotope analysis applicable to various planetary materials. This chapter is modified from Hibiya et al. (2019a) published in *Geostandards and Geoanalytical Research*. In Chapter 3, the new method developed in Chapter 2 was applied to NWA 6704, and the origin of this meteorite was investigated in terms of the petrology, geochemistry and ^{187}Re–^{187}Os and O–Cr–Ti isotope systematics. On the basis of our results, we discussed the crystallization process of NWA 6704, the nature and provenance of its parent body, and its potential utility as a *Time anchor*. This chapter is modified mainly from Hibiya et al. (2019a) that has been published in *Geochimica Cosmochimica Acta*. In Chapter 4, the Nb–Zr dating of NWA 6704 was conducted and the initial ^{92}Nb abundance (^{92}Nb/^{93}Nb)$_0$

at the start of our solar system was determined for evaluating the distribution of ^{92}Nb in the early solar system. This chapter is under preparation for submission, and is not published yet. Finally, we conclude the whole study with discussions about the significance of this thesis and future works.

Northwest Africa (NWA) 6704 is an ungrouped achondrite found in Algeria in 2010, with a total known weight of 8.387 kg (Le Corre et al., 2014). NWA 6704 has rounded shiny surfaces with one small patch of remnant black fusion crust (Fig. 2). Its interior exhibits an igneous texture with no diagnostic shock deformation effects (Irving et al., 2011). The degree of weathering is restricted to minor coatings of orange dust on broken surfaces (Le Corre et al., 2014). The texture is composed of low-Ca pyroxene, less abundant Ni-rich olivine, plagioclase, chromite, Ni-Fe-metal (awaruite), sulfides (heazlewoodite and pentlandite) and merrillite (Irving et al., 2011; Le Corre et al., 2014). Initial studies indicated that its bulk major element composition is nearly chondritic (Fernandes et al., 2013). U–Pb dating for acid-washed pyroxene of NWA 6704 has yielded 4562.76 ± 0.30 Ma with a measured ^{238}U/^{235}U ratio of 137.7784 ± 0.0097 (Amelin et al., 2019). The pristine chondrite-like characteristics of NWA 6704, coupled with its ancient crystallization age, and its igneous texture different from any known achondrite make it ideal for exploring whether it is the first "*Time anchor* from the outer solar system".

Fig. 2. An image of the reassembled mass of NWA 6704 (courtesy of Greg Hupe). The scale cube is 1 cm^3.

2. Development of new isotope analytical method

2. 1. Background

Planetary materials show variable Cr and Ti isotope compositions that do not follow mass-dependent fractionation. For instance, meteorites formed during the first 10 Myrs of solar system history exhibit variations in $^{53}Cr/^{52}Cr$ (Lugmair and Shukolyukov 1998, Trinquier et al. 2008a) generated by the decay of the short-lived radionuclide ^{53}Mn (half-life: 3.7 ± 0.4 Ma; Honda and Imamura 1971). Thus, the ^{53}Mn–^{53}Cr system has been used widely for dating early solar system processes associated with Mn/Cr fractionation. Furthermore, carbonaceous chondrites have excesses in both ^{54}Cr and ^{50}Ti (i.e., neutron-rich isotopes) compared with Earth, ordinary and enstatite chondrites and most achondrites (e.g., Shukolyukov and Lugmair 2006a, Trinquier et al. 2007, 2009, Leya et al. 2008, Qin et al. 2010, Zhang et al. 2012, Burkhardt et al. 2017, Gerber et al. 2017). In recent years, Warren (2011) summarized the striking bimodality of planetary materials on the $\varepsilon^{50}Ti$ vs. $\varepsilon^{54}Cr$ and $\Delta^{17}O$ vs. $\varepsilon^{54}Cr$ diagrams (Fig. 3a and b). Warren (2011) speculated that the bimodality correspond to a division between materials that originally accreted in the inner solar system (noncarbonaceous chondrites and achondrites including ureilites at neutron-poor end) and materials that originally accreted in the outer solar system (carbonaceous chondrites at neutron-rich end). The striking isotope dichotomy in planetary materials indicates division of an isotopically heterogeneous protoplanetary disk into a neutron-rich outer region, where carbonaceous

planetesimals accreted, and a neutron-poor inner region, where non-carbonaceous planetesimals accreted. These isotope heterogeneities are interpreted to reflect spatially and/or temporally uneven distributions of phases that preserve presolar nucleosynthetic anomalies. Accordingly, ^{54}Cr and ^{50}Ti anomalies can be used both to trace meteorite source regions and to investigate genetic relationships among planetary materials (*e.g.* Warren 2011).

There is considerable debate, however, as to when and how such presolar phases might have been brought into the protoplanetary disk. Basically, two models have been proposed to explain the observed heterogeneous distributions of ^{54}Cr and ^{50}Ti at the planetary scale. One model is that extremely neutron-rich nano-phases produced in a supernova were injected into the solar nebula at a large heliocentric distance (e.g., Leya et al., 2009; Yamakawa et al, 2010; Sugiura et al., 2014). Step-wise acid dissolution experiments have revealed the neutron-rich carrier and the opposite extreme carrier phases (e.g., Rotaru et al., 1992; Podosek et al., 1997; Trinquier et al., 2007). The former is soluble in relatively weak acid and the latter (refractory phases) more acid-resistant. In addition, large positive ^{54}Cr anomalies up to +1500 ‰ were found in the nm-size Cr-bearing presolar spinel in the Orgueil (CI) carbonaceous chondrite (Qin et al., 2011). The other model is that the local thermal processing of molecular cloud materials resulted in the preferential loss of the thermally unstable presolar silicates (e.g., Trinquier et al., 2009; Yokoyama et al., 2015). Trinquier et al. (2009) identified the linear correlation in a $\varepsilon(^{50}\mathrm{Ti}/^{47}\mathrm{Ti})$-$\varepsilon(^{46}\mathrm{Ti}/^{47}\mathrm{Ti})$ variation diagram. Considering that ^{46}Ti and ^{50}Ti have different nucleosynthetic origins, this correlation suggests that the

proto-solar molecular cloud was initially well mixed, and further requires a subsequent process causing isotopic variations at the planetary scale.

Combined analysis of Cr and Ti isotope data for planetary materials can provide important clues regarding meteorite provenance and the origin of isotope heterogeneities in the protoplanetary disk (*e.g.* Warren 2011, Trinquier et al. 2009). Previously reported data for non-carbonaceous meteorites show positive correlation between $^{54}Cr/^{52}Cr$ and $^{50}Ti/^{47}Ti$, whereas those for carbonaceous chondrites exhibit weak negative correlation between the isotope ratios, implying that different mechanisms produced the Cr and Ti isotope variations within the inner and outer disks. Note, however, that almost all reported Cr–Ti isotope data have been obtained from different fragments of single meteorites or meteorite groups. This becomes a serious problem when interpreting data obtained from isotopically heterogeneous samples. Indeed, internal Cr and/or Ti isotope variations have been found in some meteorite groups, *e.g.*, ureilites (*e.g.* Leya et al. 2008, Yamakawa et al. 2010, Larsen et al. 2011, Jenniskens et al. 2012), CV chondrites (*e.g.* Qin et al. 2010, Schoenberg et al. 2016), and CB chondrites (Yamashita et al. 2010, Van Kooten et al. 2016). Hence, combined isotope measurements of Cr and Ti in single fractions of planetary materials are indispensable for identifying the phases that contribute to these isotope anomalies and, in turn, for understanding the evolution of the protoplanetary disk.

In this study, we developed the new sequential chemical separation procedure for combined high-precision Cr and Ti isotope ratio measurements of planetary materials. By applying the procedure to samples having various compositions ranging from

basaltic to peridotitic, we evaluated its utility and versatility. Furthermore, we measured the Cr and Ti isotope compositions of the separated samples using thermal ionization mass spectrometry (TIMS) and multiple collector–inductively coupled plasma mass spectrometry (MC–ICPMS), respectively.

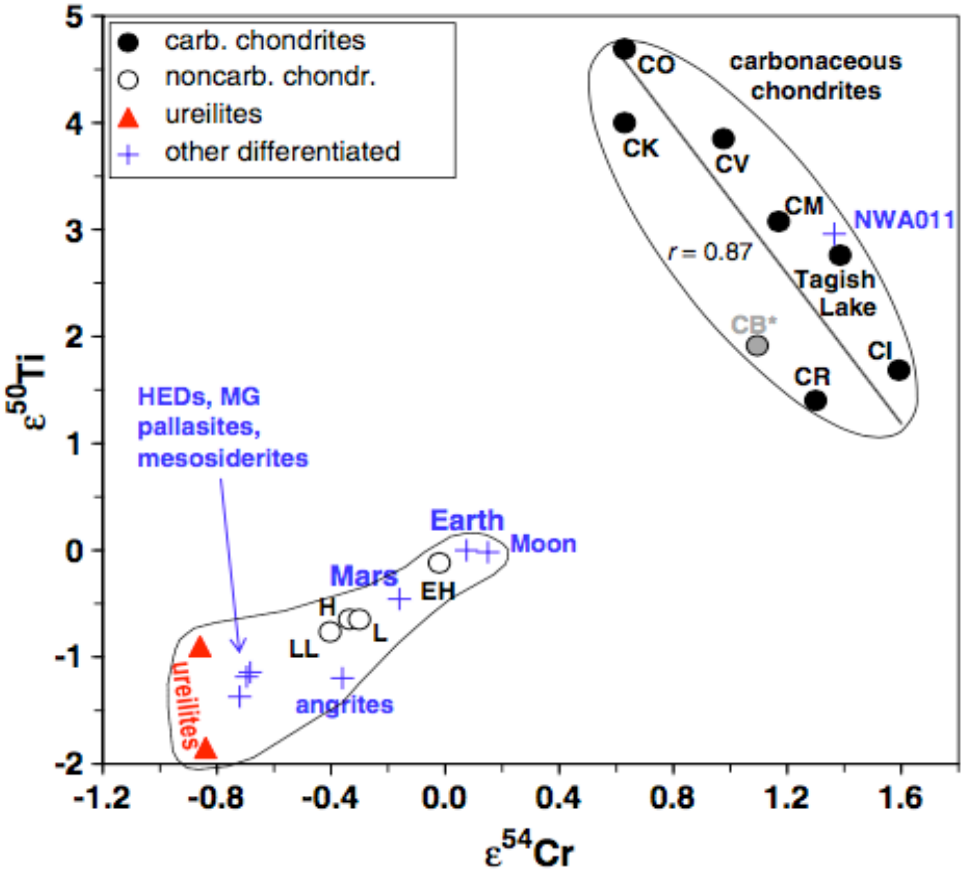

Fig. 3a. Stable isotopes ε^{50}Ti vs. ε^{54}Cr in planetary materials. Data sources for ε^{54}Cr: Bogdanovski and Lugmair (2004), Yamashita et al. (2005), Shukolyukov and Lugmair (2006a,b), Ueda et al. (2006), Trinquier et al. (2007, 2008), Yin et al. (2009), de Leuw et al. (2010), Qin et al. (2010a,b), Shukolyukov et al. (2011); for ε^{50}Ti: Leya et al. (2008) and Trinquier et al. (2009). The two ureilites that have been analyzed for both ε^{50}Ti and ε^{54}Cr are ALH 77257 and NWA 2376 (Leya et al., 2008; Ueda et al., 2006; Yamakawa et al., 2010). The plotted CB point is the average of different CB (Shukolyukov and Lugmair, 2006a).

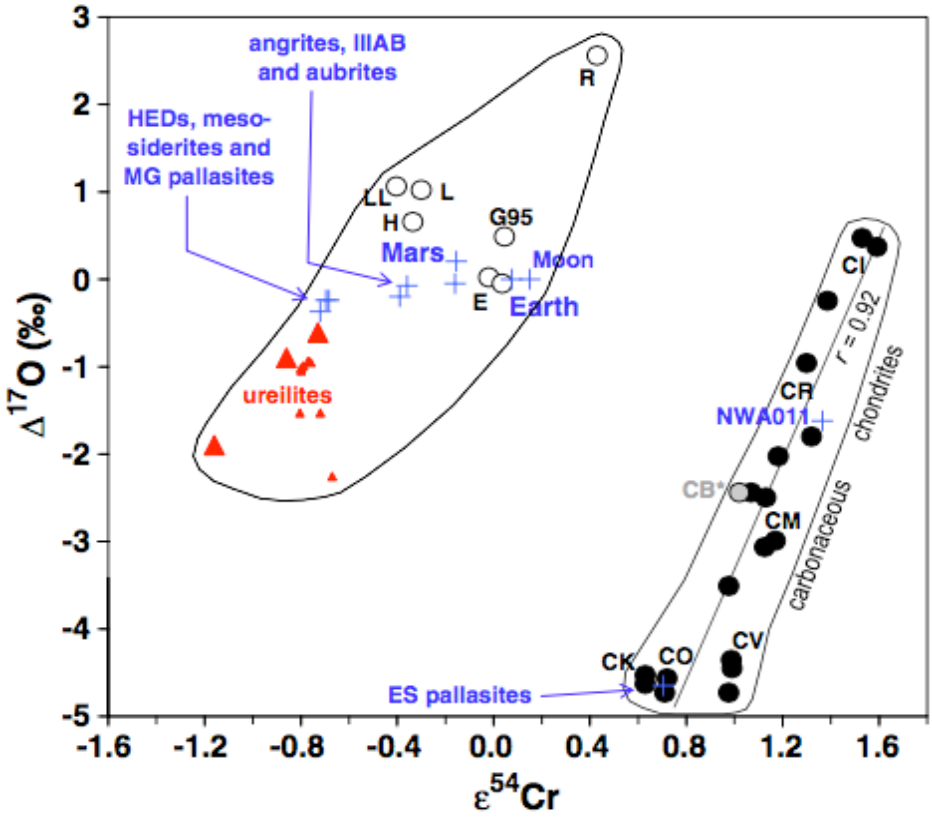

Fig. 3b. Stable isotopes $\Delta^{17}O$ vs. $\varepsilon^{54}Cr$ in planetary materials. Data sources for $\varepsilon^{54}Cr$: Bogdanovski and Lugmair (2004), Yamashita et al. (2005), Shukolyukov and Lugmair (2006a,b), Ueda et al. (2006), Trinquier et al. (2007, 2008), Yin et al. (2009), de Leuw et al. (2010), Qin et al. (2010a,b), Shukolyukov et al. (2011); for $\Delta^{17}O$: Clayton and Mayeda (1988, 1996), Clayton et al. (1976, 1991). The only three ureilites that have been analyzed for both $\Delta^{17}O$ and $\varepsilon^{54}Cr$ are ALH 77257, MET 78008, and Y-791538 (Leya et al., 2008; Ueda et al., 2006; Yamakawa et al., 2010). The plotted CB point is the average of different CB (Shukolyukov and Lugmair, 2006a).

2. 2. Methods

2. 2. 1. Samples for Cr and Ti isotope analysis

We analyzed four terrestrial and meteorite samples of various compositions for Cr and Ti isotopes (Table 1). The terrestrial samples were composed of well-characterized standard rock powders of basalt JB-1b and peridotite JP-1, distributed by the Geological Survey of Japan. The meteorite samples consisted of a reference powder of the carbonaceous chondrite Allende from the Smithsonian Institution, and the basaltic eucrite Juvinas. For the Juvinas specimen, piece of bulk sample was disaggregated in an agate mortar. The disaggregated meteorite sample was washed in a distilled acetone ultrasonic bath for about 10 minutes, and then heated on a hotplate and evaporated to dryness. Multiple fractions of Juvinas (five fractions) as well as Allende (two fractions) were analyzed to evaluate the external reproducibility of the entire technique, including sample digestion, column chromatography, and isotope analysis. High-purity Cr from Nilaco Corp. (Yamakawa et al. 2009) and NIST 3162a Ti standard solutions were used as standards for Cr and Ti isotopic analyses, respectively. To ensure that application of the chemical procedure did not induce any mass-independent fractionation, we also analyzed the standards processed by the column chromatography.

Table 1. Samples used in this study and their Cr and Ti concentrations.

Sample name	used sample size (mg)	Cr (ppm)*	Ti (ppm)*
JB-1b (terrestrial basalt)	50 mg (25 mg ×2)	439	7552
JP-1 (terrestrial peridotite)	45 mg (15 mg ×3)	2807	36
Allende (carbonaceous chondrite)	5 mg	3600	1500
Juvinas (non-cumulate eucrite)	10 mg	2330	3820
High purity Cr-standard	Cr: 20 μg	–	–
NIST 3162a Ti-standard	Ti: 20 μg	–	–

* Data of Cr and Ti concentrations are from Terashima *et al.* (1998) for JB-1b, Imai *et al.* (1995) for JP-1, Jarosewich *et al.* (1987) for Allende, Morgan *et al.* (1978) for Juvinas.

2. 2. 2. Sample digestion

Approximately 10–50 mg of terrestrial rock and meteorite powders were weighed into clean 3 ml Teflon® vials. Subsequently, about 1.2 ml of concentrated HF and 0.9 ml of concentrated HNO_3 were added, and the vials were heated inside a Teflon® capsule sealed in a Parr® bomb at 190 °C for >65 hours. All acids used in this study are ultrapure grade reagents from Kanto Chemical Co. Inc., Japan. Once digested, the HF–HNO_3 mixtures were evaporated to dryness, followed by repeated evaporation with 0.6 ml of concentrated HNO_3 for conversion from insoluble fluorides to soluble compounds. Finally, the sample was re-dissolved in ~2 ml of 6 mol l^{-1} HCl heated on a hotplate at 140 °C for 1 day. These procedures ensured complete digestion of all meteorite and terrestrial samples, and no residues were recognizable in the vials.

2. 2. 3. Chemical separation

For high-precision determination of Cr and Ti isotope compositions using TIMS and MC–ICPMS, the chemical separation and purification of Cr and Ti from the samples are required to avoid matrix effects and spectral interferences. Table 2 summarizes potential interferences in Cr and Ti isotope analyses. The most problematic interferences arise from isobaric ions of Ti, V, and Fe on ^{50}Cr and ^{54}Cr and of Ca, V, and Cr on ^{46}Ti, ^{48}Ti, and ^{50}Ti, respectively. Hence, the isobaric elements must be separated efficiently by chemical separation. In addition, elements causing doubly charged ion interferences must be reduced sufficiently. It should be noted that ion signals of argides as well as chlorides can also interfere with Ti ion signals during MC–ICPMS analysis; however, these signals can be separated utilizing a high mass resolution mode.

The chemical separation procedure proposed in this study comprised three steps (Table 3): (i) Fe removal using AG1-X8 anion exchange resin, (ii) Ti separation using AG50W-X8 cation exchange resin, and (iii) Cr separation using AG50W-X8 cation exchange resin. The digested sample aliquots of JB-1b and JP-1 were divided into two or three fractions and individually processed for the column chromatography. This is because chemical yields of the second and third steps were substantially lowered when large amounts of rock samples (>30 mg) were introduced. In addition to the three steps, a Ti purification step was performed on samples having high Cr/Ti (~3: *e.g.,* periodite)

and Ca/Ti (~100: *e.g.,* CAIs: calcium-aluminum-rich inclusions) ratios (Table 1).

Column 1

In the first step, Fe was separated from most elements including Cr and Ti using anion exchange chromatography. One ml of Bio-Rad AG1-X8 resin (200–400 mesh) was packed in a small-sized polypropylene column purchased from Muromachi Chemical Inc., Japan (d = ~5.0 mm, h = 42 mm). The resin was washed by passing 3 mol l^{-1} HNO_3, H_2O, and 6 mol l^{-1} HCl. After conditioning the resin using 5 ml of 6 mol l^{-1} HCl, samples dissolved in 1 ml of 6 mol l^{-1} HCl were loaded onto the column. Before loading, sample solutions were heated on a hotplate at 140 °C for 1 day to ensure that Cr existed as a trivalent state. The fraction containing Cr and Ti, which began to be eluted immediately, was collected by passing an additional 4 ml of 6 mol l^{-1} HCl.

Column 2

In the second step, Ti was separated from the Cr-fraction based on the procedure described by Zhang *et al.* (2011). Eichrom pre-packed 2 ml cartridges containing TODGA resin (200–400 mesh) associated with the cartridge reservoirs (15 ml, d = ~10 mm, h = 25 mm) were used. First, the resin was washed by passing 12 mol l^{-1} HNO_3 and 12 mol l^{-1} HNO_3 + 1wt% H_2O_2 and H_2O. After conditioning the resin using 5 ml of 12 mol l^{-1} HNO_3, samples dissolved in 3 ml of 12 mol l^{-1} HNO_3 were loaded onto the column. Chromium, together with matrix elements such as Ca, was collected with the

initial load and an additional 12 ml of 12 mol l^{-1} HNO_3. Then, Ti was collected as an orange-red Ti $(H_2O_2)_x$ complex with 10 ml of 12 mol l^{-1} HNO_3 + 1 wt% H_2O_2. For this step, H_2O_2 was mixed with HNO_3 1 hour before the load. This was done because H_2O_2 dissociates into H_2O and O_2 with time, whereas the addition of H_2O_2 to 12 mol l^{-1} HNO_3 immediately before the loading can lower the recovery rate of Ti, likely because of insufficient reaction between H_2O_2 and HNO_3 (Yang et al. 2015).

Column 3

In the third step, Cr was purified from the matrix elements. Prior to the third step, we controlled the temperature and acid concentration of the sample fractions recovered from the second step such that the Cr(III) remained the dominant species in the acid. This method is based on the equilibrium Cr speciation model described in (Larsen et al. 2016). After Ti separation, the Cr fraction in 12 mol l^{-1} HNO_3 was evaporated slowly to dryness on a hotplate at 100 °C, because Cr will be fully reduced to Cr(III) in >8 mol l^{-1} HNO_3 at <120 ˚C (Larsen et al. 2016). The dried Cr fraction was then dissolved in 0.5 ml of 4 mol l^{-1} HNO_3, washed in an ultrasonic bath for about 5 minutes, and then heated on a hotplate for more than 3 hours at 70 °C. Subsequently, the sample aliquots were converted to a total volume of 2 ml of 1 mol l^{-1} HNO_3 + 1 wt% H_2O_2 solution by dilution with H_2O, followed by the addition of H_2O_2 (60 μL). The addition of H_2O_2, which acts as a reducing agent at low pH, effectively aids the formation of the Cr(III) species. The formation of the trivalent Cr species was promoted further by the 4-day-storage at room temperature before column loading (Larsen et al. 2016).

The third step column chemistry was modified from the procedure described by (Yamakawa et al. 2009). One ml of Bio-Rad AG50W-X8 cation exchange resin (200–400 mesh) was packed in the small-sized polypropylene column from Muromachi Chemical Inc. (d = ~5.0 mm, h = 42 mm). First, the resin was washed by passing 6 mol l^{-1} HCl, 1 mol l^{-1} HF, and H_2O. After conditioning the resin using 3 ml of 0.5 mol l^{-1} HNO_3, samples dissolved in ~2 ml of 1 mol l^{-1} HNO_3 + 1 wt% H_2O_2 solution were loaded onto the column. Then, matrix elements including V and the remaining Ti and Fe were eluted in 0.7 mol l^{-1} HNO_3, followed by elution of Al in 0.5 mol l^{-1} HF. Finally, Cr was collected with 4 ml of 6 mol l^{-1} HCl.

Additional Column

For samples having high Cr/Ti (*e.g.,* peridotite) and/or Ca/Ti ratios (*e.g.,* CAIs), an additional separation step for Ti purification is desirable. This step removes trace amounts of Ca and Cr from the sample, based on the Ti purification procedure described by (Zhang et al. 2011) and the W separation procedure described by (Breton and Quitté 2014). The AG1-X8 anion exchange resin, packed in the small-sized polypropylene column, was washed by passing 9 ml of 3 mol l^{-1} HNO_3, 3 ml of H_2O, 5 ml of 0.4 mol l^{-1} HCl + 1 mol l^{-1} HF, 5 ml of concentrated 9 mol l^{-1} HCl + 0.01 mol l^{-1} HF, and 9 ml of H_2O. After conditioning the resin using 5 ml of 4 mol l^{-1} HF, samples dissolved in 2 ml of 4 mol l^{-1} HF were loaded onto the column. Then, matrix elements including the remaining Ca were eluted in 4 mol l^{-1} HF, followed by elution of the remaining V in 0.4

mol l^{-1} HCl + 1 mol l^{-1} HF. Finally, the Ti was collected with 10 ml of 1 mol l^{-1} HCl + 2 wt% H_2O_2.

Table 2.
Possible interferences in Cr and Ti isotope measurements

Mass	**46**	**47**	**48**	**49**	**50**	**51**	**52**	**53**	**54**
Single charged ion	$^{46}Ca^+$		$^{48}Ca^+$						
	$^{46}Ti^+$	$^{47}Ti^+$	$^{48}Ti^+$	$^{49}Ti^+$	$^{50}Ti^+$				
					$^{50}V^+$	$^{51}V^+$			
					$^{50}Cr^+$		$^{52}Cr^+$	$^{53}Cr^+$	$^{54}Cr^+$
									$^{54}Fe^+$
Doubly-charged ion	$^{92}Zr^{++}$	$^{94}Zr^{++}$	$^{96}Zr^{++}$						
	$^{92}Mo^{++}$	$^{94}Mo^{++}$	$^{96}Mo^{++}$	$^{98}Mo^{++}$	$^{100}Mo^{++}$				
			$^{96}Ru^{++}$	$^{98}Ru^{++}$	$^{100}Ru^{++}$	$^{102}Ru^{++}$	$^{104}Ru^{++}$		
						$^{102}Pd^{++}$	$^{104}Pd^{++}$	$^{106}Pd^{++}$	$^{108}Pd^{++}$
Polyatomic ion	$^{28}Si^{19}F^+$	$^{36}Ar^{12}C^+$	$^{36}Ar^{13}C^+$	$^{36}Ar^{14}N^+$	$^{38}Ar^{13}C^+$	$^{40}Ar^{12}C^+$	$^{40}Ar^{13}C^+$	$^{40}Ar^{14}N^+$	
(Argides, Flourides, Carbides, Chlorides)						$^{36}Ar^{15}N^+$	$^{38}Ar^{14}N^+$	$^{38}Ar^{15}N^{+,}$	$^{36}Ar^{18}O^+$
							$^{36}Ar^{16}O^+$	$^{36}Ar^{17}O^+$	
	$^{35}Cl^{12}C^+$	$^{35}Cl^{13}C^+$	$^{35}Cl^{14}N^+$	$^{35}Cl^{15}N^+$	$^{37}Cl^{14}N^+$	$^{37}Cl^{15}N^+$	$^{35}Cl^{18}O^+$	$^{37}Cl^{17}O^+$	
			$^{37}Cl^{12}C^+$	$^{37}Cl^{13}C^+$	$^{35}Cl^{16}O^+$	$^{35}Cl^{17}O^+$	$^{37}Cl^{16}O^+$		

Table 3.
Chromium–Titanium column chromatography

Step	Volume (mL)	Acid
Column 1 (1mL AG1-X8 anion resin 200-400 mesh d=~5.0 mm, h=42 mm)		
Wash	8	3 $molL^{-1}$ HNO_3
	16	H_2O
	8	6 $molL^{-1}$ HCl
Precondition	5	6 $molL^{-1}$ HCl
Load	1	6 $molL^{-1}$ HCl
Elute Cr and Ti	4	6 $molL^{-1}$ HCl
Column 2 (2mL pre-packed TODGA resin 50-100 micron d=~10 mm, h=25 mm)		
Wash	10	12 $molL^{-1}$ HNO_3
	10	12 $molL^{-1}$ HNO_3 - 1wt % H_2O_2
	4	H_2O
Precondition	5	12 $molL^{-1}$ HNO_3
Load	3	12 $molL^{-1}$ HNO_3
Elute Cr	12	12 $molL^{-1}$ HNO_3
Elute Ti	10	12 $molL^{-1}$ HNO_3 - 1wt % H_2O_2
Column 3 (1mL AG50W-X8 cation resin 200-400 mesh d=~5.0 mm, h=42 mm)		
Wash	16	6 $molL^{-1}$ HCl
	8	1 $molL^{-1}$ HF
	32	H_2O
Precondition	3	0.5 $molL^{-1}$ HNO_3
Load	2	1 $molL^{-1}$ HNO_3 - 1wt % H_2O_2
Elute Matrix	130	0.7 $molL^{-1}$ HNO_3
Elute Al	6	0.5 $molL^{-1}$ HF
Elute Cr	4	6 $molL^{-1}$ HCl
Additional Column (1mL AG1-X8 anion resin 200-400 mesh d=~5.0 mm, h=42 mm)		
Wash	9	3 $molL^{-1}$ HNO_3
	3	H_2O
	9	0.4 $molL^{-1}$ HCl - 1 $molL^{-1}$ HF
	9	9 $molL^{-1}$ HCl - 0.01 $molL^{-1}$ HF
	9	H_2O
Precondition	5	4 $molL^{-1}$ HF
Load	2	4 $molL^{-1}$ HF
Elute Matrix	10	4 $molL^{-1}$ HF
Elute V	12	0.4 $molL^{-1}$ HCl - 1 $molL^{-1}$ HF
Elute Ti	10	1 $molL^{-1}$ HCl - 2 wt % H_2O_2

2. 2. 4. Mass Spectrometry

To obtain elution curves, chemical yields and blanks of the column chromatography, elemental abundances in the loaded samples and elution fractions were determined using a Thermo Fisher Scientific™ iCAP Q™ ICP–MS at the University of Tokyo. The instrument was operated with kinetic energy discrimination (KED) mode, using Ar as the sample gas with He as the collision gas. All sample and standard (SPEX multi-element solution XSTC-622) solutions were diluted in 0.5 mol l^{-1} HNO_3 with an In-Bi internal standard mixture and introduced with a CETAC ASX–520 auto-sampler.

All Cr isotope compositions of the separated samples were measured using a Thermo Fisher Scientific™ TRITON Plus™ TIMS at the National Museum of Nature and Science, Japan following the method described in (Yamakawa et al. 2009). Approximately 3 μg of Cr dissolved in 6 mol l^{-1} HCl were loaded onto the prebaked W filaments along with silica gel–boric acid–Al activator (Yamakawa et al. 2009). Each sample was divided and loaded onto four filaments, thereby consuming ~12 μg of Cr in total. The analyses were performed in static mode using six Faraday cups to monitor $^{50}Cr^{+}$, $^{51}V^{+}$, $^{52}Cr^{+}$, $^{53}Cr^{+}$, $^{54}Cr^{+}$, and $^{56}Fe^{+}$. These faraday cups were connected to 10^{11} Ω amplifiers, which were rotated after each block measurement (25 cycles per block). The gain calibration was performed at the beginning of each sample analysis. The baseline measurements were performed every 6 blocks for 360 seconds with a pre-baseline wait time of 60 seconds. The beam intensity for ^{52}Cr was set at 1×10^{-10} A. Each filament analysis included 300 scans with an integration time of 8.4 seconds in each scan (12

blocks with each block consisting of 25 scans). In addition, $^{48}Ti/^{52}Cr$ and $^{49}Ti/^{52}Cr$ ratios were measured for each filament using peak jumping mode to evaluate possible interferences of ^{50}Ti on ^{50}Cr. Yet, no significant level of interferences of ^{50}Ti and ^{50}V were found for all the separated samples and, therefore, no isobaric corrections on ^{50}Cr were undertaken. For the correction of ^{54}Fe interference, the literature $^{54}Fe/^{56}Fe$ value of 0.0637 was employed (Rosman and Taylor 1998). All sample analysis was bracketed by analyses of an in-house high-purity Cr standard purchased from Nilaco Corp., Japan (two filament loads before and after the sample). The instrumental mass fractionation effect was corrected according to an exponential law by normalizing the measured $^{50}Cr/^{52}Cr$ ratio to 0.051859 (Shields et al. 1966). The Cr isotope ratios of the samples were expressed as the relative deviation from the high-purity Cr standard in parts per 10^4:

$$\varepsilon^{n}Cr = 10^4 \times \{(^{n}Cr/^{52}Cr)_{sample}/(^{n}Cr/^{52}Cr)_{standard} - 1\} \qquad (v)$$

All Ti isotope analyses of the samples were performed on a Thermo Fisher Scientific™ Neptune Plus™ MC–ICPMS at the University of Tokyo. Diluted samples, with the typical Ti concentration of ~300 ppb, were introduced into the mass spectrometer via a CETAC Aridus-II™ desolvating nebulizer with a sample uptake rate of ~100 μl min^{-1} using Ar as the sweep gas with N_2 addition to the sample gas. Measurements were conducted using a Jet sample cone and a skimmer H-cone with high mass resolution ($M/\Delta M > 9000$), which typically yielded a total Ti beam of 2–3 ×

10^{-10} A. Data were acquired in dynamic mode using Faraday cups connected to 10^{11} Ω amplifiers to monitor $^{44}Ca^{+}$, $^{46}Ti^{+}$, $^{47}Ti^{+}$ (axial), $^{48}Ti^{+}$, $^{49}Ti^{+}$, and $^{50}Ti^{+}$ (line 1) and $^{46}Ti^{+}$, $^{47}Ti^{+}$, $^{51}V^{+}$, and $^{52}Cr^{+}$ (line 2). The integration times of 8.4 and 4.2 seconds were used for lines 1 and 2, respectively. The cup positions were adjusted carefully to measure the signals at the middle of the interference-free plateau for ^{44}Ca, ^{50}Ti, and ^{52}Cr (Table 2). A $^{91}Zr^{++}$ beam was monitored before each sample measurement because doubly charged Zr ions can interfere with Ti isotopes (Table 2). No significant $^{91}Zr^{++}$ beam was observed for any of the samples examined in this study. Each sample measurement comprised 1 to 3 blocks with each block consisting of 40 cycles, consuming ~1.5 to 4.5 μg of Ti. All sample analysis was bracketed by analyses of the NIST-3162a standard (two analyses before and after the sample analysis). The instrumental mass bias was corrected relative to $^{49}Ti/^{47}Ti = 0.749766$ (Leya et al. 2007) following the exponential law. For the correction of isobaric interferences, the literature values for $^{46}Ca/^{44}Ca$ of 0.0019175, $^{48}Ca/^{44}Ca$ of 0.089645, $^{50}Cr/^{52}Cr$ of 0.45732, and $^{50}V/^{51}V$ of 0.002506 were employed (Rosman and Taylor 1998). Furthermore, the mass bias factors of Ca, Cr, and V were assumed identical to that of Ti. The interference correction yielded accurate results for Ca-, Cr-, and V-doped synthetic 300 ppb Ti standard solutions with ratios of Ca/Ti of up to 30, Cr/Ti of up to 0.6, and V/Ti of up to 1 (Fig. 4). All Ti isotope ratios of the samples, corrected for isobaric interferences and mass bias, were expressed as relative deviations from the NIST-3162a standard in parts per 10^4:

$$\varepsilon^{n}Ti = \{(^{n}Ti/^{47}Ti)_{sample}/(^{n}Ti/^{47}Ti)_{standard} - 1\} \times 10^{4} \qquad \text{(vi)}$$

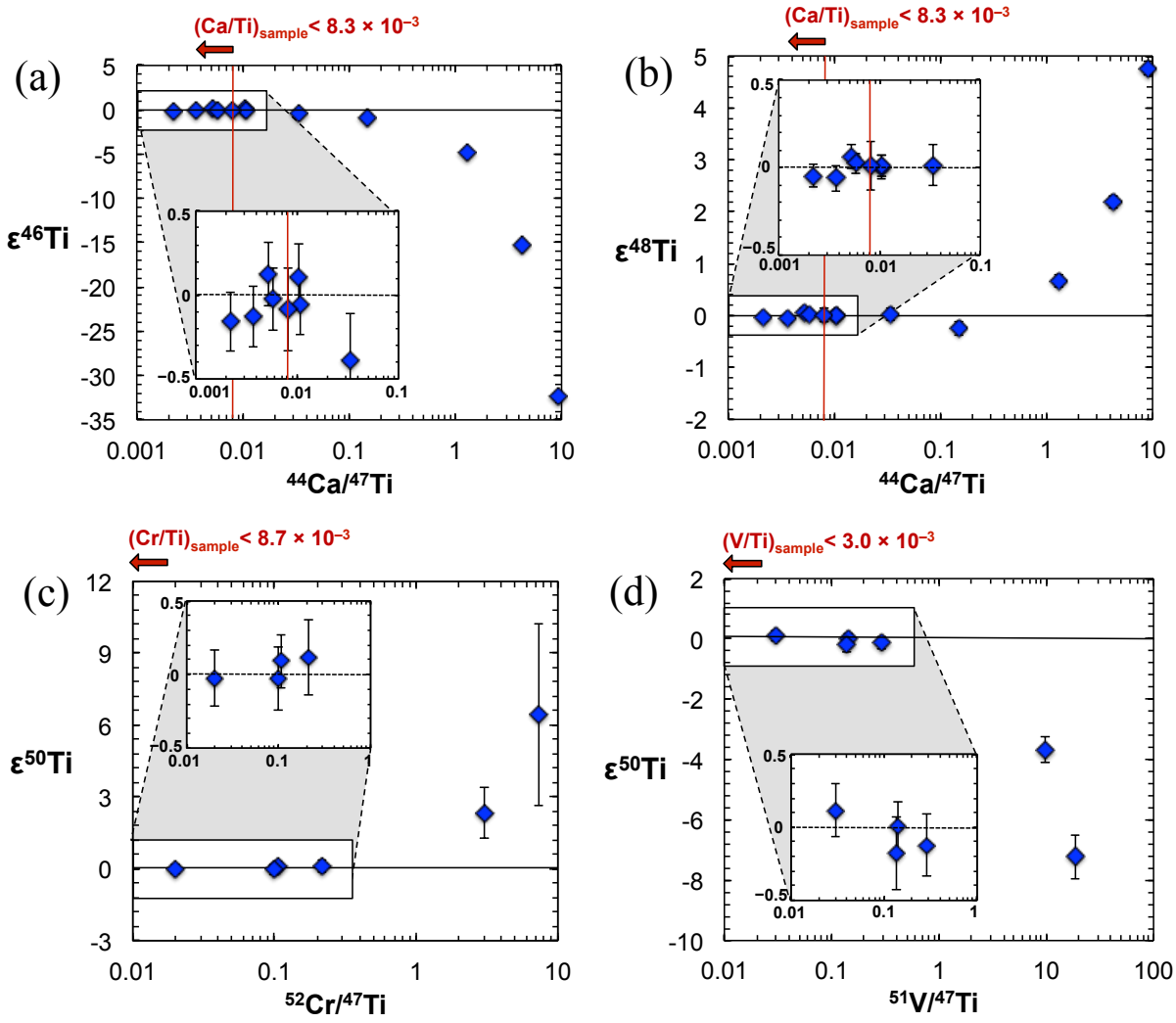

Fig. 4. Obtained ε^{46}Ti and ε^{50}Ti values after interference corrections for (a, b) Ca-, (c) Cr-, and (d) V-doped synthetic Ti standard (300 ppb) solutions. The Ca/Ti, Cr/Ti, and V/Ti ratios of our sample solutions after purification were much smaller than the accurate correction limits.

2. 3. Results and Discussion

2. 3. 1. Chemical yields and blanks

Elution curves of the major and trace elements were obtained for each separation step using 25 mg of JB-1b (terrestrial basalt) (Fig. 5). Chemical yields were determined also for JP-1, Allende, and Juvinas. In addition, a blank test was conducted for each separation step.

Column 1

In column 1, Cr and Ti were eluted with most elements including Na, Al, V, Mg, Ca, and Mn in the loading and an additional 4 ml of 6 mol l^{-1} HCl (Fig. 5a), whereas Fe was retained on the resin. The recovery rates for Cr and Ti were 96%–100% for all the studied samples. The column step reduces the Fe/Ti and Fe/Cr ratios by $>10^3$. Blank amounts were 250 pg for Cr and <200 pg for Ti.

Column 2

In column 2, Cr was eluted with Ca, Fe, Ni, V, Mn, and Al in the initial loading and an additional 12 ml of 12 mol l^{-1} HNO_3 (Fig. 5b). Subsequently, Ti was eluted with 10 ml of 12 mol l^{-1} HNO_3 + 1 wt% H_2O_2. The recovery rates for Cr and Ti were 95%–100% for JB-1b, JP-1, and Juvinas. The V/Ti, Ca/Ti, Cr/Ti, and Zr/Ti ratios in the Ti fraction were $<2 \times 10^{-3}$, $<2 \times 10^{-3}$, $<4 \times 10^{-4}$, and $<9 \times 10^{-5}$ for the studied samples,

except JP-1, and Allende, for which the Ca/Ti, and Cr/Ti ratios were as high as 2×10^{-2}. The relatively elevated Ca/Ti and Cr/Ti ratios in the Ti cuts of JP-1, and Allende inherit from the original sample compositions. Blank measurements yielded values of 970 pg Cr in the 12 mol l^{-1} HNO_3 fraction and 170 pg Ti in the 12 mol l^{-1} HNO_3 + 1wt% H_2O_2 fraction.

Column 3

In column 3, V and Na were removed immediately during the initial loading. Subsequent elution with 0.7 mol l^{-1} HNO_3 removed the Mg, Ni, Mn, and Ca from the resin (Fig. 5c). In addition, trace amounts of Cr were eluted during this step because of the incomplete transformation of Cr into its trivalent form. However, the proportion of eluted Cr in this step was no more than 4% with trace amounts of Cr remaining on the column. Al was removed in the additional loading of 0.5 mol l^{-1} HF. Finally, Cr was collected in 4 ml of 6 mol l^{-1} HCl. The Ti/Cr, V/Cr, and Fe/Cr ratios in the Cr fraction were $0.6–1.9 \times 10^{-5}$, $1.4–2.4 \times 10^{-6}$, and $1.5–3.5 \times 10^{-5}$, respectively. The recovery rates of Cr were 97%–100% for JB-1b, 91% for JP-1, and 83%–100% for Juvinas. Typical blank amounts of Cr were 1–2 ng.

These three chemical separation steps decreased the amounts of elements causing problematic spectral interferences to be sufficiently low in the Cr and Ti cuts for all studied samples. The residual Ti, V, and Fe in the Cr fraction induced interferences of <0.01 ppm of ^{50}V and <1 ppm of ^{50}Ti on $^{50}Cr/^{52}Cr$ and typically on the order of 10 ppm

of ^{54}Fe on $^{54}Cr/^{52}Cr$ during TIMS measurements, only the latter of which requires the interference correction. On the other hand, the remaining Ca, V, and Cr in the Ti fraction caused interferences of 0.3–14 ppm of ^{46}Ca on $^{46}Ti/^{47}Ti$, 1.6–75 ppm of ^{48}Ca on $^{48}Ti/^{47}Ti$, and 0.2–11 ppm of ^{50}V and 12–650 ppm of ^{50}Cr on $^{50}Ti/^{47}Ti$ during MC-ICPMS measurements, which can be accurately corrected for by our analytical protocol (Fig. 4). Total procedural blanks, including a Teflon® bomb digestion blank, were typically 3–5 ng for Cr and 2–3 ng for Ti.

Additional Column

In the additional column, Na, Mg, Cr, Ca, Mn, Ni, and Al were removed immediately in the initial loading and an additional 10 ml of 4 mol l^{-1} HF (Fig. 5d). Subsequently, V was eluted with 12 ml of 0.4 mol l^{-1} HCl + 1 mol l^{-1} HF. The recovery rates for Ti were >98% for all samples including JP-1, and Allende. The V/Ti, Ca/Ti, and Cr/Ti ratios in the collected Ti fraction were $<4 \times 10^{-5}$, $<2 \times 10^{-4}$, and $<2 \times 10^{-4}$, respectively. Blank measurements yielded ~200 pg Ti in the 1 mol l^{-1} HCl + 2wt% H_2O_2 fraction.

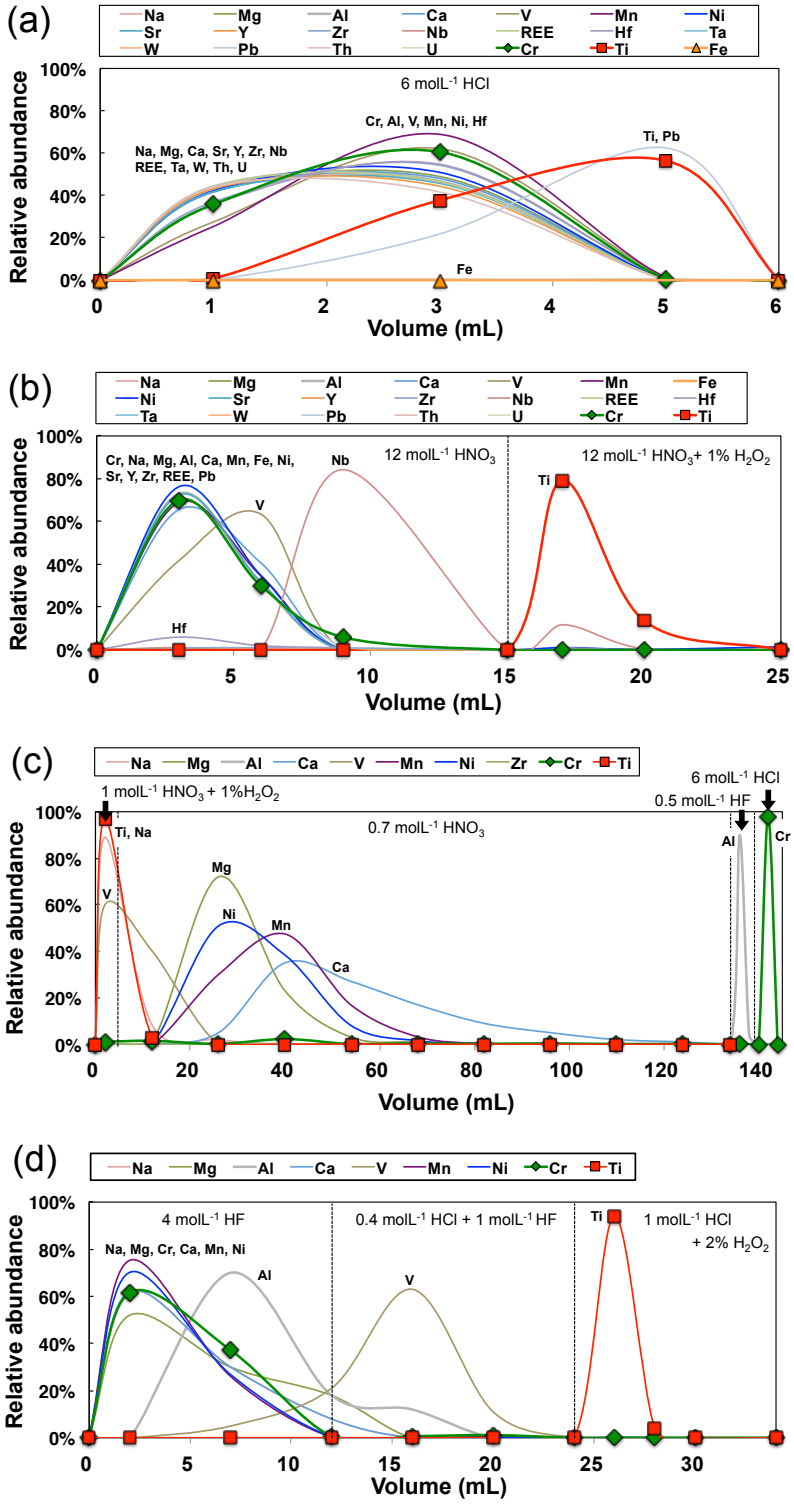

Fig. 5. Elution curves of (a) Step 1 for Fe removal using AG1-X8, (b) Step 2 for Ti separation using TODGA resin, (c) Step 3 for Cr purification using AG50W-X8, and (d) the additional step for Ti purification using AG1-X8.

2. 3. 2. Isotope data

The results of the Cr isotope analysis are reported in Table 4 and illustrated in Figure 6. The ratios obtained for the column-processed Cr standard and terrestrial samples (JB-1b and JP-1) are all identical to those for the standard within analytical uncertainty. The meteorite samples show variable values of ε^{53}Cr and ε^{54}Cr. Two fractions of Allende carbonaceous chondrite have identical Cr isotope compositions, with slightly positive ε^{53}Cr values of 0.03 ± 0.07 and 0.09 ± 0.06 and markedly elevated ε^{54}Cr values of 0.76 ± 0.07 and 0.81 ± 0.09. The Juvinas analyses are characterized by the highest ε^{53}Cr values among our samples and negative ε^{54}Cr values. The ε^{53}Cr and ε^{54}Cr values of the five individual fractions of Juvinas overlap within analytical uncertainty, with average values 0.82 ± 0.13 (2 S.D.) and −0.63 ± 0.13 (2 S.D.), respectively.

The results of the Ti isotope analysis are presented in Table 4 and illustrated in Figure 7. All the Ti isotope ratios obtained for the chemically processed Ti standard (NIST 3162a) and terrestrial samples (JB-1b and JP-1) are identical to those for the bracketing standard within analytical uncertainty. For ^{48}Ti/^{47}Ti, all meteorite samples display indistinguishable values from the standard, consistent with the results of (Trinquier et al. 2009). In contrast, the meteorite samples show variable ^{46}Ti and ^{50}Ti anomalies. The two fractions of Allende have identical Ti isotope ratios within analytical uncertainty. The ε^{50}Ti values of 3.50 ± 0.22 and 3.33 ± 0.23 and ε^{46}Ti values of 0.61 ± 0.17 and 0.64 ± 0.14 are the highest among the studied samples. The five

fractions of Juvinas have negative ε^{50}Ti and ε^{46}Ti values with averages of −1.31 ± 0.08 (2 S.D.) and −0.35 ± 0.10 (2 S.D.), respectively.

Table 4.
Summary of Cr and Ti isotope data for the column-processed standards (High-purity Cr-standard and NIST3162a), terrestrial (JB-1b and JP-1), and meteorite samples (Allende and Juvinas).

Sample		ε^{53}Cr	ε^{54}Cr	ε^{46}Ti	ε^{48}Ti	ε^{50}Ti
Column processed standards						
High purity Cr-standard		–0.03 ± 0.09	0.02 ± 0.09	—	—	—
NIST 3162a		—	—	0.01 ± 0.10	0.05 ± 0.07	–0.10 ± 0.10
Terrestrial samples						
JB-1b		–0.02 ± 0.09	–0.02 ± 0.10	–0.01 ± 0.15	–0.03 ± 0.07	0.05 ± 0.16
JP-1		–0.04 ± 0.07	0.00 ± 0.07	–0.10 ± 0.27	0.09 ± 0.15	–0.22 ± 0.31
Meteorite samples						
Allende	#1	0.03 ± 0.07	0.76 ± 0.07	0.61 ± 0.17	–0.04 ± 0.08	3.50 ± 0.22
	#2	0.09 ± 0.06	0.81 ± 0.09	0.64 ± 0.14	–0.04 ± 0.06	3.33 ± 0.23
Juvinas	#1	0.90 ± 0.08	–0.58 ± 0.08	–0.37 ± 0.13	0.02 ± 0.05	–1.27 ± 0.13
	#2	0.83 ± 0.08	–0.60 ± 0.07	–0.33 ± 0.17	–0.04 ± 0.07	–1.32 ± 0.18
	#3	0.74 ± 0.09	–0.74 ± 0.08	–0.36 ± 0.17	–0.06 ± 0.07	–1.35 ± 0.18
	#4	0.78 ± 0.05	–0.63 ± 0.09	–0.42 ± 0.16	–0.05 ± 0.07	–1.25 ± 0.17
	#5	0.87 ± 0.08	–0.61 ± 0.08	–0.29 ± 0.17	–0.04 ± 0.07	–1.33 ± 0.18
Juvinas average		0.82 ± 0.13	–0.63 ± 0.13	–0.35 ± 0.09	–0.03 ± 0.06	–1.31 ± 0.09

Errors are propagated to include the internal errors and the uncertainty in the isotope normalization to the standards.

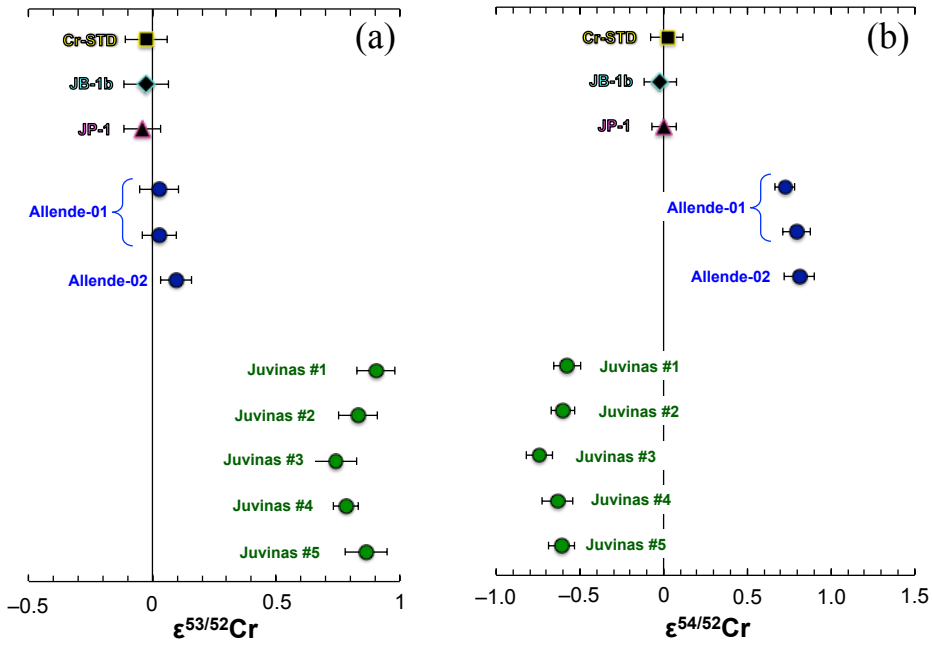

Fig. 6. Obtained (a) ε^{53}Cr and (b) ε^{54}Cr values for the column-processed Cr standard, JB-1b, JP-1, Allende, and Juvinas (5 fractions).

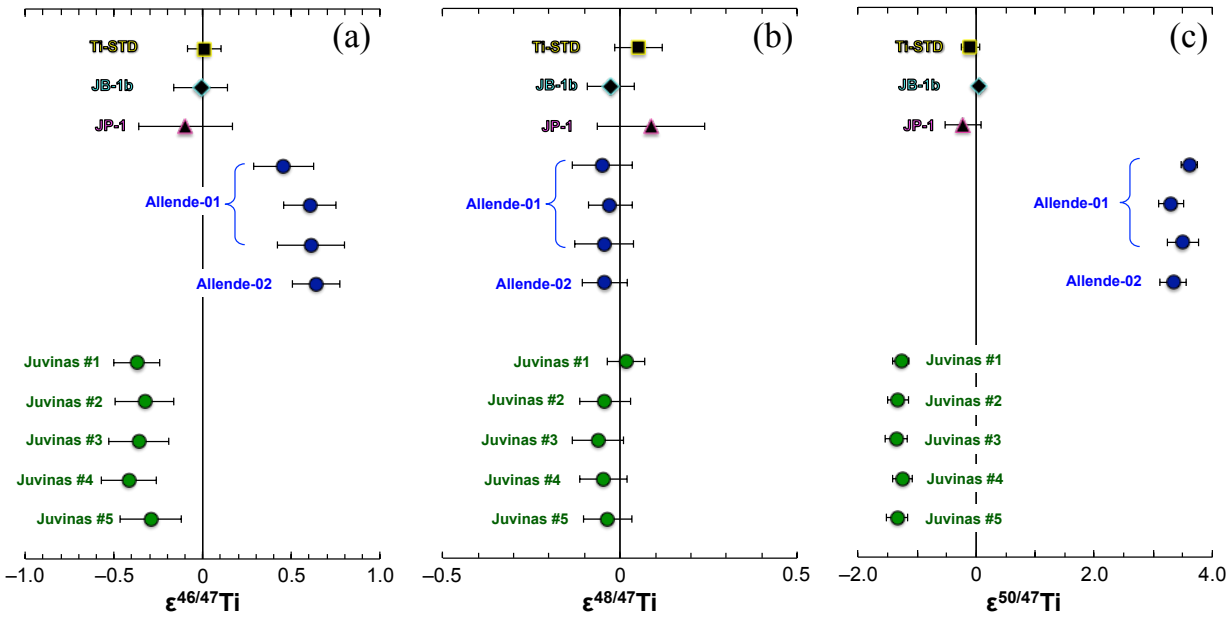

Fig. 7. Obtained (a) ε^{46}Ti, (b) ε^{48}Ti, and (c) ε^{50}Ti values for the column-processed Ti standard, JB-1b, JP-1, Allende (2 fractions), and Juvinas (5 fractions).

2. 3. 3. Validation of the method

Our Cr and Ti isotope analyses of the chemically processed standards and terrestrial standard rocks (JB-1b and JP-1) yielded Cr and Ti isotope ratios identical to those for the bracketing standards (Figs. 6 and 7). The consistency verifies that the application of the entire technique, including sample digestion, column chromatography and isotope analyses, does not induce any mass-independent fractionation for Cr and Ti. The meteorite samples studied here were analyzed previously for Cr and Ti isotope compositions, individually. Our Cr and Ti isotope data for the Juvinas eucrite are in good agreement with the previously reported results: $\varepsilon^{53}Cr = 0.65 \pm 0.08$ to 0.93 ± 0.10 and $\varepsilon^{54}Cr = -0.71 \pm 0.12$ to -0.55 ± 0.19 (Trinquier et al. 2007, 2008a, Bonnand et al. 2016b); $\varepsilon^{46}Ti = -0.32 \pm 0.06$ to -0.21 ± 0.09, $\varepsilon^{48}Ti = -0.04 \pm 0.13$ to -0.02 ± 0.05, and $\varepsilon^{50}Ti = -1.33 \pm 0.14$ to -1.25 ± 0.05 (Zhang et al. 2011, 2012). Similarly, the Cr and Ti isotope ratios obtained from the Allende carbonaceous chondrite are within the ranges of previously reported variable ratios that are indicative of isotope heterogeneity: $\varepsilon^{53}Cr = 0.10 \pm 0.09$ to 0.14 ± 0.10 and $\varepsilon^{54}Cr = 0.86 \pm 0.09$ to 1.04 ± 0.19 (Shukolyukov and Lugmair 2006a, Trinquier et al. 2007, Qin et al. 2010, Bonnand et al. 2016b, Burkhardt et al. 2017); $\varepsilon^{46}Ti = 0.53 \pm 0.28$ to 0.94 ± 0.11, $\varepsilon^{48}Ti = -0.10 \pm 0.08$ to 0.55 ± 0.07, and $\varepsilon^{50}Ti = 3.27 \pm 0.16$ to 5.01 ± 0.29 (Trinquier et al. 2009, Zhang et al. 2011, 2012, Burkhardt et al. 2017, Gerber et al. 2017) (Fig. 8).

Methods for individual separation of Cr and Ti were established in previous studies (e.g., Schoenberg et al. 2008, Frei et al. 2009, Trinquier et al. 2009, Bonnand et

al. 2011, Zhang et al. 2011, Reinhard et al. 2014, Schiller et al. 2014, Cole et al. 2016, Gueguen et al. 2016). However, the simple combination of these procedures can result in relatively low Cr yields (~70%), especially for samples having high Fe/Cr, Ti/Cr, and V/Cr (Wang et al. 2016). Note also that the double-spike technique used in the previous Cr isotopic studies (e.g., Schoenberg et al. 2008, Bonnand et al. 2016b) are not favorable for the combined Cr and Ti isotope analyses of single digest because the addition of the widely used ^{50}Cr-enriched spike increases the level of isobaric interference on ^{50}Ti and, in turn, the uncertainty of measured ε^{50}Ti. Recently, Larsen et al. (2018) reported an ion-exchange chromatography for combined isotope analysis of Mg and Ti, which is applicable to Cr isotope analysis as well. Yet, the sequential chemical separation scheme developed here allows us to extract Cr and Ti with fewer steps than in Larsen et al. (2018) and other previous studies (i.e., three steps for both Cr and Ti elution compared with two to five steps for each individual element extraction; *e.g.* Trinquier et al. 2008a, Wombacher et al. 2009, Yamakawa et al. 2009, Zhang et al. 2011, Schiller et al. 2014).

The present method enables the combined isotope analyses of 3 μg of Cr and 1.5 μg of Ti. These amounts correspond to single ~1 mm chondrules and ~2 mm CAIs, assuming typical Cr and Ti abundances (~2000 ppm Cr and ~1000 ppm Ti for chondrules; Hezel et al. 2018 and ~200 ppm Cr and ~5400 ppm Ti for CAIs; Trinquier et al. 2009). Such combined analyses of the isotopes of primitive meteorite components will facilitate understanding of the nature and evolution of the protoplanetary disk. Furthermore, the application of our new method to various types of planetary materials

could provide new constraints on their genetic relationship.

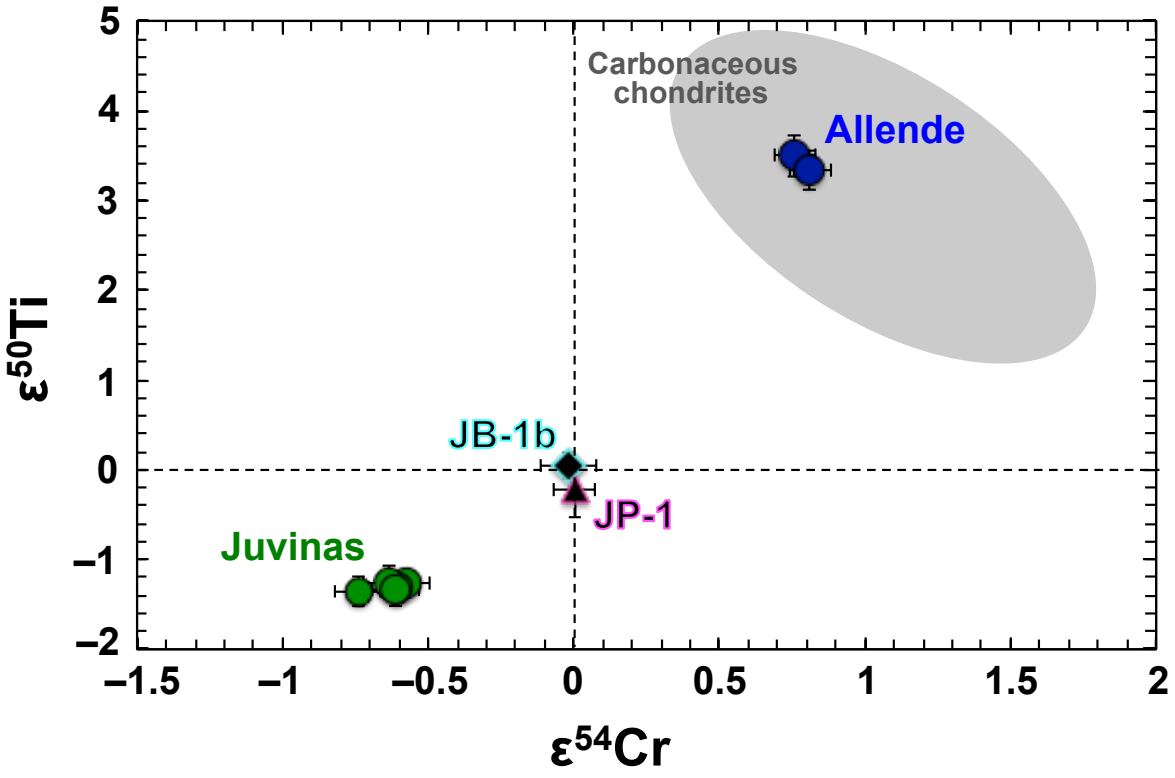

Fig. 8. Plot of ε^{50}Ti versus ε^{54}Cr for JB-1b, JP-1, Allende (2 fractions), and Juvinas (5 fractions). Data sources for the shaded region of carbonaceous chondrite are as follow: ε^{54}Cr, Yamashita *et al.* (2005), Shukolyukov and Lugmair (2006), Trinquier *et al.* (2007), Yamakawa *et al.* (2009), Qin *et al.* (2010), Larsen *et al.* (2011), Petitat *et al.* (2011), Sanborn *et al.* (2014), Göpel *et al.* (2015), Bonnand *et al.* (2016), Schoenberg *et al.* (2016) and Van Kooten *et al.* (2016); ε^{50}Ti, Leya *et al.* (2008), Trinquier *et al.* (2009), Qin *et al.* (2010), Jenniskens *et al.* (2012) and Zhang *et al.* (2012).

2. 4. Conclusion

A sequential Cr and Ti separation procedure has been developed, which consists of three steps: (i) Fe removal using AG1-X8 anion exchange resin, (ii) Ti separation using TODGA resin, and (iii) Cr separation using AG50W-X8 cation exchange resin (with one additional step of Ti purification using AG1-X8 anion exchange resin only for samples having high Cr/Ti and Ca/Ti ratios). Both the utility and the validity of the method have been verified by its application to compositionally varied terrestrial and meteorite samples, including terrestrial basalt JB-1b, terrestrial peridotite JP-1, Allende carbonaceous chondrite, and Juvinas non-cumulate eucrite. The achieved recovery rates were typically 90%–100% with total blanks of 3–5 ng for Cr and 2–3 ng for Ti. The Cr and Ti isotope compositions measured for the separated terrestrial samples were identical to those of the standards within analytical uncertainty. By contrast, the $\varepsilon^{53,54}$Cr and $\varepsilon^{46,50}$Ti values obtained for the meteorite samples were variable and they compared well with previously published individual Cr and Ti isotope datasets. These results demonstrate that the developed method enables combined high-precision Cr and Ti isotope analyses of single digests of planetary materials, highlighting its potential application to various samples ranging from basaltic and peridotitic rocks to single components of primitive meteorites.

3. Origin of NWA 6704

3. 1. Background

A fundamental and long-standing issue in planetary science is determining when, where, and how asteroids formed and differentiated (e.g., Ringwood 1961; Anders and Goles 1961; Mason 1967; Weiss and Elkins-Tanton, 2013; Day, 2015). Information regarding this must come from meteorites that record the early histories of their respective asteroidal parent bodies. Primitive achondrites are meteorites that have near-chondritic bulk compositions, but exhibit igneous and/or metamorphic textures (Prinz et al., 1980, 1983; Benedix et al., 1998; Weisberg et al., 2006; Rubin, 2007). They include several meteorite groups such as acapulcoites, lodranites, and winonaites (Weisberg et al., 2006; Greenwood et al., 2012). These meteorites record variable stages in the transition from chondrites to differentiated achondrites, from high degrees of metamorphism and anatexis of chondritic protoliths (acapulcoites and winonaites, e.g., Mittlefehldt et al., 1996; McCoy et al., 1996; Benedix et al., 1998; Floss et al., 2008), to various degrees of partial melting and melt extraction (lodranites as well as ureilites and brachinites, e.g., Goodrich, 1992; Mittlefehldt et al., 1996; Rubin, 2006; Warren et al., 2006; Keil, 2014). Moreover, shared O isotopic compositions and other similarities suggest that acapulcoites–lodranites and winonaites–IAB complex iron meteorites may share common parent bodies, respectively (e.g., McCoy et al., 1993; Benedix et al., 1998, 2005; Floss et al., 2008). Thus, primitive achondrites provide an important

opportunity to bridge the gap between chondrites and differentiated achondrites, and to decipher the thermal histories of (partially) undifferentiated planetesimals.

Recently, it has been found that several ungrouped achondrites, that are not classified into any known meteorite groups, also have near-chondritic major element compositions together with prominent igneous textures (e.g., Day et al., 2009, 2015; Gardner-Vandy et al., 2012; Warren et al., 2013). Such ungrouped achondrites are of importance for investigating the diversity of asteroids, and for refining our current understanding of early solar system evolution gained from grouped achondrites. Studies of ungrouped achondrites, however, are limited.

In this study, we conducted petrologic observations, geochemistry including highly siderophile element (HSE: Re, Os, Ir, Ru, Pt, Pd) abundances, ^{187}Re–^{187}Os systematics, and O–Cr–Ti isotope systematics (Fig. 3) for NWA 6704. The results allow us to constrain the crystallization process of this unique achondrite, the nature and provenance of its parental body and by extension, the implication for the origin of primitive achondrites. On the basis of the results and discussion, we lastly discuss whether this meteorite can be used as "*Time anchor*".

3. 2. Methods

3. 2. 1. Petrology

We prepared nine polished thin sections from four fragments of NWA 6704 for petrologic studies, (Table 5; TS-1 and -2 from fragment #1, TS-3–5 from fragment #2, TS-6 and -8 from fragment #3, and TS-7 and -9 from fragment #4). Petrologic analyses were carried out by means of optical and electron microscopies at the University of Tokyo and National Institute of Polar Research, Japan. Optical microscopy was performed using a *Nikon ECLIPSE E600W* polarizing optical microscope equipped with *Axiocam-MR* camera and *Axiovision 4* software. More detailed observation was conducted using a *JEOL JXA-7000F* field emission-scanning electron microscope equipped with an energy dispersive spectrometer (FE-SEM/EDS). Analytical conditions were 15 kV accelerating voltage, 10 mm working distance, and 12 nA specimen current. Major element compositions of minerals were determined using a *JEOL JXA-8530L* electron probe micro analyzer (EPMA) with 15–25 kV accelerating voltages, 11 mm working distance, and 12–20 nA specimen currents. Elemental maps were acquired for the four thin sections (TS-6–9) using *JEOL JXA-8900L* EPMA with 15 kV accelerating voltages and 80 nA specimen current. The entire thin sections of TS-6 and TS-7 were mapped for characterization of their textural features and determination of modal abundances. Crystallographic orientations in the two thin sections were further investigated by FE-SEM combined with an electron back-scattering diffraction (EBSD)

detector (*JEOL JSM 7000F* and *7100F* FE-SEM/EBSD) with the *HKL Channel-5* data acquisition and processing software. The EBSD technique allows us to determine the crystallographic orientations from Kikuchi patterns regardless of mineral phase contents (Schwartz et al., 2009). The instruments were operated at an accelerating voltage of 15 kV, a working distance of 25 mm, and a beam current of 10 nA. Orientation maps were created for orthopyroxene by scanning the sample (108–200 μm step), in which orientations are coded according to Euler color. Pole figure diagrams for {100} of orthopyroxene were obtained by processing the data. To characterize the spatial distribution of minerals in NWA 6704, we performed micro X-ray computed tomography (CT) using a ScanXmate-D180RSS270 at Tohoku University, Japan. A sample chip of NWA 6704 (2.4 × 12.4 × 16.7 mm) was scanned using an X-Ray beam at 130 kV and 120 μA, with isotropic voxels (3-D pixels) of 12.093 μm. X-rays were filtered with 1 mm copper filter. We used the Amira 6.0 reconstruction software to recreate 3D images from the obtained 600–1600 2D slice images.

3. 2. 2. Major and trace element geochemistry

For major element geochemistry, a ~4 g fragment of NWA 6704 (fragment #5) was disaggregated using an agate mortar and pestle. Approximately 200 mg of the sample powder was fused in a mixture of sample powder and $Li_2B_4O_7$ to form a glass disk, on which the major element abundance determination was carried out using a

ThermoARL Advant'XP+ sequential X-ray fluorescence (XRF) spectrometer at the Washington State University (WSU) Geoanalytical Laboratory. Major elements were normalized on a volatile-free basis with total Fe expressed as FeO.

For solution-based bulk and mineral chemistry measurement, two fusion-crust free subsamples of NWA 6704 (fragment #3: 678 mg, fragment #6: 42.9 mg) were powdered in an agate mortar and pestle. In addition to NWA 6704, an aliquot of NWA 6693 (39.5 mg) was also prepared for bulk chemistry measurement. Four powdered whole rock fractions of NWA 6704 (50.2mg, 50.1mg, 51.6 mg aliquots of fragment #3-a,b,c, and whole aliquot of fragment #6) and the NWA 6693 aliquot were digested with a concentrated 3:1 HF–HNO_3 mixture in a Parr® digestion bomb at 190 °C for 96 hs. Besides, plagioclase and orthopyroxene mineral separates of NWA 6704 were digested a concentrated 3:1 HF–HNO_3 mixture on a hot plate. Digestion was followed by a treatment with alternating solution of 6 mol l^{-1} HCl and concentrated HNO_3 for conversion to a soluble form. Aliquots of fragment #3 were diluted by a factor of 500 in 0.5 mol l^{-1} HNO_3 for trace elements using a Thermo Fisher Scientific™ iCAP Q™ ICP–MS at the University of Tokyo. Aliquots of NWA 6704-fragment #6 and mineral separates and NWA 6693 were diluted in 2% HNO_3 for trace/minor and major elements using a *Thermo Fisher Scientific Element XR* high-resolution inductively coupled plasma mass spectrometer (ICP-MS) at the University of California at Davis. Sample dilution factors were 4,500 and 95,000 for trace/minor and major elements, respectively. Analyses were made in low-, medium-, or high-resolution, based on the resolution conditions needed for a given element. The accuracy was evaluated by analyzing

well-characterized terrestrial rock standards (BHVO-2 and JB-1b) and Murchison meteorite dissolved in the same manner as NWA 6704. These results are reported in Table 6 together with literature values (Jarosewich, 1971; Terashima et al., 1998; Friedrich et al., 2002; Makishima et al., 2006; Jochum et al., 2015; Kon and Hirata, 2015).

Table 5: Summary of six NWA 6704 fragments used for petrologic studies

Fragments	**#1**		**#2**			**#3**		**#4**		**#5**	**#6**
Thin section number	TS-1	TS-2	TS-3	TS-4	TS-5	TS-6	TS-8	TS-7	TS-9	—	—
Lithology	fine	coarse	coarse	coarse	coarse	fine	fine	coarse	coarse	—	—
Optical microscopy/SEM observation	○	○	○	○	○	○	○	○	○	×	×
Major element composition of minerals (EPMA)	○	○	○	○	○	○	○	○	○	×	×
Crystallographic orientations (EBSD)	×	×	×	×	×	○	×	○	×	×	×
Solution-based bulk chemistry (ICP-MS)	×	×	×	×	×	○	○	×	×	×	○
Whole rock major element geochemistry (XRF)	×	×	×	×	×	×	×	×	×	○	×
Elemental maps (EPMA)	×	×	×	×	×	○	○	○	○	×	×
diameter of the electron probe spot						φ26μm	φ25μm	φ28μm	φ23μm		
the number of mapping points						700 × 1000	645 × 1000	750 × 1000	790 × 1000		
the mapped area						18 mm × 26 mm	18 mm × 28 mm	21 mm × 28 mm	22 mm × 28 mm		
measured time						45 hours	43.5 hours	48 hours	44 hours		

Table 6: Major and trace element abundances determined in BHVO and Murchison by ICPMS

Sample		BHVO	[a] BHVO-Ref	% Deviation	Murchison	[b, c] Murchison-Ref	% Deviation	JB-1b	[d, e, f] JB-1b-Ref	% Deviation
mass										
Na	wt%	1.61	1.65	-2.6						
Mg	wt%	4.24	4.38	-3.3						
Al	wt%	7.09	7.11	-0.3						
Ca	wt%	8.27	8.15	1.5	*No Murchison major element ref available*					
Cr	wt%	0.03	0.03	1.3						
Fe	wt%	8.74	8.67	0.8						
Ni	wt%	0.01	0.01	-1.7						
Li	µg/g	4.642	4.500	3.2	1.359	1.400	-3.0	11.492	11.5	-0.1
Be	µg/g	1.093	1.076	1.6	0.042	0.040	3.9	1.462	1.44	1.5
Sc	µg/g	32.564	31.83	2.3	8.272	8.180	1.1	29.640	30.2	-1.9
Ti	µg/g	16495.73	16400	0.6	655.05	650.00	0.8			
Mn	µg/g	1298.6	1300	-0.1	1802.4	1730.0	4.2			
V	µg/g	309.05	318.2	-2.9	67.55	68.00	-0.7			
Co	µg/g	45.13	44.89	0.5	562.76	544.00	3.4			
Cu	µg/g	126.47	129.3	-2.2	135.08	140.00	-3.5	51.51	53.2	-3.2
Rb	µg/g	9.300	9.261	0.4	1.211	1.170	3.5	35.352	34.0	4.0
Sr	µg/g	397.495	394.100	0.9	8.285	8.400	-1.4	454.632	444	2.4
Y	µg/g	25.846	25.910	-0.2	2.322	2.350	-1.2	20.510	21.3	-3.6
Zr	µg/g	178.538	171.200	4.3	6.780	6.900	-1.7	126.646	123.1	2.9
Nb	µg/g	17.797	18.100	-1.7	0.437	0.440	-0.7	26.153	26.7	-1.9
Mo	µg/g	3.881	4.070	-4.6	1.826	1.800	1.4			
Sn	µg/g	1.856	1.776	4.5	0.853	0.890	-4.2			
Te	µg/g	0.014	0.014	-3.0	1.651	1.600	3.2			
Cs	µg/g	0.102	0.100	2.4	0.123	0.124	-0.7			
Ba	µg/g	125.985	130.900	-3.8	2.940	2.850	3.2			
La	µg/g	15.276	15.200	0.5	0.327	0.316	3.6	39.377	39.1	0.7
Ce	µg/g	37.884	37.530	0.9	0.867	0.840	3.2	68.357	67.2	1.7
Pr	µg/g	5.405	5.339	1.2	0.132	0.130	1.2	7.101	7.08	0.3
Nd	µg/g	24.368	24.270	0.4	0.628	0.616	1.9	26.480	26.6	-0.5
Sm	µg/g	6.060	6.023	0.6	0.221	0.216	2.5	4.914	4.86	1.1
Eu	µg/g	2.015	2.043	-1.4	0.079	0.076	3.3	1.471	1.437	2.4
Gd	µg/g	6.119	6.207	-1.4	0.292	0.284	2.7	4.754	4.90	-3.0
Tb	µg/g	0.946	0.939	0.8	0.057	0.055	3.7	0.696	0.669	4.0
Dy	µg/g	5.292	5.280	0.2	0.298	0.290	2.8	4.029	3.99	1.0
Ho	µg/g	1.000	0.989	1.1	0.075	0.074	0.9	0.800	0.776	3.0

Er	µg/g	2.565	2.511	2.1	0.220	0.216	2.0	2.239	2.21	1.3
Tm	µg/g	0.341	0.335	1.8	0.037	0.037	-0.4	0.306	0.302	1.3
Yb	µg/g	2.045	1.994	2.5	0.216	0.211	2.3	1.983	1.92	3.3
Lu	µg/g	0.288	0.275	4.6	0.039	0.039	0.9	0.291	0.278	4.5
Hf	µg/g	4.364	4.470	-2.4	0.160	0.161	-0.4	3.314	3.31	0.1
Ta	µg/g	1.132	1.154	-1.9	0.176	No ref	n/a	1.512	1.484	1.9
W	µg/g	0.261	0.251	4.2	0.144	0.150	-4.1			
Tl	µg/g	0.023	0.022	1.1	0.088	0.090	-2.0			
Pb	µg/g	1.513	1.553	-2.6	1.584	1.600	-1.0	5.744	5.59	2.7
Th	µg/g	1.219	1.224	-0.4	0.045	0.043	4.3	9.080	9.30	-2.4
U	µg/g	0.402	0.412	-2.4	0.010	0.010	-1.1	1.603	1.67	-4.0

[a] BHVO values from Jochum et al. (2015).

[b,c] Murchison values from Jarosewich (1971) and Friedrich et al. (2002).

[d,e,f] JB-1b values from Terashima et al. (1998), Makishima et al. (2006), and Kon and Hirata (2015).

3. 2. 3. Highly siderophile element and Re–Os isotope analysis

Four bulk fragments as well as a non-magnetic and magnetic separates were analyzed for highly siderophile element abundances (Re, Os, Ir, Ru, Pt, Pd) and ^{187}Re–^{187}Os isotope systematics. Approximately 70 mg of bulk fragments and a non-magnetic (primarily silicate) fraction were crushed into fine powders using an agate mortar and pestle. The magnetic fraction, containing mostly FeNi-rich metal, could not be crushed, and was dissolved as whole grains. Samples were combined with ~5 mL of a 2:1 mixture of distilled, concentrated HNO_3 and HCl, and appropriate amounts of two isotopic spikes, one enriched in ^{185}Re and ^{190}Os, the other enriched in ^{191}Ir, ^{99}Ru, ^{194}Pt, and ^{105}Pd. Samples, spikes, and acids were sealed in 8 mL *Pyrex*™ Carius tubes (Shirey and Walker, 1995) and heated at 260 ºC for three days. After digestion, Os was extracted from the acid by solvent extraction using CCl_4, and back extraction into concentrated HBr (Cohen and Waters, 1996). The Os was then purified using a microdistillation technique from a dichromate solution into concentrated HBr (Birck et al., 1997). The remaining HSE (Re, Ir, Ru, Pt, and Pd) were separated and purified via anion exchange chromatography using 10 mL *Bio-Rad* columns loaded with ~1 mL of AG1-X8 anion exchange resin (Rehkämper and Halliday, 1997).

Purified Os was analyzed by negative thermal ionization mass spectrometry (N-TIMS) on either the University of Maryland (UMd) *VG Sector 54* or *Thermo-Fisher Triton* using Faraday cups. The Os solutions were dried onto Pt filaments and then a $Ba(OH)_2$ activator was added (Creaser et al., 1991). The other HSE were analyzed as

solutions by multicollector-ICP-MS (MC-ICP-MS) on the *Nu Plasma* at University of Maryland (UMd) using Faraday cups. The measurements of Ir, Ru, Pt, and Pd were corrected for mass bias by interspersing standards with sample measurements. Tungsten was added to Re fractions and mass bias corrections were made using $^{184}W/^{186}W$ = 1.0780 (Kleine et al., 2004).

Mean (N = 2) blanks were 1.3 ± 1.3 pg for Re, 1.6 ± 0.8 pg for Os, 0.7 ± 0.4 pg for Ir, 2.3 ± 0.3 pg for Ru, 4.3 ± 4.0 pg for Pt, and 4.6 ± 4.6 pg for Pd. The Os blank correction was 1.4% for the silicate fraction, and less than 0.12% for all other fractions. Blank corrections of Re, Pt, and Pd were 2.6%, 3.9%, and 1.5%, respectively, for the silicate fraction. All other blank corrections, including Ir and Ru blank corrections for the silicate fraction, were less than 0.1%. Uncertainties arising from blank corrections are included in reported uncertainties. The total uncertainties for Ir, Ru, Pt, and Pd concentrations of bulk and magnetic fractions are ≤1%. For the Re and Os concentrations of bulk and magnetic fractions, uncertainties are less than 0.2% and 0.1%, respectively. The total uncertainties for HSE concentrations of silicate fractions are all less than 5%.

3. 2. 4. Oxygen isotope analysis

A ~550 mg fragment of NWA 6704 was crushed in a silicon nitride mortar and pestle, then sieved. The grain size of constituent minerals of NWA 6704 ranged up to

centimeter length. To reduce the heterogeneity in the mineral proportion among the analyzed sample aliquots, a mineral fraction of 73–120 μm in diameter was used for the analyses. The fraction was washed in high purity water three times and dried at 80 ºC overnight. After drying, metal grains were magnetically removed from the fractions. Since no weathered material was identified in the separated fraction under the microscope, no further cleaning was performed.

The O isotope analyses were conducted on five separates using the fluorination and gas purification methods modified after Sharp (1990) at the Institute for Planetary Materials, Okayama University. Details of the method are described in Tanaka and Nakamura (2013) and Pack et al. (2016). About 1–2 mg of sample was placed in a Ni sample holder. To remove the absorbed moisture, the sample was baked at 170 ºC for 6 hs *in vacuo*, then prefluorinated with BrF_5 for 1 h before analysis. The O_2 was extracted from each sample using a CO_2 laser (*PIN-10R*, Onizca Glass, Japan) with BrF_5 as oxidation agent. Extracted oxygen was then purified and trapped with 13 Å molecular sieve at liquid nitrogen temperature. Total procedural O_2 blanks for the laser fluorination method were typically <20 ppm relative to the sample gas. Thus, no blank correction was performed. The isotope ratios in the purified O_2 gases were determined using a *Thermo Finnigan* MAT253 gas source mass spectrometer with the dual inlet mode. Each sample measurement comprised 8 blocks of 11 cycles with a total measurement time of ~90 minutes. The $^{18}O/^{16}O$ and $^{17}O/^{16}O$ of the samples are expressed as the common delta (δ) notation relative to VSMOW as $\delta^{17 \text{ or } 18}O = 10^3 \times [(^{17 \text{ or } 18}O/^{16}O)_{sample} / (^{17 \text{ or } 18}O/^{16}O)_{VSMOW} - 1]$ using a VSMOW-SLAP scale. The excess ^{17}O

values relative to terrestrial silicate fractionation line (TSFL) are defined as $\Delta^{17}O = 10^3 \times [\ln(\delta^{17}O^* \times 10^{-3} + 1) - 0.527 \times \ln(\delta^{18}O \times 10^{-3} + 1)]$, where $\delta^{17}O^* = \delta^{17}O + 0.039$ (Tanaka and Nakamura, 2013; Pack et al., 2016). Since most of the laboratories for O isotope analysis do not calibrate the working gas by VSMOW-extracted oxygen, it is widely assumed that the $\Delta^{17}O$ value of VSMOW is the same as that of the so-called terrestrial fractionation, i.e. $\Delta^{17}O = 0$, (Tanaka and Nakamura, 2013). The $\delta^{17}O^*$ value defined in this study corresponds to the $\delta^{17}O$ value so far published by other laboratories unless otherwise mentioned. The precision and accuracy during the course of this study were monitored by analyzing the San Carlos olivine (MSOL-1), which yielded $\delta^{18}O = 5.246 \pm 0.033$, $\delta^{17}O^* = 2.762 \pm 0.018$, and $\Delta^{17}O = 0.001 \pm 0.005$ (N = 5, 2 SD).

3. 2. 5. Chromium and titanium isotope analysis

For combined Cr and Ti isotope analysis, the new method developed in Chapter 2 was applied to NWA 6704. Approximately 50 mg fragment of NWA 6704 was disaggregated in an agate mortar. The disaggregated samples were washed in a distilled acetone ultrasonic bath for about 10 minutes, and then heated on a hotplate and evaporated to dryness. Sample was then digested following the method described in Chapter 2.2.2. The digested sample aliquot of NWA 6704 was divided into two fractions and individually processed for the column chromatography in Chapter 2.2.3. Chemical yields were 96-100% for Column 1; 98-100% for Column 2; 88-91% for

Column 3; and >98% for Additional Column.

The Cr and Ti isotope compositions of the separated sample were measured by thermal ionization mass spectrometry *a Thermo Fisher Scientific™ TRITON Plus™* TIMS, and *a Thermo Fisher Scientific™ Neptune Plus™* MC–ICPMS, respectively. Details of the method including sample digestion, chemical separation and purification of Cr and Ti, and high-precision Cr and Ti isotope ratio measurements by MC-ICP-MS and TIMS are described in Chapter 2.2.4.

3. 3. Results

3. 3. 1. Petrology

Northwest Africa 6704 is composed dominantly of large orthopyroxene grains, with smaller grains of Ni-rich olivine, feldspars (plagioclase and K-feldspar), chromite, NiFe-metal (awaruite), sulfides (heazlewoodite and pentlandite) and merrillite. The modal abundances of minerals were obtained for two thin sections (TS-6 and TS-7) from their phase maps obtained by X-ray intensity maps on the entire thin sections. The results are summarized in Table 7. The micro-CT images of individual minerals and the combined image of the major phases other than orthopyroxene are shown in Fig. 9a-e. As olivine and chromite have similar X-ray absorption coefficients, these minerals are shown together in Fig. 9b.

Table 7: Modal mineralogy of NWA 6704 thin sections (in vol.%).

vol.%	TS-6	TS-7
orthopyroxen	68.7	69.9
olivine	14.0	11.6
plagioclase	9.9	11.1
pigeonite	6.9	7.0
metal	0.34	0.27
spinel	0.16	0.14
phosphate	0.06	0.05
sulfide	minor	minor
Total	100.06	100.06

Orthopyroxene is identified by straight extinction under crossed nicols, EBSD patterns, and low CaO content. The size of orthopyroxene is mostly greater than a few mm and up to 1.7 cm in length. The grain size of orthopyroxene is highly variable on various scales and orthopyroxene grain larger than 0.5 cm is called as megacryst in this paper. Some of NWA 6704 fragments consist mostly of orthopyroxene megacrysts (TS-2–5, 7 and 9, termed as “coarse lithology”: Fig. 9a-e, 10a-c), whereas other fragments consist mostly of orthopyroxene with grain size 1 mm across on average and minor megacrysts (TS-1, 6 and 8, termed as “fine lithology”: Fig. 10d-f). Orthopyroxene megacrysts are either euhedral or subhedral. In the coarse lithology (Fig. 10a-c), the megacrysts are elongated parallel to the c-axes, and show a shape-preferred orientation (Fig. 11). In many places, the orthopyroxene megacrysts are in direct contact with each other without a clear interstitial part. Their boundaries are very irregular and

indented on a grain-size scale, and thus the adjacent megacrysts are interlocked with each other. Orthopyroxene megacrysts contain abundant euhedral olivine and anhedral plagioclase, which tend to occur in the marginal zone of megacrysts. Some megacrysts also enclose curvilinear trains of irregularly-shaped micro-bubbles (Fig. 12a and b) as well as tiny oval-shaped inclusions of chromite (Fig. 12c). Raman spectroscopy demonstrates that the clear to pinkish bubbles are now empty. Both sorts of included objects are localized in the core and/or mantle of megacrysts, and in some places, are aligned parallel along the earlier growth surface.

Minor amounts of pigeonite occur as a rim surrounding some orthopyroxene megacrysts with thicknesses of up to a few hundred μm. The pigeonite and surrounded orthopyroxene share the same c-axis orientation. Augite ($Fs_{17}En_{45}Wo_{39}$) occurs as exsolution lamellae in pigeonite. The lamellae have thickness up to ~0.1 μm with 1–2 μm spacing.

Plagioclase occurs mostly in orthopyroxene megacrysts as "inclusions" apparently isolated from each other in the coarse lithology, whereas it occurs along the grain boundaries or interstices of orthopyroxene and olivine grains in the fine lithology. Notably, plagioclase shares the same optical extinction positions over an area up to a few cm scale in both the coarse and fine lithologies. The EBSD analyses also indicate the identical lattice orientations of plagioclase over such area. Plagioclase often shows a cuspate morphology with extremely low dihedral angles of ≤40˚ against contacting two mafic crystals with distinct crystallographic orientations irrespective of their assemblage (plagioclase-olivine-orthopyroxene, plagioclase-olivine-olivine, etc.). The dihedral

angles are, however, greater than 60° on the scale of ~10 μm (Fig. 13–i). Some plagioclase domains enclosed in orthopyroxene megacrysts show rectangular morphology with both curvatures and straight interfaces with the host (Fig. 13–ii). Our EBSD analysis showed that such facets are parallel to c-axis of the adjacent orthopyroxene, and the shapes of plagioclase are consistent with [100], [010] and [001] axes of the orthopyroxene (Fig. 13). Moreover, some plagioclase domains have thin delicate maze-like morphology (Fig. 13–iii) extending into orthopyroxene megacrysts. These observations indicate that the apparently isolated grains of plagioclase are inter-connected with each other in three dimensions, which is recognizable in the obtained micro-CT image (Fig. 9d). Some plagioclase grains contain tightly clustered oval inclusions (Fig. 14), which tend to be aligned parallel to [100] axis of plagioclase, indicating that these inclusions were trapped during the crystallization of plagioclase. Twinning of plagioclase is vague and the wavy extinctions are not clearly observed. This indicates that NWA 6704 is unshocked to very weakly shocked, corresponding to shock stage S1 or S2 (Fritz et al., 2017).

Olivine occurs mostly as euhedral to subhedral grains with diameters from 50 μm to 1.7 mm and they are intimately associated with anhedral plagioclase. It shows sharp extinction under crossed-nicols, consistent with the low shock stage. Some olivine grains contain melt inclusions that are filled with glass containing bubbles and euhedral orthopyroxene skeletal crystals (Fig. 15a). In the coarse lithology, olivine is distributed in the outer parts of orthopyroxene megacrysts, rarely occurring along megacryst boundaries (Fig. 10c). In the fine lithology, the size of olivine is comparable to that of

orthopyroxene, and the olivine is rather homogeneously distributed with clear avoidance of core regions of orthopyroxene megacrysts (Fig. 10f). In both the coarse and fine lithologies, olivine occasionally occurs as anhedral vermicular inclusions within orthopyroxene megacrysts (Fig. 15b). These vermicular olivine inclusions occur only in one place near the center of each orthopyroxene megacryst (e.g., red circles in Fig. 10a-e). The number of orthopyroxene megacrysts containing such vermicular olivine inclusions tends to be smaller for the coarse lithology: The thin sections of the fine lithology have more than five orthopyroxene megacrysts including vermicular olivine, whereas the thin sections of the coarse lithology have only a few of them. The EBSD analysis reveals that these inclusions have twisted crystallographic orientations.

Chromite is euhedral to subhedral and its size ranges from 30 to 300 μm in diameter. It is mostly present in the marginal part of orthopyroxene megacrysts together with plagioclase and olivine and it is absent in the core regions of orthopyroxene megacrysts. In fine-grained areas of the fine lithology, it occurs along grain boundary of olivine, mostly associated with plagioclase. Inclusions of chromite are also observed in olivine. Some chromite grains contain sub-rounded melt inclusions.

Awaruite is rounded in morphology and has a size ranging from 20 μm to 1 mm in diameter. In the coarse lithology, larger grains (~1 mm) are present with plagioclase and olivine in the margin of orthopyroxene megacrysts. Smaller grains (~20 μm) occur mainly as ovals or spherules, scattering among the texture. Inclusions of awaruite are observed in orthopyroxene, olivine, and plagioclase. Moreover, there are composite inclusions of Ni-Fe-S minerals including awaruite and heazlewoodite with or without

pentlandite (Fig. 15c). Some of the composite inclusions show rounded morphology, but others show facetted outline against the host orthopyroxene (Fig. 15c), which indicates that it was a single crystalline phase when incorporated in the host. Some of the larger awaruite grains are associated with orthopyroxene grains and the reaction rims of Fe and Ni-rich olivine are observed along the grain boundaries with thickness of 5 μm (Fig. 15d).

Merrillite has a rounded morphology and grain size ranging from 20 to 100 μm in diameter. It is associated with plagioclase or pigeonite, and sometimes occurs as oval inclusions in plagioclase.

The representative EPMA data (in wt.%) for individual phases are summarized in Table 8. The major element compositions of individual minerals are generally homogeneous among thin sections. Orthopyroxene is mostly homogeneous with the ferrosilite component (Fs = 100 × Fe/(Mg+Fe+Ca)) ranging from 40 to 42, enstatite component (En = 100 × Mg/(Mg+Fe+Ca)) from 55 to 57, and wollastonite component (Wo = 100 × Ca/(Mg+Fe+Ca)) from 3 to 4. The average value of Fe/Mn is 1.4. However, some orthopyroxene megacrysts have a chemically distinctive core characterized by low Ca and high Mg contents. The EPMA line profile (Fig. 16) illustrates that the core has relatively low Ca and Ti contents and high Mg# (the center: $Fs_{35}En_{64}Wo_{0.8}$) with gradual increases of Ca, and Ti and decrease of Mg towards the margin of Ca and Mg plateau (Ca = 0.02 mol%, Mg# = 60.5), which is rimmed by orthopyroxene with the “normal” Mg# (the shaded area in Fig. 16b-d; Ca = 0.02–0.03 mol%, Mg# = 57–60). The orthopyroxene rim is further surrounded by pigeonite having

many exsolution of clinopyroxene.

Olivine has a slightly heterogeneous chemical composition ranging from 50 to 53 in fayalite content (Fa = 100 × Fe/(Mg+Fe)) with Fe/Mn = 1.1–2.1 and the average NiO = 0.9 wt.%. Vermicular olivine inclusions in the core regions of orthopyroxene megacrysts are richer in Fe (Fa_{54-55}) than "normal" olivine (Table 8).

Chromite has a Cr/(Cr+Al) ~0.94 and a notably high ferric content of ~2.2 wt.% of Fe_2O_3. Sub-rounded glass inclusions in chromite are rich in Fe, Ti and Mg as compared to glass inclusions in other phases (Table 8).

Ni-Fe metal is identified as awaruite with Ni contents ranging from 78 to 81 wt.% (Table 8). In Ni-Fe composite inclusions in orthopyroxene, awaruite has a chemical composition of $Fe_{20}Ni_{79}$, corresponding to relatively Ni-poor single awaruite grains, whereas heazlewoodite and pentlandite have compositions of $Fe_3Ni_{55}S_{42}$ and $Fe_{26}Ni_{24}S_{48}$, respectively.

Plagioclase is extremely Na-rich and classified as albite. It has slight heterogeneity with variation of albite content (Ab = 100 × Na/(Ca+Na+K)) from 91 to 93. It is also rich in orthoclase component (Or = 100 × K/(Ca+Na+K)) ranging from 4 to 6, while the anorthite content (An = 100 × Ca/(Ca+Na+K)) varies from 2 to 3.

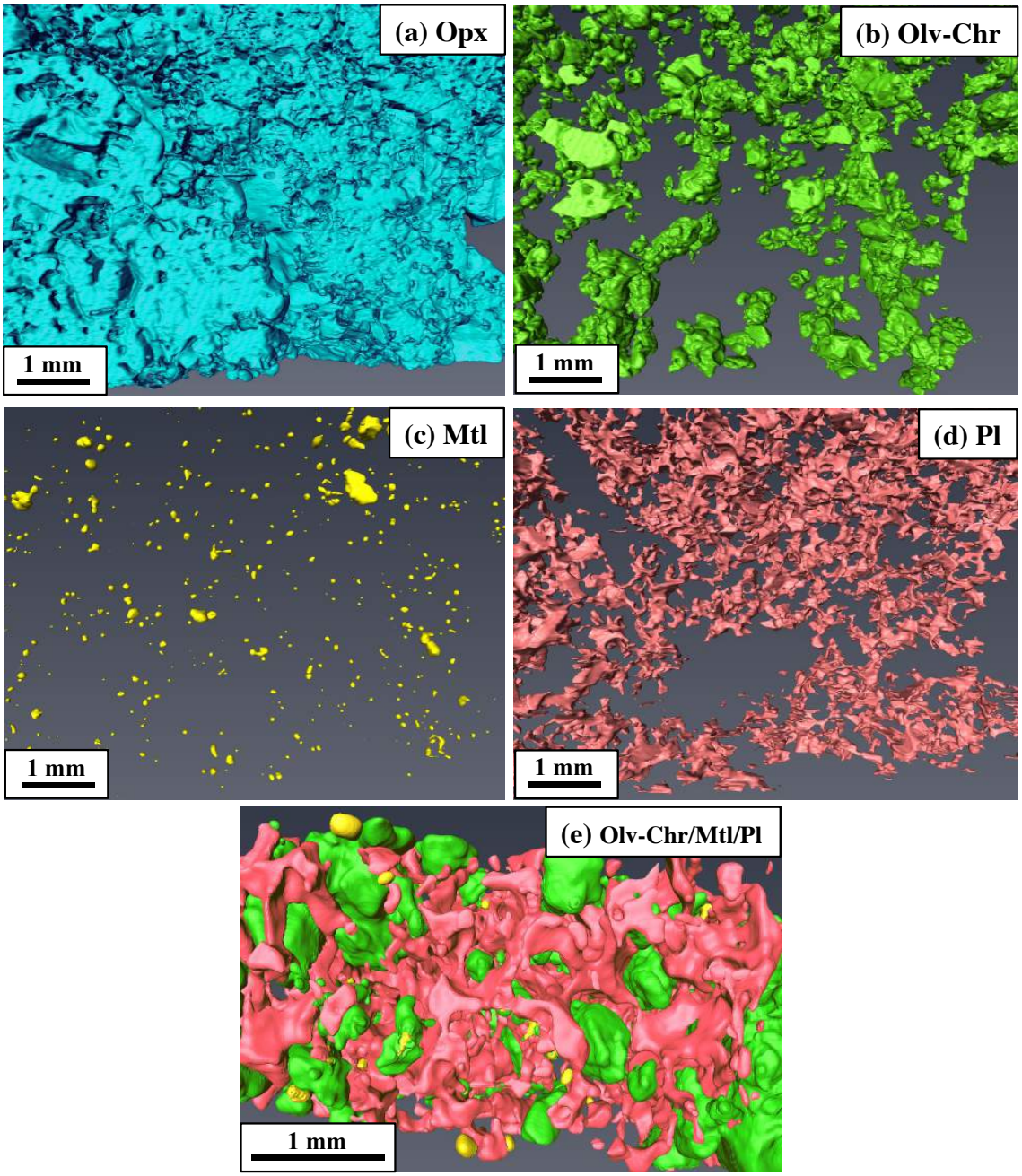

Fig. 9. 3D X-ray computed tomography (CT) images of (a) orthopyroxene, (b) olivine-chromite, (c) Fe-Ni metal, (d) plagioclase and (e) minerals other than orthopyroxene: olivine-chromite (green), metal (yellow), and plagioclase (pink).

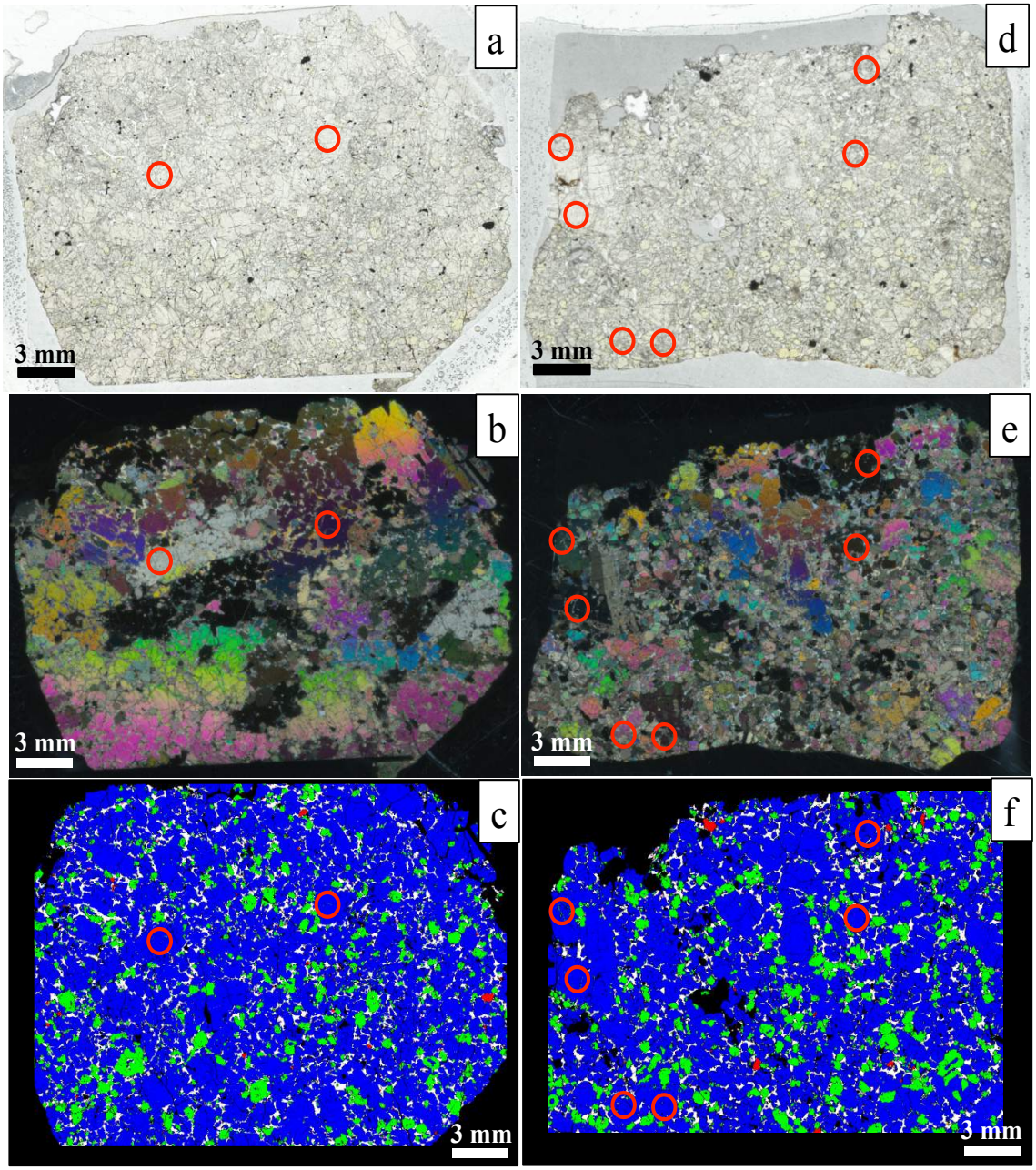

Fig. 10. Scanned images of "coarse-part" (TS-7) and "fine-part" (TS-6) are shown in the left- and right-hand columns, respectively. (a,d) open-nicols, (b,e) crossed-nicols and (c,f) chemical maps: orthopyroxene (blue), olivine (green), metal (red), and plagioclase (white). Vermicular olivine inclusions in the core regions of orthopyroxene megacrysts are highlighted by a red circle.

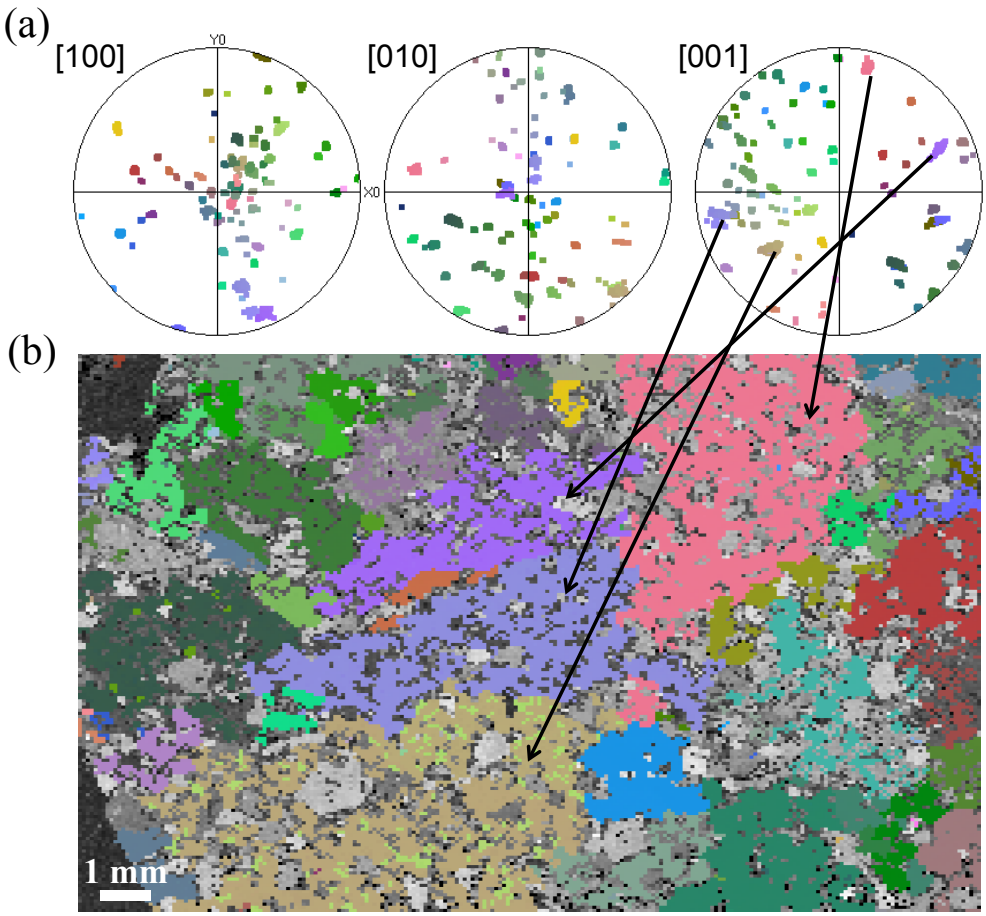

Fig. 11. (a) Pole figure diagrams for orthopyroxene {100} in thin section TS7. The maps were created with Euler color ascribed to orientations. (b) The inverse pole figure map of the analyzed area. The color of each phase corresponds to the color in obtained crystal orientation stereo nets. It shows that [001] of orthopyroxene grains correspond to their maximum length axes.

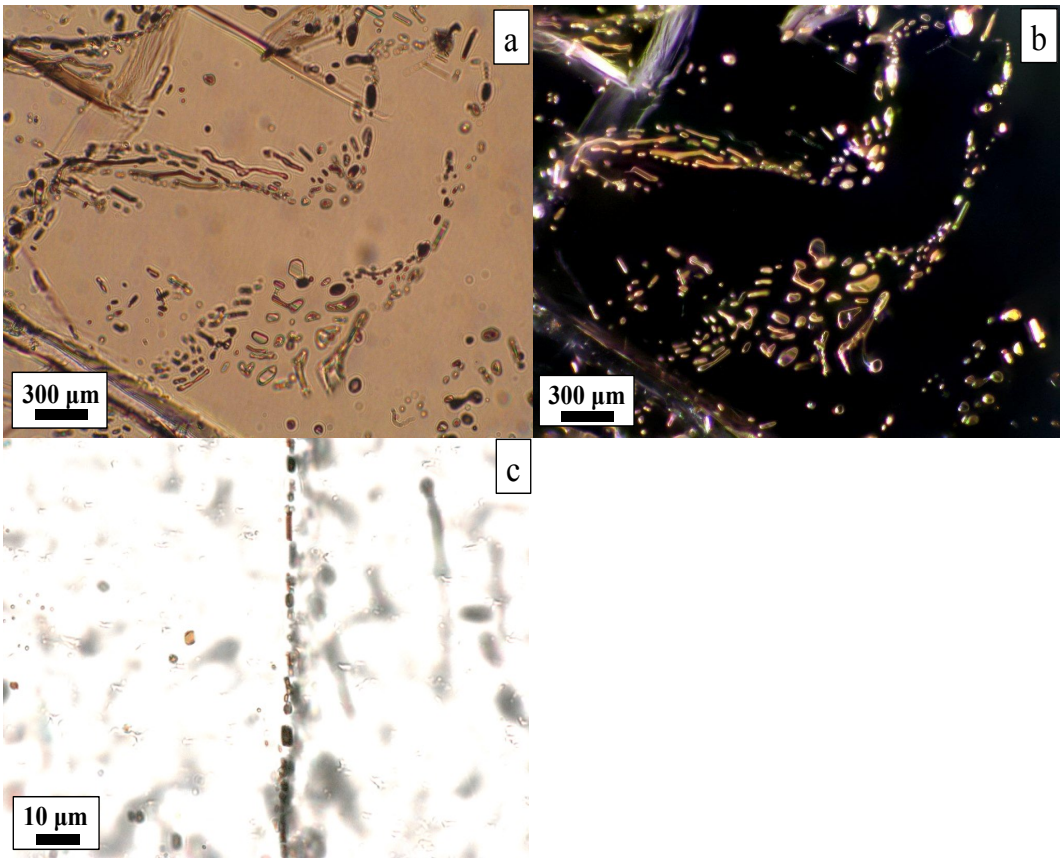

Fig. 12. Optical thin section images of curvilinear trains of micro-inclusions (< 2-30 µm) enclosed in some orthopyroxene megacrysts: (a,b) open- and crossed nicol views of rounded to irregularly-shaped clear to pinkish empty bubbles, and (c) open-nicol view of rectangular to oval brownish chromite inclusions.

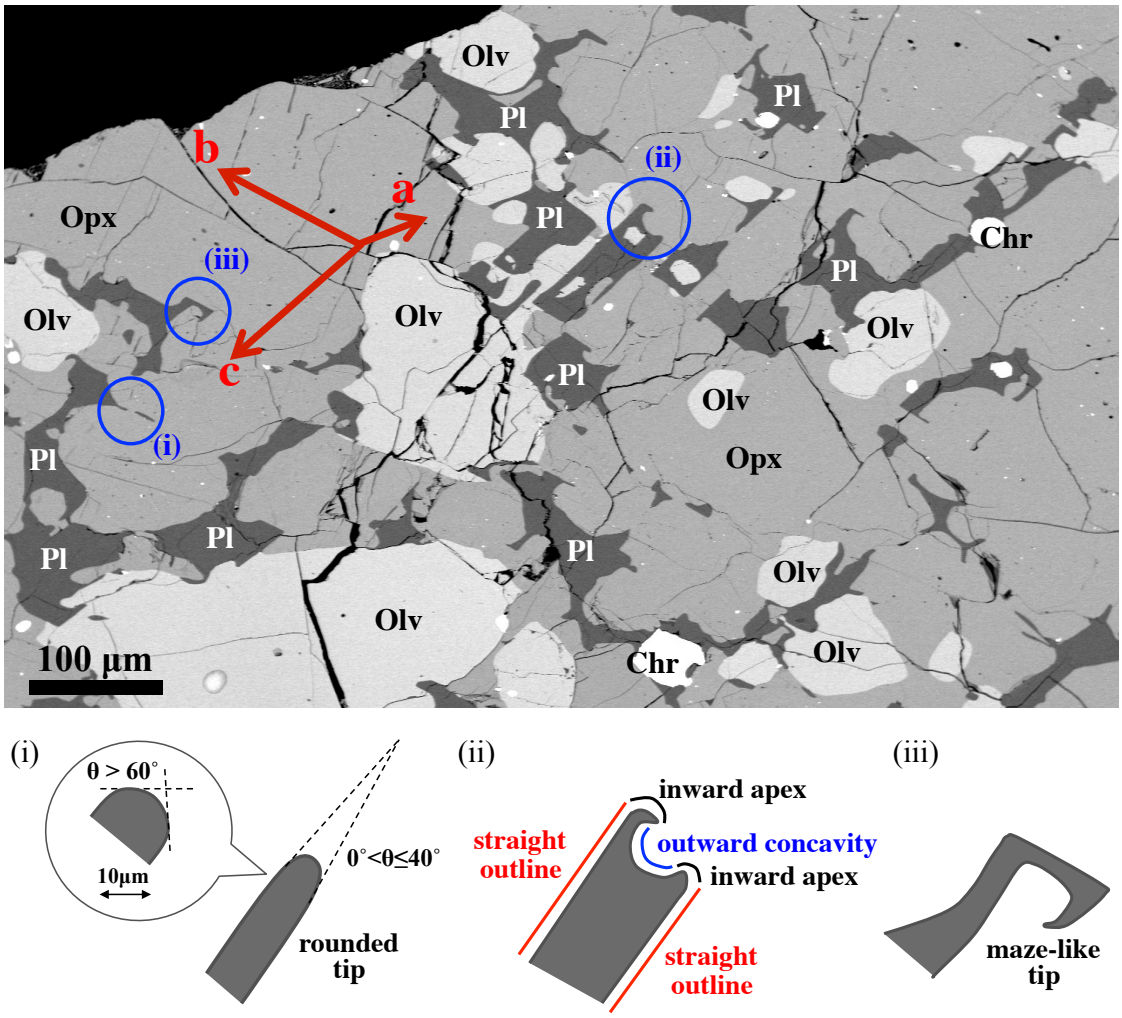

Fig. 13. Back-scattered electron image of thin section TS-7. The [100], [010] and [001] axes of orthopyroxene are compared with the shape of plagioclase, indicating that the shape of plagioclase is controlled by the facets of orthopyroxene megacrysts. Plagioclase typically shows three types of morphology; (i) cuspate shape with extremely low dihedral angles ($0 < \theta \leq 40^{\circ}$) on the scale greater than ~100 μm, and with much greater than 60° on the scale smaller than ~20 μm, (ii) rectangular morphology with both curvatures and straight interfaces with the host, and (iii) thin, delicate maze-like morphology with or with out branches extending into orthopyroxene megacrysts.

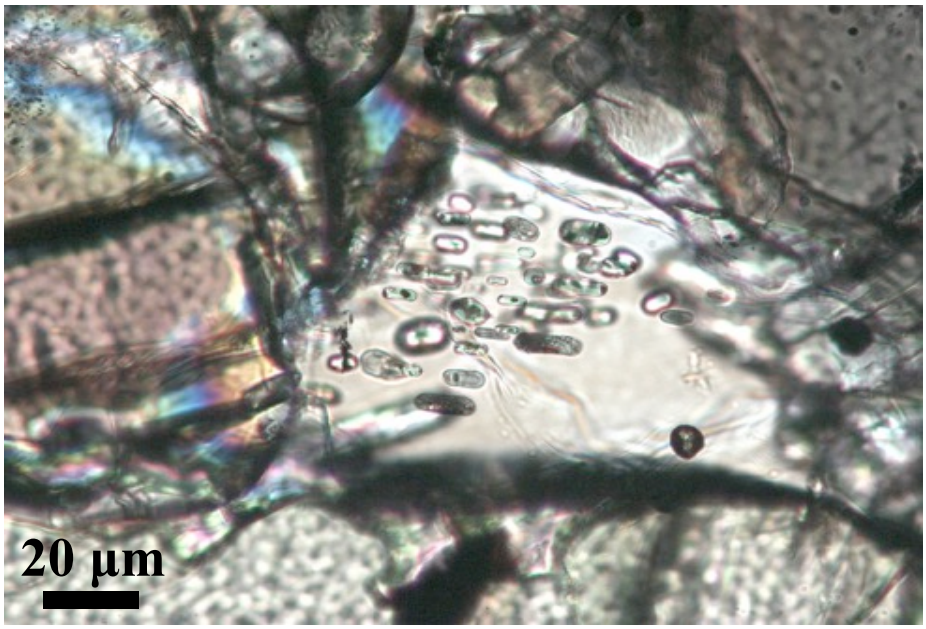

Fig. 14. Reflected-light, crossed-nicol view of oval inclusions in plagioclase of NWA 6704.

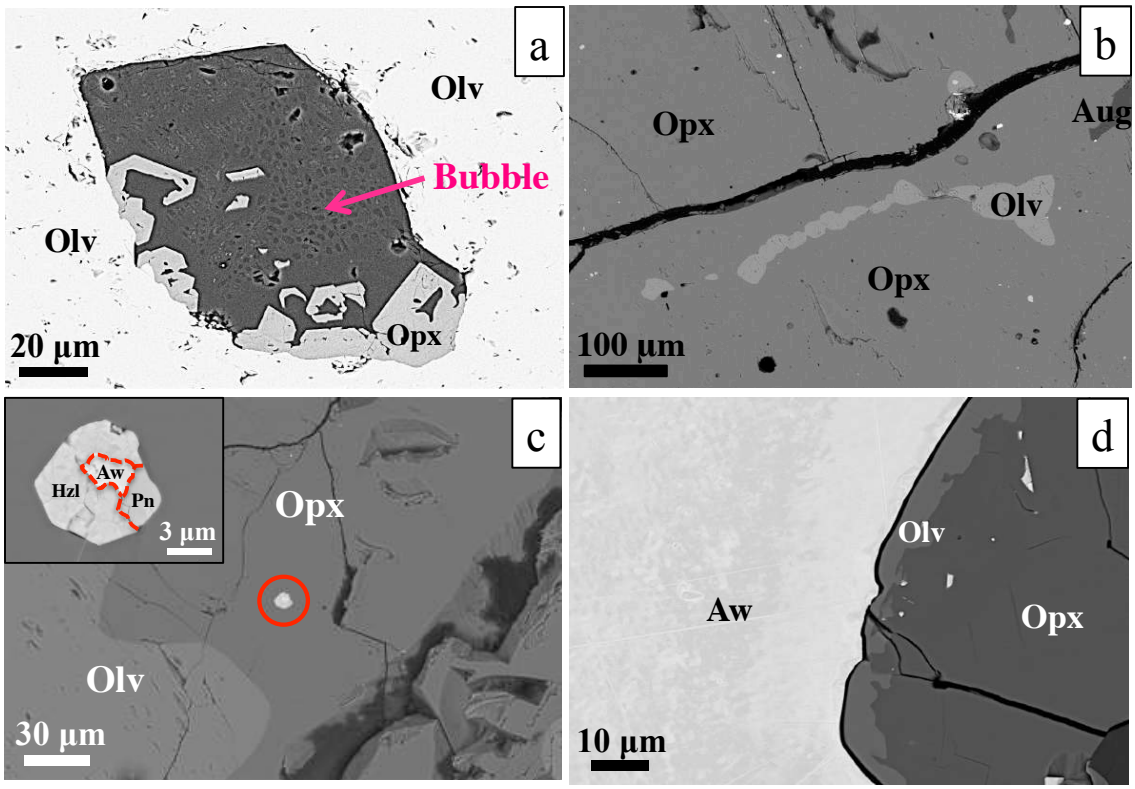

Fig. 15. Backscattered electron images showing (a) a melt inclusion in olivine, composed of skeletal orthopyroxene and glass with bubbles, (b) vermicular olivine inclusions within the orthopyroxene, (c) Fe-Ni-S minerals of awaruite ($Fe_{20}Ni_{80}$) + heazlewoodite ($Fe_2Ni_{56}S_{42}$) + pentlandite ($Fe_{27}Ni_{25}S_{48}$) enclosed by orthopyroxene, and (d) reaction rims of Fe, Ni-rich olivine along the grain boundary between large awaruite and orthopyroxene.

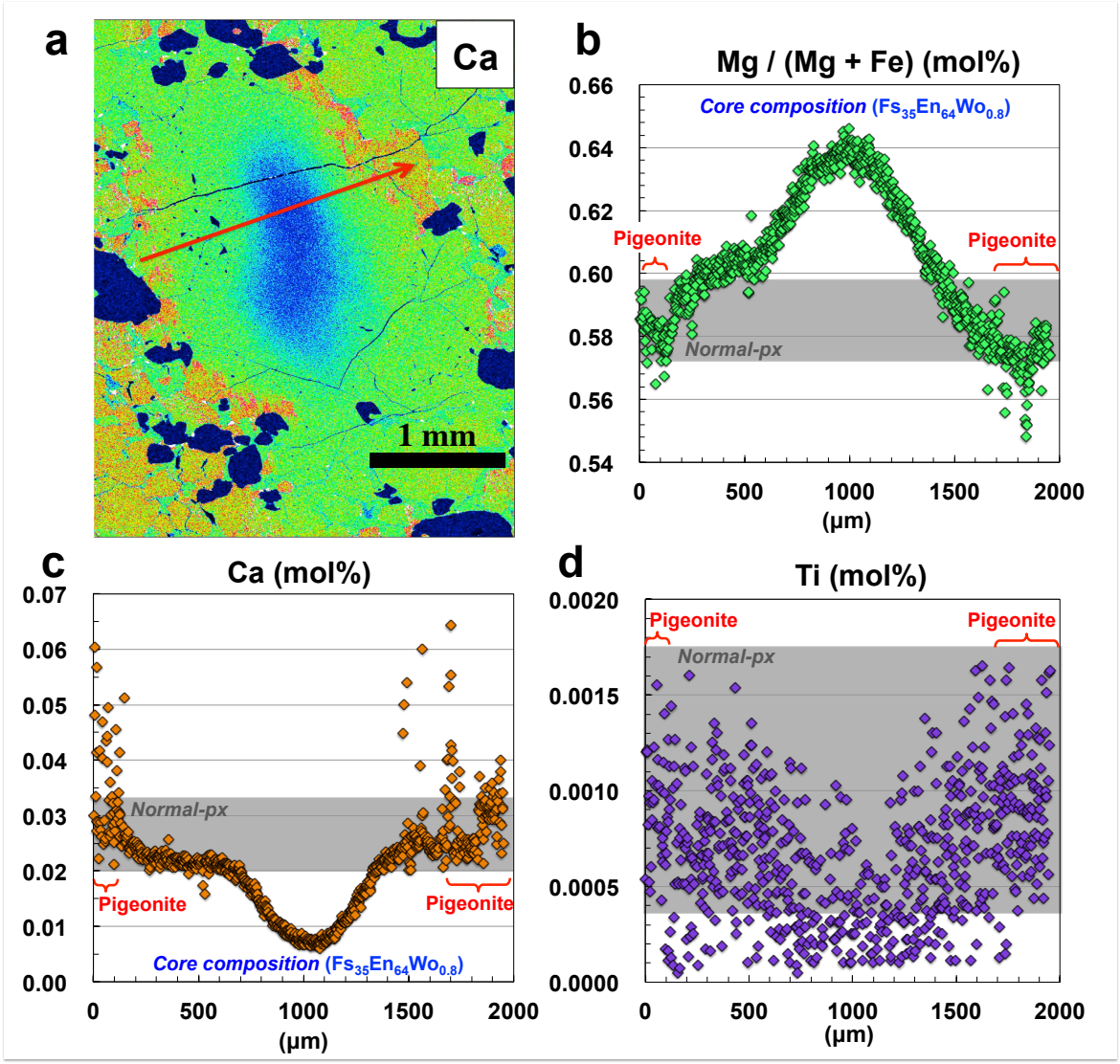

Fig. 16. A chemically zoned orthopyroxene megacryst: (a) Ca-mapping image and line profiles (2 μm step) of (b) Mg#, (c) Ca and (d) Ti. The shaded area (Ca = 0.02–0.03 mol%, Mg# = 57–60) shows the compositional range of "normal" Mg# orthopyroxene, randomly selected pyroxene among the thin section (n = 20). The orthopyroxene is further surrounded by pigeonite having exsolution lamellae of clinopyroxene.

Table 8: The representative EPMA data (in wt.%) for individual phases

	Orthopyroxene							Olivine				Vermicular olivine		
	Coarse-parts (N = 68)	2SD	Fine-parts (N = 41)	2SD	Relict opx in Fine-parts	NWA 6693 (N = 52)	NWA 6926 (N = 14)	Coarse-parts (N = 56)	2SD	Fine-parts (N = 24)	2SD	Coarse-parts (N = 12)	2SD	Fine-parts (N = 1)
SiO_2	52.56	1.16	52.66	1.16	53.42	51.98	52.44	34.28	0.83	34.46	0.30	33.67	0.38	34.00
TiO_2	0.08	0.08	0.07	0.10	0.06	0.08	0.05	0.02	0.05	0.01	0.02			0.01
Al_2O_3	0.11	0.08	0.14	0.11	0.21	0.12	0.09							
Cr_2O_3	0.30	0.19	0.29	0.12	0.34									
Total FeO	25.01	1.66	24.98	1.51	22.11	25.06	25.20	42.05	1.56	41.53	0.70	42.71	0.88	43.50
MnO	0.28	0.16	0.28	0.18	0.24	0.28	0.28	0.30	0.11	0.28	0.05	0.30	0.06	0.35
MgO	19.26	1.01	19.23	1.04	22.65	20.07	20.04	21.98	1.00	22.50	0.38	19.90	0.14	20.26
NiO	0.34	0.14	0.28	0.14	0.26			0.97	0.13	0.87	0.07	0.96	0.08	0.96
CaO	1.52	0.71	1.62	0.54	0.40	1.58	1.61	0.08	0.06	0.08	0.03	0.06	0.04	0.04
Na_2O	0.09	0.06	0.10	0.07	0.04	0.09	0.10					0.02	0.02	0.03
K_2O							0.02							
Total	99.54		99.62		99.73	99.26	99.83	99.78		99.81		97.62		99.15
En	56.02		55.88		64.1	56.9	56.7							
Fs	40.80		40.73		35.1	39.9	40.0							
Wo	3.17		3.38		0.81	3.21	3.27							
mg	57.79		57.94		64.6	58.8	58.6	48.19		49.12		45.4		45.4

	Chromite					Plagioclase						Merrillite		
	Coarse-parts (N = 38)	2SD	Fine-parts (N = 19)	2SD	NWA 6693	Coarse-parts (N = 31)	2SD	Fine-parts (N = 11)	2SD	NWA 6693	NWA 6926	Fine-parts (N = 17)	2SD	NWA 6693 (End 1)
SiO_2					0.03	66.80	1.80	67.20	0.81	66.60	67.60	0.11	0.04	0.08
TiO_2	2.54	0.73	2.93	0.97	2.73					0.04	0.05			0.01
Al_2O_3	2.88	1.59	2.47	0.82	2.84	19.38	0.61	20.07	0.38	20.09	18.94	0.02	0.02	0.01
Cr_2O_3	58.32	1.40	57.99	2.15	57.89					0.02	0.04			0.01
Total Fe_2O_3	2.21	0.96	2.25	1.00	2.10									
Total FeO	31.89	1.33	32.17	1.02	31.97	0.26	0.21	0.25	0.19	0.27	0.39	1.33	0.18	1.58
MnO	0.26	0.13	0.27	0.13	0.34					0.01	0.02	0.03	0.02	0.01
MgO	1.54	0.42	1.54	0.36	1.73					0.01	0.01	3.16	0.11	3.06
NiO	0.27	0.11	0.26	0.08										
CaO					0.02	0.65	0.18	1.23	0.22	0.61	0.44	47.02	0.25	45.95
Na_2O					0.02	10.52	0.72	10.91	0.71	10.69	11.14	2.50	0.13	2.64
K_2O						0.67	0.09	0.42	0.11	1.01	0.89	0.03	0.02	
P_2O_5												46.70	0.34	45.90
Total	99.67		99.65		97.57	98.28		100.08		99.35	99.52	100.90		99.25
Cr/(Cr+Al)	0.93		0.94		0.93	An 3.17		2.33		2.90	2.02			
						Ab 92.9		92.0		91.4	93.1			
						Or 3.90		5.72		5.66	4.91			

	Glass inclusion					Awaruite						Pentlandite	Heazlewoodite
	in olivine	in olivine K-rich	in chromite	NWA 6693 (in chromite)		Coarse-parts (N = 17)	2SD	Fine-parts (N = 18)	2SD	NWA 6693		Coarse-parts (N = 1)	Coarse-parts (N = 1)
SiO_2	82.53	78.05	60.31	60.31	Si					0.02	Si	0.07	0.27
TiO_2	0.08	0.18	1.01	1.01	S					0.02	S	47.49	41.9
Al_2O_3	12.79	13.42	12.20	12.20	Fe	19.49	1.24	20.21	1.83	18.61	Fe	26.4	3.05
Cr_2O_3			10.17	10.17	Ni	79.72	1.29	78.97	1.78	80.74	Ni	24.4	54.7
Total FeO	0.76	1.04	8.25	8.25	Cr						Cr	0.02	
MgO	0.03	0.16	0.46	0.46	Co	0.71	0.07	0.74	0.12	0.74	Co	1.62	0.03
NiO	0.03	0.03	0.04	0.04									
CaO	0.02	0.02	0.06	0.06									
Na_2O	3.35	0.81	7.85	7.85									
K_2O	1.06	7.66	0.12	0.12									
Total	100.65	101.37	100.47	100.47	Total	99.92		99.92		100.13	Total	100.00	99.95
An	0.33	0.20	0.42	0.42									
Ab	82.4	13.8	98.6	98.6									
Or	17.2	86.0	1.01	1.01									
Total cations (O = 8)	4.42	4.56	4.99	4.99									

3. 3. 2. Geothermometry and geobarometry

The temperatures estimated by applying the two-pyroxene geothermometer of Lindsley and Andersen (1983) to 18 pairs of orthopyroxene and augite inverted from pigeonite range from 900 to 1200 ˚C, with an average of 1050 ˚C. Olivine-spinel Fe-Mg exchange geothermometry of Fabriés et al. (1979) for neighboring spinel and olivine yields temperatures ranging from 850 to 970 ˚C with an average of 900 ˚C. The cooling rate of NWA 6704 can be constrained from the relationship between the calculated temperature of the average olivine composition and chromite core (T*) and sizes (f = ~35–260 μm in diameter) of respective chromite grains by applying geospeedometry established by Ozawa (1984). The T*– f diagram (Fig. 17) indicates a cooling rate of 10^{-4}–10^{-2} ˚C/hr. Considering, however, that NWA 6704 is composed predominantly of orthopyroxene in which Mg-Fe diffusion is slower than in olivine, the actual cooling rate was slower than this estimate.

The coexistence of olivine, orthopyroxene, and spinel allows us to constrain the oxygen fugacity (fO_2) on the basis of the olivine-spinel oxygen geobarometry of Ballhaus et al. (1991). Using the temperature estimated from the olivine-spinel Fe-Mg exchange geothermometer for each chromite grain, the fO_2 is constrained to be 2.6 log units below the fayalite-magnetite-quartz buffer (FMQ −2.6). The result is consistent with the presence of Ni-rich metal (78–81 wt.% Ni) and ferric content in chromite (2.23 wt.% Fe_2O_3).

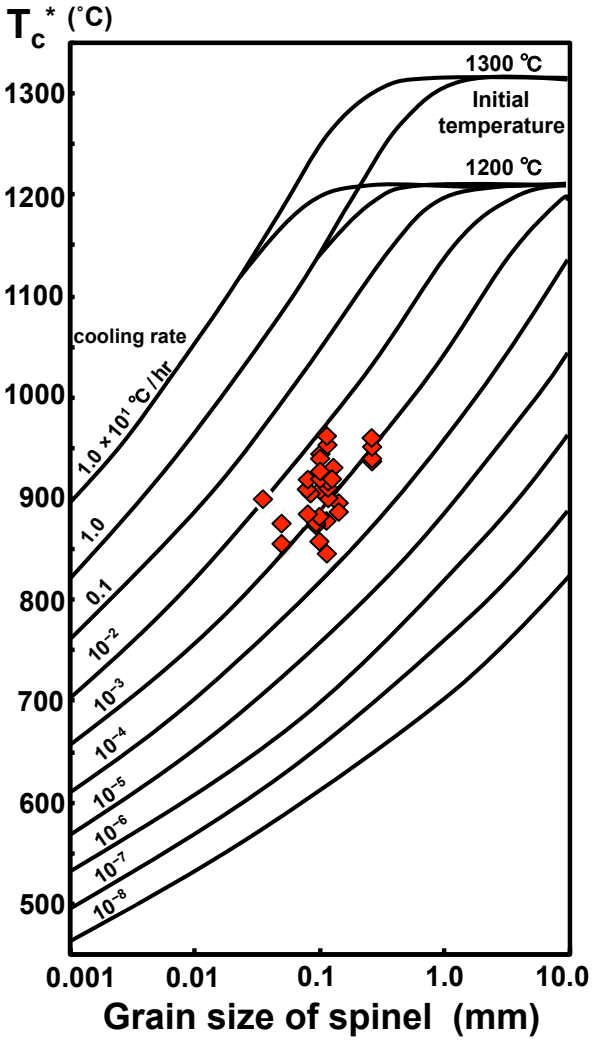

Fig. 17. Plot of estimated temperature (T^*_c) vs. grain size (φ_{sp}) for chromite grains of NWA 6704. The T^*_c–φ_{sp} relationship can be used to constrain the cooling rate based on geospeedometry established by Ozawa (1984). The data for NWA 6704 chromite grains are represented by red points. The T^*_c were estimated using the olivine-spinel Fe-Mg exchange geothermometer of Fabriès et al. (1979) for each chromite grain with the neighboring olivine.

3. 3. 3. Major and trace elements

The measured whole rock and mineral compositions of NWA 6704 measured by solution-based ICP-MS are summarized in Table 9. The bulk major element compositions estimated using the modal mineral abundances obtained from the phase maps (Table 7) and mineral chemical compositions (Table 8) are also listed in the table. The XRF major element analysis of fragment #5 yielded substantially 6% lower SiO_2 and 4% higher FeO contents than the estimates on fragment #4 using the modal mineral abundance and mineral compositions, indicating chemical heterogeneity among the fragments. The Si/Mg ratio in the both fragments is distinctly higher than that in CI chondrites (Si/Mg ~1.9–2.2 × CI), whereas relative abundances of Na, Ni, Fe, Mn, K and Ca to Mg are similar to or slightly lower than those in CI chondrites (~0.8–1.0 × CI). In Fig. 18, the whole rock major and trace element abundances of NWA 6704, normalized to CI chondrite abundances (Palme and O'Neill, 2014), are plotted against the order of decreasing incompatibility to orthopyroxene (Kennedy et al., 1993; Bédard et al., 2007; Laubier et al., 2014) (Fig. 18a) and the 50% condensation temperature for a solar composition gas at 10^{-4} bar (Tc, Lodders, 2003) (Fig. 18b). The plots show that, relative to CI chondrite, NWA 6704 is depleted in elements having Tc of <900 K irrespective of lithophile, siderophile, or chalcophile (Fig. 18b), whereas there is no systematic change in the relative elemental abundances with the incompatibility (Fig. 18a). Among the two whole rock fractions analyzed for trace elements, fragment #3 has markedly higher abundances of Sr and Ba than fragment #6. Considering that these

elements are sensitive indicators of terrestrial weathering (Barrat et al., 2003), the data suggest that fragment #3 is more affected by terrestrial weathering. Both of the two fragments show moderate depletion in heavy REE abundances as compared to CI chondrite (0.5 × CI) with only slightly light REE depleted to enriched patterns ($[La/Yb]_N$ = 0.63–2.1, [Eu/Eu*] = 0.84–1.09) (Fig. 19). The present data for NWA 6704 and NWA 6693 are generally consistent with those obtained for NWA 6693 by Warren et al. (2013), except for Cr, some REE, Ni, V, and Co. The differences may be partly due to the uneven distribution of minor phases such as Ni-Fe-metal, phosphate, and chromite between samples.

Table 9a: Major element abundances determined in NWA 6704 by x-ray fluorescence

		NWA 6704 **XRF data**	**NWA 6704** **estimated from EPMA**	**NWA 6693** **Warren et al. (2013)**
SiO_2	wt%	45.75	52.02	50.52
TiO_2	wt%	0.07	0.07	0.06
Al_2O_3	wt%	2.18	1.75	1.94
Cr_2O_3	wt%	1.00	0.34	0.44
Total FeO	wt%	28.94	24.78	24.65
MnO	wt%	0.27	0.26	0.25
MgO	wt%	17.10	18.29	18.46
CaO	wt%	1.46	1.27	1.47
Na_2O	wt%	1.00	0.50	1.02
K_2O	wt%	0.08	–	0.04
P_2O_5	wt%	0.22	0.02	0.09

[a]CI values from Palme et al. (2014).

Table 9b: Major and trace element abundances determined in NWA 6704 and NWA 6693 by ICPMS

Sample		NWA 6704-#3-a	NWA 6704-#3-b	NWA 6704-#3-c	NWA6704-#3-ave	NWA 6704-#6	NWA 6704-#6 Plagioclase	NWA 6704-#6 Pyroxene	[b]NWA6704-J.B.	NWA 6693
mass		50.2 mg	50.1 mg	51.6 mg		32.91 mg			125 mg	39.48 mg
Na	wt%					0.79	8.44	0.22	0.65	0.80
Mg	wt%					8.89	0.41	11.87	11.28	7.81
Al	wt%					0.88	11.78	0.19	0.97	0.90
Ca	wt%					1.09	1.20	1.31	0.99	1.19
Cr	wt%					0.22	0.01	0.20	0.16	0.37
Fe	wt%					20.54	0.73	20.57	20.85	18.26
Ni	wt%					1.34			0.91	0.58
Li	µg/g	2.091	2.194	1.883	2.056	2.709	0.323	2.607	3.15	2.574
Be	µg/g	0.025	0.040	0.017	0.027	0.008	0.112	0.025	0.034	0.018
Sc	µg/g	3.256	3.366	2.811	3.144	3.857			4.16	4.052
Ti	µg/g					363.68	221.2	466.2	351.00	412.69
Mn	µg/g					1900.0	71.4	2085.6	1814	1765.4
V	µg/g					64.80	1.8	46.2	60.3	74.75
Co	µg/g					554.13	15.5	365.2	627	433.84
Cu	µg/g	11.32	13.10	13.38	12.60	53.36	2.04	2.84	96	18.28
Rb	µg/g	0.377	0.393	0.328	0.366	0.164	3.547	0.268	0.95	0.529
Sr	µg/g	14.39	14.98	12.62	13.99	4.165	185.9	1.185	4.38	6.139
Y	µg/g	0.700	0.734	0.624	0.686	0.648	0.365	0.645	0.79	0.799
Zr	µg/g	2.620	2.762	2.317	2.566	0.432	0.900	2.381	2.52	3.390
Nb	µg/g	0.259	0.274	0.222	0.251	0.277	0.046	0.455	0.38	0.273
Mo	µg/g					4.374				3.559
Sn	µg/g					0.073				0.098
Te	µg/g					0.002				0.008

Table 9b (*Continued*)

Sample		NWA 6704-#3-a	NWA 6704-#3-b	NWA 6704-#3-c	NWA6704-#3-ave	NWA 6704-#6	NWA 6704-#6 Plagioclase	NWA 6704-#6 Pyroxene	[b]NWA6704-J.B.	NWA 6693
mass		50.2 mg	50.1 mg	51.6 mg		32.91 mg			125 mg	39.48 mg
Cs	µg/g	0.015	0.016	0.013	0.014	0.008			0.020	0.008
Ba	µg/g	5.402	5.664	4.794	5.287	1.575			5.21	5.765
La	µg/g	0.216	0.226	0.193	0.212	0.071	0.275	0.018	0.130	0.171
Ce	µg/g	0.593	0.620	0.531	0.581	0.211	0.668	0.067	0.336	0.449
Pr	µg/g	0.088	0.093	0.080	0.087	0.032	0.091	0.010	0.0498	0.063
Nd	µg/g	0.421	0.442	0.377	0.414	0.164	0.436	0.063	0.240	0.301
Sm	µg/g	0.130	0.136	0.117	0.128	0.065	0.119	0.039	0.0880	0.103
Eu	µg/g	0.045	0.047	0.041	0.044	0.018	0.435	0.011	0.0267	0.031
Gd	µg/g	0.122	0.128	0.108	0.119	0.065	0.101	0.051	0.0994	0.100
Tb	µg/g	0.021	0.023	0.019	0.021	0.015	0.015	0.013	0.0201	0.021
Dy	µg/g	0.140	0.148	0.126	0.138	0.119	0.083	0.111	0.138	0.150
Ho	µg/g	0.028	0.029	0.025	0.028	0.026	0.014	0.025	0.0299	0.032
Er	µg/g	0.079	0.083	0.071	0.077	0.074	0.032	0.076	0.0869	0.090
Tm	µg/g	0.012	0.012	0.010	0.011	0.013	0.005	0.015		0.015
Yb	µg/g	0.076	0.079	0.069	0.075	0.087	0.024	0.101	0.0917	0.098
Lu	µg/g	0.010	0.011	0.009	0.010	0.012	0.003	0.015	0.0119	0.013
Hf	µg/g	0.072	0.076	0.066	0.071	0.023	0.063	0.055	0.0573	0.065
Ta	µg/g	0.021	0.017	0.013	0.017	0.011	0.005	0.013	0.0149	0.012
W	µg/g					0.598			0.18	0.164
Tl	µg/g					0.001	0.001	0.000		0.001
Pb	µg/g	0.034	0.031	0.033	0.033	0.152	0.056	0.033	0.013	0.041
Th	µg/g	0.029	0.029	0.026	0.028	0.011	0.024	0.016	0.0193	0.018
U	µg/g	0.017	0.017	0.015	0.016	0.012	0.010	0.008	0.0165	0.014

[a]CI values from Palme et al. (2014).

[b]Data provided by Jean-Alix Barrat.

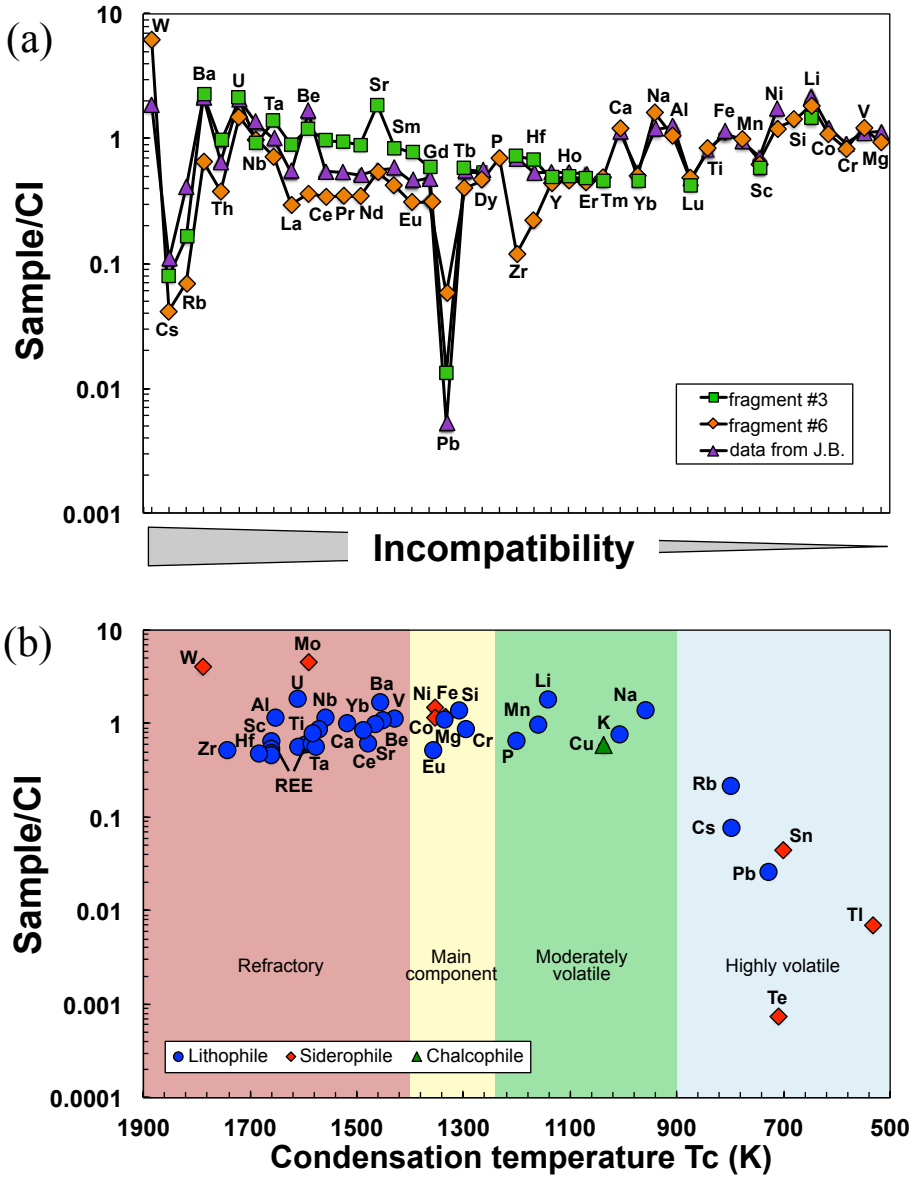

Fig. 18. CI-normalized (Palme and O'Neill, 2014) major and trace element abundances of NWA 6704. (a) The data for whole rock fragments #3 and #6 are plotted against the order of decreasing incompatibility to orthopyroxene (Kennedy et al., 1993; Bédard et al., 2007; Laubier et al., 2014). The whole rock data obtained by Jean-Alix Barrat (J.B.) are also shown for comparison. (b) The averaged values of the data shown in (a) are plotted against the 50% condensation temperature for a solar composition gas at 10^{-4} bar (Tc, Lodders, 2003).

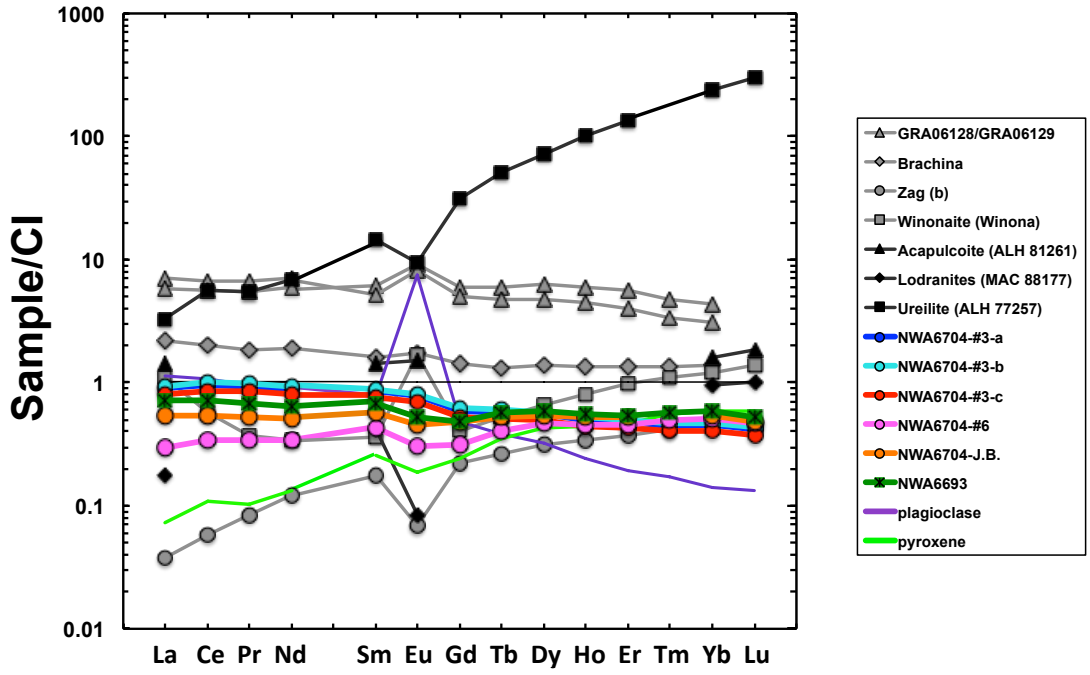

Fig. 19. Comparison of CI-normalized (Palme and O'Neill, 2014) whole rock rare earth element abundances between NWA 6704 and various primitive achondrites (GRA 06128/9, Brachina and Zag from Day et al., 2012; Winona from Floss, 2008; ALH 81261 and MAC 88177 from Mittlefehldt et al., 1996; ALH 77257 from Spitz and Boynton, 1991; NWA 6693 from Warren et al., 2013). NWA6704-J.B. represents the data provided by Jean-Alix Barrat (J.B.). Also shown are rare earth element patterns of plagioclase and pyroxene separates of NWA 6704.

3. 3. 4. Highly siderophile elements and Re–Os isotopes

The HSE abundances and ^{187}Re–^{187}Os systematics for NWA 6704 are presented in Table 10. Highly siderophile element abundances, normalized to CI chondrite abundances (Orgueil; Horan et al., 2003) are shown in Fig. 20. The milligram-sized bulk fragments have broadly chondritic HSE abundances, ranging from ~0.2 × to ~5 × CI abundances of Ir. The metal fraction has much higher HSE abundances, with ~48 × CI Ir. By contrast, the silicate fraction has much lower HSE abundances than bulk fractions, with ~0.05 × CI Ir. The relative abundances of all fractions are only slightly fractionated from CI chondrite relative abundances. CI-normalized Re/Ir, Os/Ir, Ru/Ir, Pt/Ir, and Pd/Ir range from 0.7–1.7, 0.7–1.4, 0.8–1.7, 1.0–1.4, and 0.7–2.2, respectively. To estimate NWA 6704 HSE abundances at the whole-rock scale, the HSE abundances of the milligram-sized bulk fragments were averaged, weighted by mass (Fig. 20). Although the HSE abundances of a calculated whole rock composition are similar to bulk chondrites, on a finer scale there are HSE fractionations and large variations in the absolute HSE abundances among milligram-sized bulk fragments.

The ^{187}Re–^{187}Os systematics are shown in Fig. 21. The milligram-sized bulk fragments have $^{187}Os/^{188}Os$ ranging from 0.121 to 0.147, while those ratios in metal and silicate fractions are within the range. The $^{187}Os/^{188}Os$ in the bulk and metal fractions are correlated well with Re/Os but not with 1/Os (Fig. 21a and b), indicating that the regression line in Fig. 21a represents not a mixing line but an isochron. The isochron regression using ISOPLOT (Ludwig, 2001) defines an age of 4576 ± 250 Ma, indicating

early Solar System closure of the isotope system. By contrast, the silicate fraction plots below this isochron (Fig. 21a). The ^{187}Re–^{187}Os systematics of these samples can be expressed in Δ_{Os} units (where Δ_{Os} is the deviation in parts per 10,000, from a primordial 4568 Ma reference isochron, using parameters from Becker et al. (2001) and Archer et al. (2014) ($\Delta_{Os} = 10^4 \times [^{187}Os/^{188}Os_{Sample} - [0.09517 + 0.07908 \times {}^{187}Re/^{188}Os_{Sample}]]$). The Δ_{Os} of bulk samples and metal range from +0.8 to +6.8, whereas the silicate sample has a Δ_{Os} value of –24 ± 10 (Table 10; Fig. 21c). The larger error bars for the silicate are the result of low Re and Os abundances, and consequently, larger blank corrections.

Table 10:

Highly siderophile element abundances (ppb) and ^{187}Re–^{187}Os systematics of NWA 6704 metal, silicate, and bulk fractions.

Sample	Weight (mg)	Re	Os	Ir	Ru	Pt	Pd
NWA 6704							
Bulk A	33.9	10.69	89.22	93.64	188.5	243.2	137.4
Bulk B	20.3	11.69	85.78	85.49	177.3	231.3	142.6
Bulk C	5.14	215.7	3242	2252	2668	4200	4064
Bulk D	6.34	70.99	694.2	486.6	725.3	1135	1188
Metal	6.02	3034	29820	22000	32340	49270	58560
Silicate	9.96	1.474	15.42	23.47	58.37	48.38	20.36
Sample	**$^{187}Re/^{188}Os$**	**2σ[b]**	**$^{187}Os/^{188}Os$**	**2σ[b]**	**Δ_{Os}[a]**	**2σ[b]**	
NWA 6704							
Bulk A	0.5782	0.0008	0.14133	0.00008	4.3	0.7	
Bulk B	0.658	0.0016	0.14738	0.00012	1.8	1.2	
Bulk C	0.3203	0.0026	0.12119	0.00076	6.8	2.2	
Bulk D	0.4932	0.0032	0.13439	0.00025	2.1	2.5	
Metal	0.4906	0.0005	0.13405	0.00018	0.85	0.4	
Silicate	0.461	0.013	0.12923	0.00086	-24	10	

[a] Δ_{Os} is the deviation in parts per 10,000, from a primordial 4568 Ma reference isochron.

[b] Uncertainties of $^{187}Re/^{188}Os$, $^{187}Os/^{188}Os$, and Δ_{Os} are 2σ.

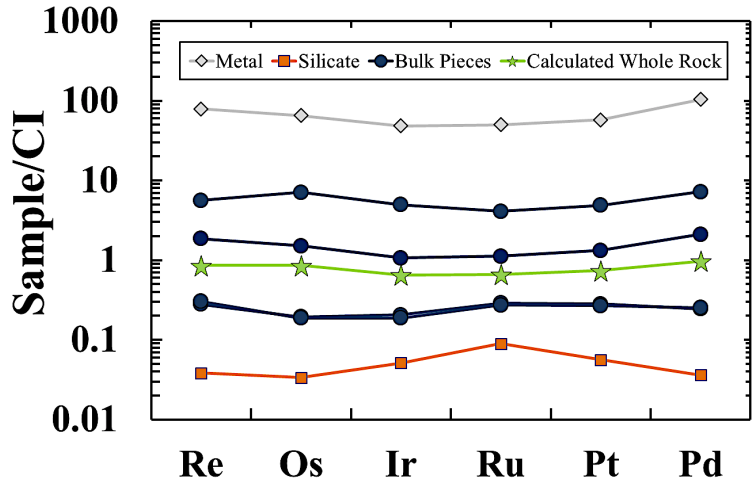

Fig. 20. CI-normalized (Horan et al., 2003) highly siderophile element abundances of NWA 6704 bulk fragments, metal, silicate, and calculated whole rock. Uncertainties are smaller than symbols.

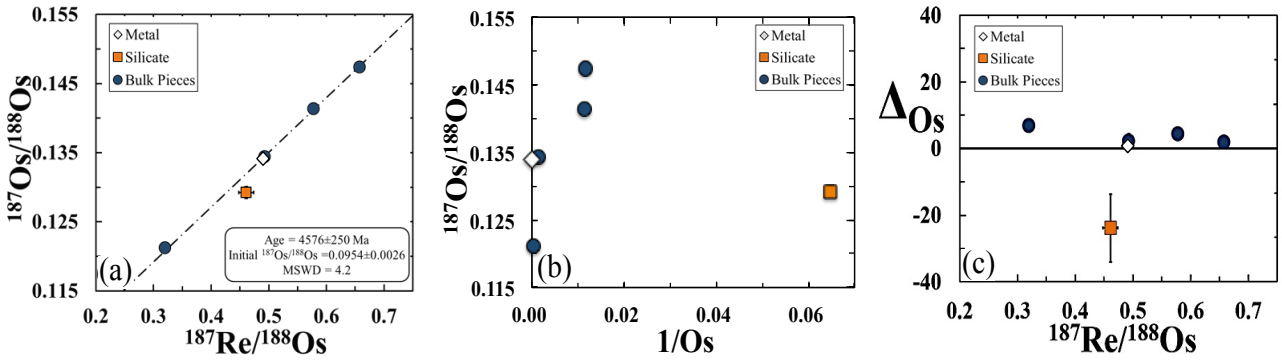

Fig. 21. ^{187}Re–^{187}Os systematics of NWA 6704 bulk, metal, and silicate fractions. Uncertainties are smaller than symbols unless shown. (a) Re–Os isochron calculated using ISOPLOT (Ludwig, 2001) for NWA 6704 metal and bulk fractions. (b) Plot of ^{187}Os/^{188}Os vs. 1/Os. (c) The absolute deviation in parts per 10,000, from a primordial 4568 Ma reference isochron (Δ_{Os}) plotted against ^{187}Re/^{188}Os.

3. 3. 5. Oxygen–Cr–Ti isotopes

The results of O isotope analyses of NWA 6704 are summarized in Table 11, together with those of a different fragment of NWA 6704 (Irving et al., 2011) and paired NWA 6693 (Warren et al., 2013). The five fractions analyzed in this study yielded slightly variable $\delta^{18}O$ and $\delta^{17}O$ values but identical $\Delta^{17}O$ values within analytical uncertainty. Moreover, the $\delta^{18}O$ and $\delta^{17}O$ values are clearly distinct from the previously reported values for NWA 6704 (Irving et al., 2011), while the $\Delta^{17}O$ values are consistent with those of Irving et al. (2011). The variations in the $\delta^{18}O$ and $\delta^{17}O$ values can be attributed to the difference in mineral abundance among the analyzed fractions. Our results yield an average $\Delta^{17}O$ value of -1.052 ± 0.002 (1 SD), which is similar to the $\Delta^{17}O$ value of -1.08 obtained from paired NWA 6693 (Warren et al., 2013).

The Cr and Ti isotopes analyses of NWA 6704 are summarized in Table 12. Consistent with previous studies (Sanborn et al. 2014), the NWA 6704 yielded markedly positive values of $\varepsilon^{54}Cr$ and $\varepsilon^{50}Ti$. The isotope compositions are within the range of carbonaceous chondrites (Fig. 22), in striking contrast to those of other primitive achondrites, such as acapulcoite and lordanite, which are similar to non-carbonaceous meteorites (Larsen et al. 2011, Zhang et al. 2012, Göpel et al. 2015, Goodrich et al. 2017). Figure 23 summarizes the $\varepsilon^{46}Ti$ and $\varepsilon^{50}Ti$ values of the individual sample fractions analyzed in this study. The plot shows a linear correlation between the two values with a regression line of $\varepsilon^{50}Ti = (4.94 \pm 0.63) \times \varepsilon^{46}Ti + (0.44 \pm 0.25)$, which

is similar to the one proposed by (Trinquier et al. 2009) ($\varepsilon^{50}Ti = (5.48 \pm 0.27) \times \varepsilon^{46}Ti - (0.04 \pm 0.20)$).

Table 11:

The oxygen isotope composition of NWA 6704 bulk meteorite, compared with those of paired meteorites

Sample	$\delta^{18}O$	$\delta^{17}O$	$\delta^{17}O^*$	$\Delta^{17}O^b$
NWA 6704 fraction-1	4.557 ± 0.004[a]	1.307 ± 0.007	1.346	−1.051 ± 0.008
NWA 6704 fraction-2	4.637 ± 0.002	1.348 ± 0.011	1.387	−1.052 ± 0.010
NWA 6704 fraction-3	4.601 ± 0.005	1.327 ± 0.010	1.366	−1.054 ± 0.009
NWA 6704 fraction-4	4.460 ± 0.004	1.257 ± 0.007	1.296	−1.050 ± 0.007
NWA 6704 fraction-5	4.501 ± 0.004	1.275 ± 0.006	1.314	−1.053 ± 0.007
Average ± 2SD	4.551 ± 0.144	1.303 ± 0.074	1.342	−1.052 ± 0.004
NWA 6704 (N = 2)[c]	3.77		0.95	−1.03
NWA 6693 (N = 2)[d]	4.32		1.19	−1.08

[a]Uncertainties in each fraction are internal precisions and expressed as 1SE.

[b]$\Delta^{17}O = 10^3 \times [\ln(\delta^{17}O^* \times 10^{-3} + 1) - 0.527 \times \ln(\delta^{18}O \times 10^{-3} + 1)]$, where $\delta^{17}O^* = \delta^{17}O + 0.039$ (Pack et al., 2016).

[c]From Irving et al. (2011). Average and external precision of the standard during analysis was $\delta^{18}O = 5.976 \pm 0.180$, $\delta^{17}O^* = 3.140 \pm 0.144$ and $\Delta^{17}O = -0.005 \pm 0.040$ (N = 6, 2 SD) for MSG-1 (see Tanaka and Nakamura, 2013 in detail).

[d]From Warren et al. (2013).

Table 12:
Cr and Ti isotope data for NWA 6704.

Sample name	used sample size (mg)	Cr (ppm)*	Ti (ppm)*	ε^{53}Cr	ε^{54}Cr	ε^{46}Ti	ε^{48}Ti	ε^{50}Ti
NWA 6704 (ungrouped achondrite)	50 mg (25 mg ×2)	2200	364	0.18 ± 0.07	1.28 ± 0.08	0.23 ± 0.13	–0.01 ± 0.05	1.96 ± 0.15

*Data of Cr and Ti concentrations are from Hibiya *et al.* (2019) for NWA 6704.

Errors are propagated to include the internal errors and the uncertainty in the isotope normalization to the standards.

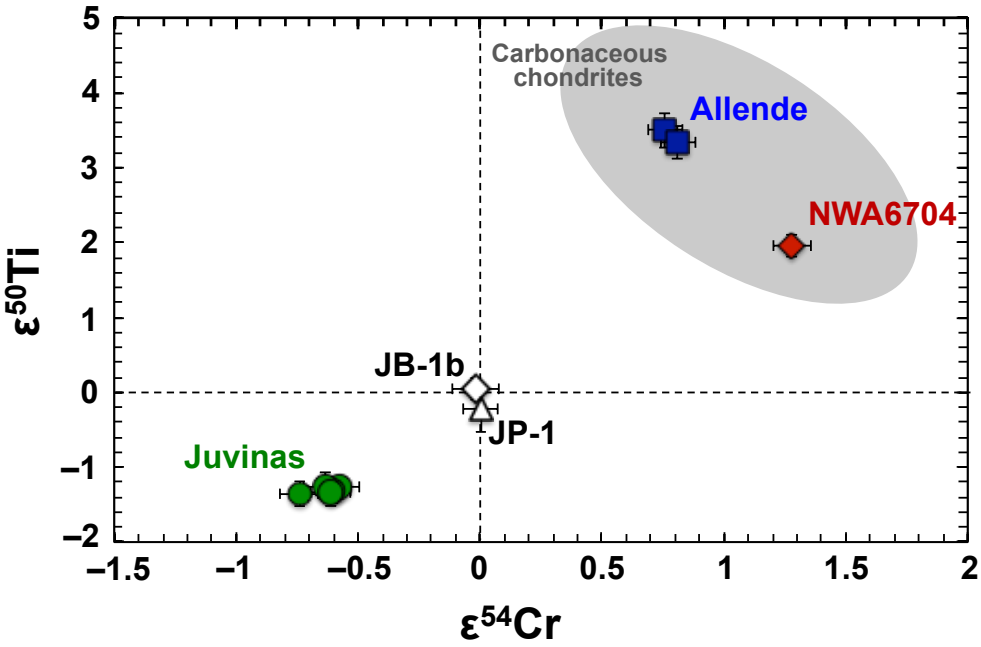

Fig. 22. Plot of ε^{50}Ti versus ε^{54}Cr for JB-1b, JP-1, Allende (2 fractions), NWA 6704, and Juvinas (5 fractions). Data sources for the shaded region of carbonaceous chondrite are as follow: ε^{54}Cr, Yamashita et al. (2005), Shukolyukov and Lugmair (2006), Trinquier et al. (2007), Yamakawa et al. (2009), Qin et al. (2010), Larsen et al. (2011), Petitat et al. (2011), Sanborn et al. (2014), Göpel et al. (2015), Bonnand et al. (2016), Schoenberg et al. (2016) and Van Kooten et al. (2016); ε^{50}Ti, Leya et al. (2008), Trinquier et al. (2009), Qin et al. (2010), Jenniskens et al. (2012) and Zhang et al. (2012).

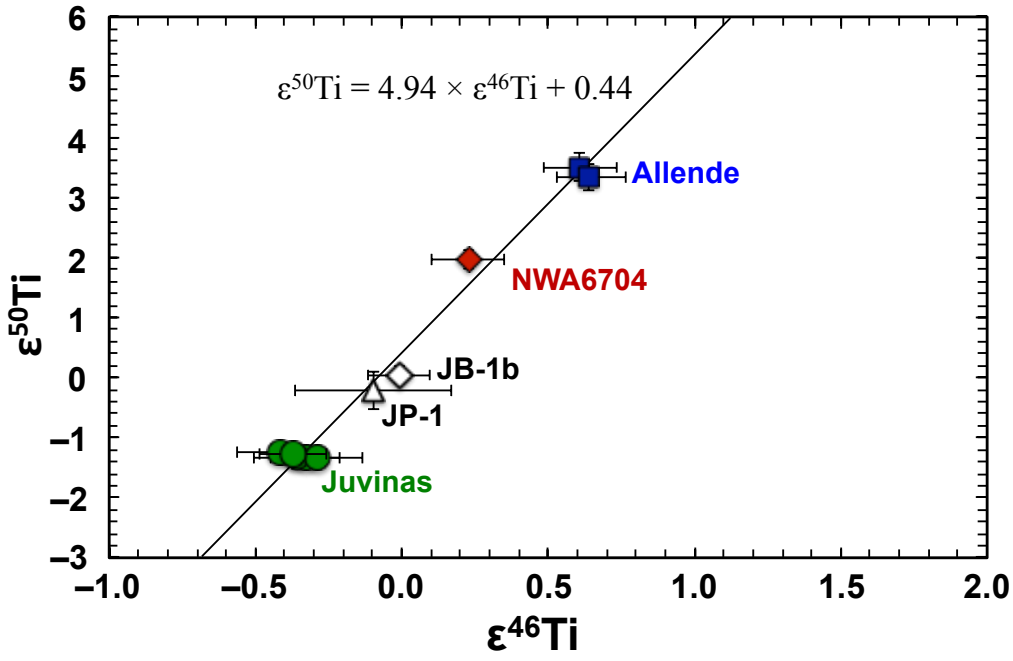

Fig. 23. Plot of ε^{50}Ti versus ε^{46}Ti for JB-1b, JP-1, Allende (2 fractions), NWA 6704, and Juvinas (5 fractions), defining a regression line of $\varepsilon^{50}\text{Ti} = (4.94 \pm 0.63) \times \varepsilon^{46}\text{Ti} + (0.44 \pm 0.25)$.

3. 4. Discussion

3. 4. 1. Crystallization process of NWA 6704

The overall texture of NWA 6704 is characterized by interlocking aggregate of orthopyroxene megacrysts with finer euhedral-subhedral olivine and anhedral plagioclase. The crystallographic consistency of the apparently isolated plagioclase domains indicates that the apparent "inclusions" are inter-connected in three dimensions, and thus orthopyroxene megacryst and plagioclase are interlocked. The dihedral angles of plagioclase against contacting two mafic crystals are very low ($\theta \leq 40^{\circ}$), but the tips of plagioclase are rounded on the scale of ~10 μm (Fig. 13–i), implying that plagioclase crystallized from melt filling interstices of mafic minerals and its morphology was frozen at the stage approaching the textural equilibrium characterized by the median angle populations of 100°–130° for granulite-grade rocks (Kretz, 1966; Vernon, 1968, 1970). In addition to these dihedral angle features, the coexistence of curvatures (or cuspate) and straight interfaces (Fig. 13–ii) is consistent with the growth of orthopyroxene narrowing melt filled spaces before the crystallization of plagioclase. Further, such facets are parallel to the c-axis of orthopyroxene (Fig. 11), indicating that the outline of plagioclase is controlled by the rational crystal facets of orthopyroxene megacrysts. These observations strongly suggest that orthopyroxene megacrysts of NWA 6704 originally had "hollow" structures, and that plagioclase filled the space of a well-connected, complex network of pores in the megacrysts.

Minor phases in NWA 6704 include pigeonite, chromite, metal, sulfides and merrillite. Pigeonite occurs as rims on some orthopyroxene megacrysts, whereas the other minor phases are intimately associated with olivine and plagioclase. These observations indicate that the orthopyroxene started to crystallize in the melt before the other phases. Moreover, the occurrence of chromite and awaruite as inclusions in olivine indicates that they crystallized earlier than olivine. On the other hand, merrillite occurs in the margin of olivine as well as orthopyroxene. Thus, the following crystallization sequence is inferred: orthopyroxene (pigeonite) → awaruite, chromite → olivine → merrillite → plagioclase. Besides, the compositional variations observed in some orthopyroxene megacrysts containing Mg-rich cores (Fig. 16) indicate that the mantle characterized by the Ca and Mg plateaus grew slightly before the crystallization of "normal" orthopyroxene, which was followed by the overgrowth of pigeonite. The chemically distinct core is considered to represent a relict grain from the precursor, which must have existed before the crystallization of the megacryst. The gradual compositional change is attributed to diffusion between the relict core and the host magma before the major crystallization stage of orthopyroxene. The vermicular olivine may also be inherited from the precursor, given that they always occur in cores of orthopyroxene megacrysts and have distinct chemical and crystallographic features from the normal olivine (Table 8).

Our EBSD mapping demonstrates that elongation of orthopyroxene megacrysts is along c-axis (Fig. 11). Such extension of single crystals in preferred growth orientations generally forms dendrites, a crystal having a branching structure with uniform lattice

and optical properties throughout (Cody and Cody, 1995). Hence, the organized subdivision into sub-parallel units of megacrysts suggests their crystallization by dendritic growth and ripening, rather than by a complex combination of nucleation or crystal aggregation (Welsch et al., 2012). Such dendritic structure of each orthopyroxene megacryst is partly recognizable in the micro-CT images (Fig. 9a).

Branching, dendritic crystals generally form under extreme super-saturation conditions (Lofgren, 1980; Vetere et al., 2015), suggesting that the initial cooling rate of NWA 6704 was very rapid. Crystal morphology as a function of cooling rate was investigated for various melts by dynamic crystallization experiments (e.g., Lofgren, 1980). The results for basaltic compositions showed that the typical crystal shape is euhedral-equant and slightly skeletal or blocky at <2 ˚C/h, elongate and skeletal to even more acicular at 2–10 ˚C/h, dendritic to spherulitic at >10˚C/h, and a feathery texture as observed in "spinifex-textured rock" (Fleet and MacRae, 1975) at >50 ˚C/h. Vetere et al. (2015) confirmed that elongated dendrites can form even by heterogeneous crystallization at cooling rates of 7–60 ˚C/h from the starting temperature of 1300 ˚C, whereas crystallization is suddenly suppressed at >1800 ˚C/h from the same starting temperature, leaving glassy products. These experiments were mostly on clinopyroxene, olivine, and plagioclase, which could show morphological behaviors distinct from orthopyroxene. Nevertheless, skeletal or dendritic orthopyroxene has been reported from rapidly solidified terrestrial rocks, such as komatiite lavas (Arndt and Fleet 1979) and orbicular diorite intrusions (Durant and Fowler, 2002), suggesting that orthopyroxene dendrite could form essentially in the same manner as clinopyroxene.

Thus, we infer that the initial cooling rate of NWA 6704 was most likely about 1–10^2 ˚C/h (dendrite formation conditions) and not higher than 10^3 ˚C/h (glass formation conditions).

The grain sizes of the NWA 6704 orthopyroxenes (0.4–1.7 cm) are significantly larger than dendritic crystals observed in eucrites or lunar and Martian basalts (μm to ~mm; Barrat et al., 2003; Walton and Herd, 2007; Hewins and Zanda, 2012). Such coarse dendritic crystals would be formed when very few nuclei exist in the superheated parental melt at the onset of cooling, so as to suppress homogeneous nucleation (Walton and Herd, 2007). Remarkably, a thin section of the fine lithology tends to contain more orthopyroxene grains with Mg-rich cores and vermicular olivine inclusions that are considered to be inherited components from the precursor (Figs. 15b and 16). The relationship may reflect that these cores acted as nuclei for the dendritic growth of orthopyroxene giving rise to megacryst formation when such nuclei are limited in number.

In contrast to the initial very high cooling rate to produce the dendritic texture for orthopyroxene, the olivine-spinel geospeedometry indicates a significantly slower cooling rate of $<10^{-4}$–10^{-2} ˚C/h at 850–970 ˚C (Fig. 17). A similar cooling rate of 2.0×10^{-2} ˚C/h at a temperature interval between 1100 and 950 ˚C is estimated from the thickness and wavelength of some augite exsolution lamellae that are similar to those observed in the Zagami martian meteorite (Brearley, 1991; Takagi et al., 2014). These results indicate that the cooling rate significantly decreased below a temperature of ~1100 ˚C during the cooling of NWA 6704.

On the basis of the textural and mineral chemical data and the above considerations, the following crystallization processes are inferred for NWA 6704: (1) the parental magma was initially dominated by melt with a few grains of relict Mg-rich orthopyroxene and vermicular olivine-bearing orthopyroxene, (2) orthopyroxene rapidly crystallized under highly super-saturation conditions, mostly on the preexisting seeds, which suppressed homogeneous nucleation and resulted in the formation of orthopyroxene megacrysts with dendritic and branching morphology, (3) as the temperature fell with decreasing cooling rate, the dendritic growth of orthopyroxene ceased and thickening of the branches proceeded with crystallization of awaruite and chromite followed by olivine and merrillite, narrowing the pore space between the orthopyroxene branches, (4) plagioclase started crystallization with limited numbers of nuclei when a interstitial residual melt was still well-connected, and eventually it completely filled the pore space.

The initial state of the crystallization can be further explored from the diffusional zoning developed around the relict Mg-rich core of orthopyroxene megacryst (Fig. 16). The average Fe^{2+}-Mg interdiffusion coefficient along the c and b axis directions of orthopyroxene at FMQ-buffered conditions can be expressed as a function of temperature and composition (Ganguly and Tazzoli. 1994);

$$\log D(\text{Fe-Mg})_{\text{c-b}} = -5.54 + 2.6\, X_{\text{Fe}} - 12530/\text{T} \qquad \text{(vii)}$$

where D is the diffusion coefficient in cm^2/s, X_{Fe} is the Fa component in orthopyroxene,

and T is the temperature in K. Using a X_{Fe} of 0.4 that is the value at the core of a chemically zoned orthopyroxene megacryst, we derive a D value of about 10^{-14} at 1000 ˚C, and a value of about 10^{-11} at 1500 ˚C, although the validity of equation (vii) remains controversial for temperatures outside the range of 500–800 ˚C. Given these D values and the diffusion distance between the relict Mg-rich core and the margin of Mg plateau (Mg# = 60.5) of about 10^{-2} cm in Fig. 16b, we estimate the time scale of superheating and cooling to be on the order of $<10^2$ yrs at 1000 ˚C, and $<\sim10^4$ h (10^{-1} yr) at 1500 ˚C. Such short time scale of melting is consistent with the presence of vermicular olivine inclusions. Reaction experiments between natural olivine crystals (Fo_{91}, Fo_{39}, and Fo_{31}) and SiO_2-rich melt at high temperatures (1100–1320 ˚C) showed that vermicular olivine can form via its partial dissolution under the conditions where the olivine has an Fe content higher than the equilibrium Fe content of olivine with the melt and when the duration of heating is short ($<10^2$ h at >1300 ˚C) enough to dissolve the Fe-rich olivine out (Tsuchiyama, 1986).

Most of the petrologic and mineral chemical features of NWA 6704 described above are consistent with those reported for paired NWA 6693, such as the intact igneous texture with the lack of shock metamorphic features, optical continuity of plagioclase over large areas, micro-inclusion alignments in plagioclase, and Ni-rich olivine, metal and sulfide compositions, even though an olivine-rich clast reported for NWA 6693 (Warren et al., 2013) has not been found in NWA 6704. Nevertheless, the inferred crystallization process is inconsistent with previously proposed cumulate origin for NWA 6693/6926 by Warren et al. (2013), who interpreted that NWA 6693

underwent an intense shock after its formation as a cumulate, causing selective melting of plagioclase and infiltration of the melt to account for the optical continuity of plagioclase. However, the dendtritic structure of orthopyroxene megacrysts and the presence of glass- and skeletal orthopyroxene-bearing inclusions in olivine (Fig. 15a) provide strong evidence for rapid cooling during crystallization of the mafic minerals. In addition, as discussed below, the rapid initial crystallization rather than cumulate origin can be more readily reconciled with the lack of chemical evidence for significant magmatic fractionation.

3. 4. 2. Highly siderophile element systematics of NWA 6704

Although the ^{187}Re–^{187}Os system cannot be used for precise dating of NWA 6704 formation because of the limited variation in Re/Os, it is useful for placing constraints on the occurrence and timing of secondary processes that may have affected the HSE in NWA 6704 fractions. The ^{187}Re–^{187}Os systematics of NWA 6704 bulk and metal fractions are generally consistent with system closure since formation, given that they fall on or near a primordial isochron (Fig. 21a). The deviation of the silicate fraction from a primordial isochron most likely indicates that a minor amount of Re has been added (Fig. 21c). Prior studies have noted similar disturbances of the Re–Os systems in some samples from Northwest Africa (Brandon et al., 2012). Despite the minor disturbance, the HSE abundances of the silicate sample were not evidently affected by

secondary processes by more than a few percent.

The relative and absolute HSE abundances of bulk fragments are broadly chondritic, but variable among individual fragments. The variation in HSE abundances indicates that HSE carriers are heterogeneously distributed on a milligram scale in NWA 6704. The heterogeneity most likely reflects a nugget effect of HSE-rich carriers, as argued by Warren et al. (2013) for paired NWA 6693. Further, some modest Re/Os variations among different bulk fragments may be partly attributed to Re/Os fractionation caused by changing redox states, as Re has the highest oxidation potential among the HSEs. Indeed, the occurrence of Fe- and Ni-rich olivine grains observed along the boundaries between large awaruite and orthopyroxene grains (Fig. 15d) suggests olivine formation via oxidation reaction of awaruite consuming orthopyroxene during cooling.

Warren et al. (2013) reported depletions in the abundances of S and chalcophile elements relative to bulk CI chondrites in paired NWA 6693. In addition to being siderophile, the HSE, and especially Pd, are also chalcophile. Sulfides in iron meteorites can have Pd abundances that are ~10% of the Pd abundances of coexisting Fe, Ni-rich metal (Carlson and Hauri, 2001). Therefore, sulfide loss may result in Pd depletions and HSE fractionations if sulfides act as a major HSE carrier. However, bulk fragments of NWA 6704 do not have Pd depletions. Therefore, despite the loss of S and chalcophile elements (and possibly sulfide phases), Pd behaved coherently with the other HSE and remained almost wholly retained in the metal. Evidently, under the formation conditions of NWA 6704, Pd behavior was far more siderophile than chalcophile.

Igneous processes should have equilibrated the HSE among metals and silicates. However, the apparent NWA 6704 metal/silicate concentration ratio for Ir is ~960. Although metal-silicate partition coefficients tend to decrease with increasing pressure and temperature for at least some HSE (e.g., Mann et al., 2012), even under P-T conditions appropriate for the terrestrial lower mantle, partition coefficients for Ir do not decrease below ~10^4. Thus, the HSE abundances of the measured NWA 6704 silicate fraction either reflect disequilibrium or the presence of some small fraction of HSE- rich metal or sulfide. Mixing calculations indicate that the presence of only 0.2% of the measured metal in a virtually HSE-free silicate fraction can broadly account for the HSE abundances in the silicate fraction. However, the relative HSE abundances of the metal and silicate fraction are not identical (Fig. 20). Therefore, metal or sulfide present in the silicate fraction must have relative HSE abundances that differ from the measured metal fraction. This may reflect restricted addition of exogenous HSE-enriched, possibly impactor materials during or subsequent to magmatic crystallization, as observed for some basaltic achondrites (Riches et al., 2012). Note, however, that such contamination should have trivial effect on the HSE systematics of bulk and metal fractions because of their higher abundances. Indeed, their ^{187}Re–^{187}Os systematics define a primordial isochron rather than a mixing line (Fig. 21a and b).

3. 4. 3. Constraints on parent body processes

Multiple processes, including core formation, silicate differentiation, and degassing, can give rise to chemical variations among different parts of planetary bodies. Immediately following core formation, the HSE concentrations of the silicate portions of planetary bodies were most likely highly depleted and fractionated, relative to chondrites (e.g., Capobianco et al., 1993) because the HSE have high ($>10^4$–10^6 under low pressure conditions) and variable metal-silicate partition coefficients (e.g., Kimura et al., 1974; Newsom, 1990; O'Neill et al., 1995; Borisov and Palme, 1995; Fortenfant et al., 2003). In addition, the HSE are typically fractionated during silicate differentiation because of their diverse compatibilities in silicate systems (e.g., Barnes and Naldrett, 1985; Walker et al., 1999; Puchtel et al., 2004, 2007; Day et al., 2010). The absolute and relative HSE abundances of a calculated whole rock, which were calculated from the four bulk fragments, are broadly chondritic (Fig. 20). Except for Pd, the HSE abundances of the estimated whole rock composition are within 2σ of carbonaceous, ordinary, enstatite, and Rumuruti-like chondrites (Fig. 24a), and one of the bulk fragments has HSE abundances that are within 2σ of ordinary chondrites for all HSE, including Pd. The HSE of NWA 6704 are also less fractionated than primitive achondrites, including ureilites, brachinites, brachinite-like achondrites, and GRA 06129 (Fig. 24b). Further, Warren et al. (2013) reported that the relative and absolute abundances of siderophile elements (including Co, Ni, Ir, Os, and Au) and non-volatile lithophile elements of paired NWA 6693 are only minimally fractionated relative to

bulk chondrites. The nearly chondritic absolute and relatively unfractionated HSE abundances of NWA 6704 and NWA 6693 indicate that their precursor rocks most likely had chondritic absolute and relative HSE abundances, and that they crystallized from a melt that underwent only minor metal and sulfide fractionation. This, in turn, suggests that a parent body had not segregated metal or sulfide on a global scale to form a core by the time the samples formed.

The significance of the parent body differentiation can be further constrained from other geochemical systematics of NWA 6704. Silicate differentiation processes including crystal accumulation should cause significant fractionation between elements having highly different compatibilities in silicate systems. The CI chondrite-normalized REE pattern of NWA 6704 is compared with those of NWA 6693 and primitive achondrites in Fig. 19. The absolute abundances of REE in NWA 6704 and NWA 6693 are slightly sub-chondritic (0.4–0.7 × CI), which led some to argue its cumulate origin (Jambon et al., 2012; Warren et al., 2013). However, the only weakly fractionated REE patterns of NWA 6704 and NWA 6693 (Fig. 19), together with the lack of systematic depletion of highly incompatible lithophile and siderophile elements (Figs. 18b and 20), require that neither the parental magma nor precursor underwent significant silicate differentiation.

A plot of Fe/Mn ratio vs. Fe/Mg ratio (Fig. 25) can be used to evaluate chemical fractionation during planetary processes, because (1) silicate differentiation is accompanied by variation in Fe/Mg ratio with minor Fe/Mn fractionation, (2) metal-silicate segregation causes correlated changes in Fe/Mn and Fe/Mg ratios, and (3)

volatility-controlled differentiation can lead to more variation in Fe/Mn ratio than in Fe/Mg ratio (Goodrich and Delaney, 2000). Like primitive achondrites, NWA 6704 yields a Mn/Mg ratio (~1.06 × CI) within the range of chondritic ratios. As compared to primitive achondrites including lodranites and winonaites/IAB (~0.73 × CI and ~0.65 × CI, respectively), NWA 6704 has Fe/Mn and Fe/Mg ratios (Fe/Mg ~1.18 × CI; Fe/Mn ~1.11 × CI) similar to those of carbonaceous chondrites, which is consistent with the restricted silicate differentiation and metal-silicate segregation.

NWA 6704 is severely depleted in elements having Tc of <900 K, relative to the reference CI chondrite (Fig. 18b). Such depletion is recognizable for NWA 6693, but the degrees of the depletion are remarkably different between the two meteorites especially for Rb, Pb, and Te (Table 9). Further, a whole rock sample of NWA 6693 used for Rb–Sr dating has a nearly chondritic Rb abundance of 3.2 μg/g, which is one order of magnitude higher than that of NWA 6704 (Amelin et al., 2019). As a result of the Rb abundance variation, mineral separates of NWA 6704 and NWA 6693 yielded clearly distinct $^{87}Rb/^{86}Sr$ and $^{87}Sr/^{86}Sr$ ratios, but the Rb–Sr isotope data define a single isochron with an age of 4.54 ± 0.03 Ga, which is consistent with the Pb–Pb and Al–Mg ages (Amelin et al., 2019; Sanborn et al., 2019). This indicates that the observed Rb variation was established at or around the time of crystallization, implying that the depletion of the highly volatile element with variable degrees resulted from a high-temperature magmatic event forming NWA 6704 and NWA 6693.

Limited chemical fractionation among elements with T_C > 900 K indicates that the effects of planetary differentiation processes must have been restricted for NWA

6704 and NWA 6693 compared to primitive achondrites characterized by more fractionated chemical compositions. The large-scale distributions of HSE-rich carriers (primarily metal and sulfides) in NWA 6704 appear to have been largely unchanged during melting and crystallization. Transport of these carriers must have therefore been limited. Moreover, fractional melting in the precursor and crystal accumulation in the parental magma should have been insignificant. One possibility for the restricted differentiation despite melting and crystallization is that the NWA 6704 parent body was too small for gravitational separation of metals, sulfides or silicate minerals from melt. Alternatively, melting and crystallization may have happened on a timescale that was too short to allow segregation of these phases. The latter is compatible with the petrological observations suggesting instantaneous melting followed by rapid crystallization. Plausibly, a chondrite-like precursor to NWA 6704 was rapidly heated well above liquidus temperature such that the generated melt contained a limited number of relics from the precursor and retained the primitive chemical features except for the highly volatile elements with Tc of <900 K that were lost by degassing. This rapid heating was immediately followed by rapid cooling, which resulted in the formation of dendritic orthopyroxene megacrysts and prevented silicate differentiation and metal/sulfide segregation. Such precipitous thermal phenomenon may be implemented by an impact event, even though no unambiguous mineralogical evidence for this proposal, such as the presence of high-pressure phases, is preserved in NWA 6704.

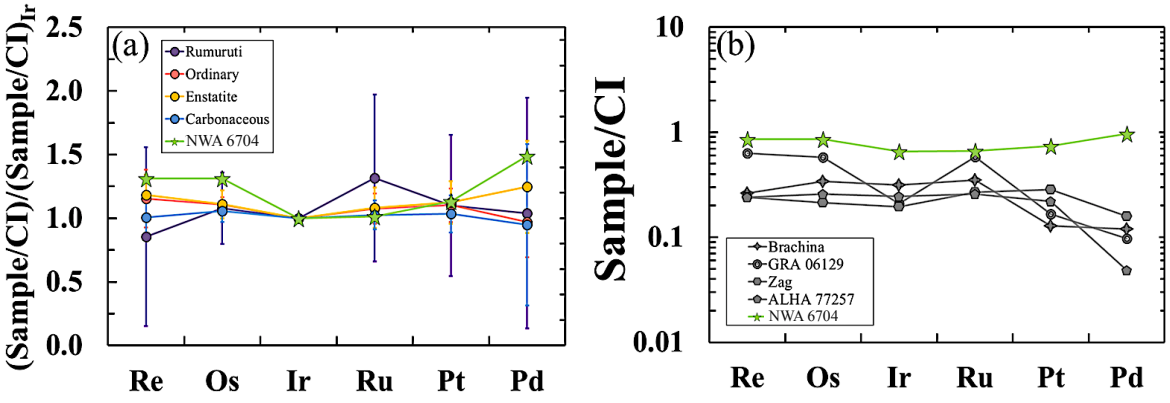

Fig. 24. CI-normalized (Horan et al., 2003) highly siderophile element (HSE) abundances of NWA 6704 whole rock, compared with those of (a) chondrite groups and (b) achondrites. HSE abundances in (a) are doubly normalized to CI chondrites (Horan et al., 2003) and Ir. For comparison, doubly normalized average and 2σ of ordinary, carbonaceous, enstatite, and Rumuruti-like chondrites HSE abundances are also shown in (a). The HSE abundances of NWA 6704 whole rock in (b) are normalized only to CI chondrites (Horan et al., 2003). For comparison, CI-normalized HSE abundances of various primitive achondrites are also shown in (b). The plots for ordinary, carbonaceous, enstatite, and Rumuruti-like chondrites are based on the data reported by Walker et al. (2002), Horan et al. (2003), Brandon et al. (2005), Fischer-Gödde et al. (2010) and Day et al. (2015). Data for GRA 06129 are from Day et al. (2009), Brachina and Zag from Day et al. (2012), and ALHA 77257 from Rankenburg et al. (2008).

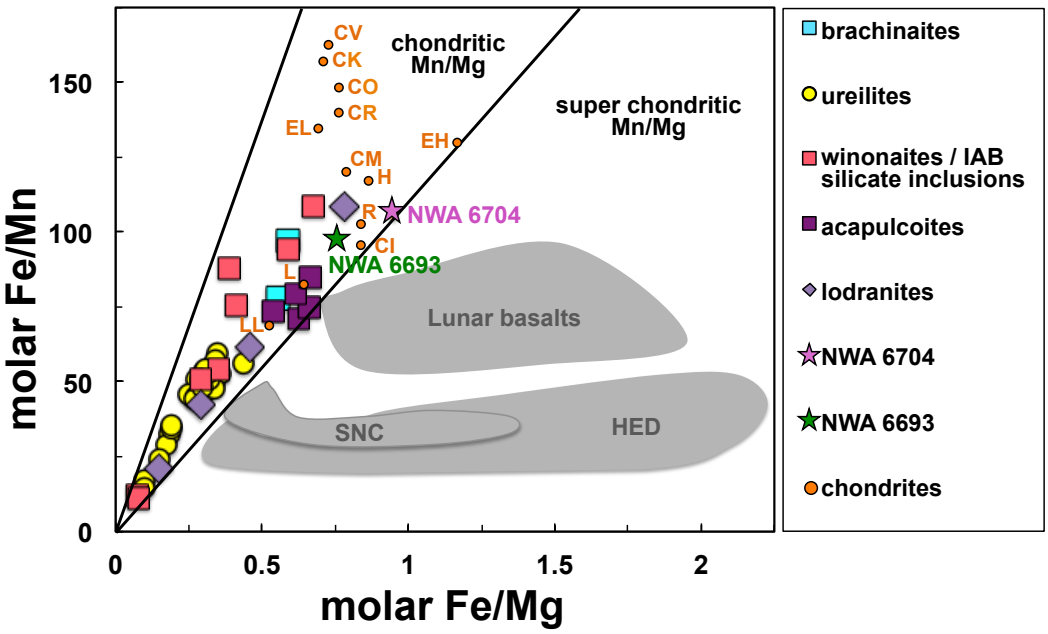

Fig. 25. Plot of Fe/Mn vs. Fe/Mg, comparing NWA 6704 with chondrites, primitive achondrites, HED/SNC, and lunar basalts (Goodrich and Delaney, 2000 and the references listed there). The NWA 6704 data shown here were obtained with XRF.

3. 4. 4. Constraints on the provenance of the parent body

The O isotope compositions of meteorites have long been used to investigate their parent bodies, since different meteorite groups and, by extension, different planets have distinct $\Delta^{17}O$ values, probably as a result of isotope-selective photo-dissociation of CO in the early solar nebula (Clayton, 2002; Yurimoto and Kuramoto, 2004; Lyons and Young, 2005). More recently, it has been shown that each meteorite group has distinctive mass independent isotope variations of heavier elements such as Ti, Cr, and Ni (Trinquier et al., 2007, 2009; Dauphas and Schauble, 2016, and references therein). In particular, carbonaceous chondrites have substantially higher values of $\varepsilon^{54}Cr$ and $\varepsilon^{50}Ti$ as compared to most differentiated meteorites and ordinary and enstatite chondrites. The carbonaceous chondrite parent bodies (C-type asteroids) are considered to have accreted in the outer solar system and then implanted into the main asteroid belt (Walsh et al., 2011). Thus, the isotope data are interpreted to reflect distinct isotope features between the inner and outer early solar nebula (Warren, 2011; Budde et al., 2016; Van Kooten et al., 2016; Kruijer et al., 2017). This potentially offers a new means of assessing the parent body provenance, even though the cause of the isotope variations is a matter of on-going debate (e.g., Trinquier et al., 2009; Dauphas et al., 2010; Qin et al., 2011). In Fig. 26, we compare the O–Cr–Ti isotope systematics of NWA 6704 and other planetary materials. The comparison shows that NWA 6704 plots within the range of carbonaceous chondrites. This correspondence suggests that its parent body sampled the same reservoirs of O, Cr and Ti in the outer solar system as the carbonaceous

chondrite parent bodies. If so, it is likely that the precursor of NWA 6704 was originally hydrous, but water was lost during the magmatic event together with the highly volatile elements such as Rb. The empty inclusions observed in the orthopyroxene megacrysts (Fig. 12a,b) may represent a vestige of trapped fluid that was derived from the hydrous precursor.

NWA 6704 shows further similarities to carbonaceous chondrites in fO_2 and refractory major element abundances. The fO_2 of NWA 6704 (FMQ −2.6) estimated from the olivine-spinel geobarometry is similar to those of CV chondrites and distinctly higher than those of ordinary and enstatite chondrites (Righter and Neff, 2007), suggesting its parent body accretion in a relatively oxidized environment. The Al/Mg and Ca/Mg ratios in NWA 6704 (Al/Mg ~1.27 × CI; Ca/Mg ~1.06 × CI) are within the range of carbonaceous chondrite values (Al/Mg 0.98–1.37 × CI; Ca/Mg 0.97–1.38 × CI), while those ratios are distinctly lower in non-carbonaceous chondrites (Al/Mg 0.84–0.93 × CI; Ca/Mg 0.75–0.94 × CI) that have lower abundances of refractory Ca-Al-rich inclusions (CAIs) in non-carbonaceous chondrites (e.g., Palme, 2000; Rubin, 2011) (Fig. 27).

On the other hand, NWA 6704 is clearly distinct from both carbonaceous and non-carbonaceous chondrites in its high Si/Mg (~1.85 × CI; chondrites and primitive achondrites 0.62–1.40 × CI). Such elevated Si/Mg ratio is observed also in NWA 6693 (Warren et al., 2013) and results in their higher modal ratios of low-Ca pyroxene to olivine than those in carbonaceous chondrites. The high Si/Mg ratio in NWA 6704 cannot be attributed to igneous differentiation on its parent body, because the nearly

chondritic HSE and only weakly fractionated REE patterns preclude significant magmatic fractionation (previous section). Aqueous alteration processes are incapable of fractionating Si from Mg without a remarkable change of Fe/Mg ratio (Tomeoka and Buseck, 1985; McSween, 1987) that is not observed in NWA 6704. It is difficult to account for the increased Si/Mg ratio by volatilization processes on the parent body, given the rather chondritic Na/Mg and K/Mg ratios in NWA 6704 and NWA 6693 (Fig. 27) despite more volatile features of Na and K relative to Si. Instead, the Si enrichment in NWA 6704 may result from cosmochemical fractionation in the solar nebula that is thought to be responsible for Si/Mg variations among different chondrite groups (Larimer, 1979).

It has long been known that carbonaceous and non-carbonaceous chondrites define distinct trends in a Mg/Si vs. Al/Si diagram (Fig. 28) (Jagoutz et al., 1979; Larimer, 1979; Alexander, 2005): there are little Mg/Si variations but significant Al/Si variations for carbonaceous chondrites, whereas correlated variations between Mg/Si and Al/Si ratios are observed for non-carbonaceous chondrites. On the basis of predicted condensation sequence for the cooling solar nebula, the cosmochemical trend for carbonaceous chondrites has been considered to reflect the addition of the earliest condensates to the solar (CI) composition, whereas that for non-carbonaceous chondrites has been explained by the removal of forsterite and earlier condensates (Larimer, 1979). The nebular fractionation of forsterite is consistent with a more recently recognized correlation between the Mg/Si ratios and Si isotopic compositions of different meteorite groups (Fitoussi et al., 2009; Dauphas et al., 2015).

If the significantly lower Mg/Si ratio in NWA 6704 (Mg/Si ~0.52 × CI) is due to the nebular fractionation, then the NWA 6704 parent body likely formed in a region of the protoplanetary disk where the forsterite component was significantly depleted as compared to the accretion regions of any known chondrites. At the same time, the remarkable deviation of NWA 6704 from the non-carbonaceous chondrite trend (Fig. 28) suggests that the most refractory component was relatively enriched in the region. Given that CAIs and refractory presolar materials exhibit high ε^{54}Cr and ε^{50}Ti values (e.g., Choi et al., 1998; Trinquier et al., 2009; Qin et al., 2010; Kööp et al., 2016), the refractory component enrichment in NWA 6704 can account for its carbonaceous chondrite-like Ti and Cr isotopic compositions despite of its non-chondritic Mg/Si ratio.

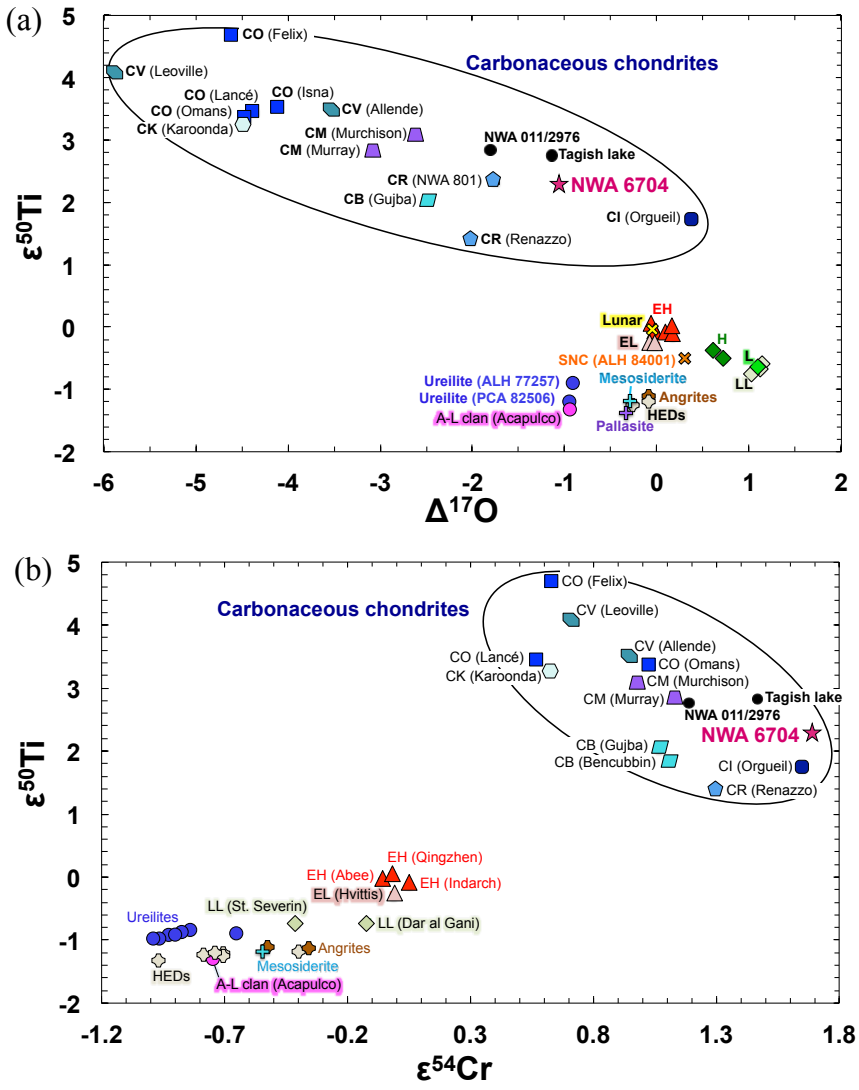

Fig. 26. Comparisons of isotope compositions of NWA 6704 with planetary materials: (a) ε^{50}Ti vs. Δ^{17}O; (b) ε^{50}Ti vs. ε^{54}Cr. Data sources are as follow: Δ^{17}O, Clayton et al. (1991), Clayton and Mayeda (1996, 1999), Franchi et al. (1999), Newton et al. (2000), Greenwood et al. (2004, 2005, 2010, 2012), Wiechert et al. (2001, 2004), Scott et al. (2009), Schrader et al. (2011) and Harju et al. (2014); for ε^{50}Ti, Trinquier et al. (2007, 2008, 2009), Leya et al. (2008), Qin et al. (2010 a,b) Yamakawa et al., (2010) and Zhang et al. (2012); for ε^{54}Cr, Yamashita et al. (2005), Shukolyukov and Lugmair, (2006a,b), Trinquier et al. (2007), Shukolyukov et al. (2009, 2011), Qin et al. (2010 a,b), Göpel and Birck, (2010), Yamakawa et al., (2010), Larsen et al. (2011), Petitat et al. (2011), Qin et al. (2011), Sanborn et al. (2014), Bonnand et al. (2016), Göpel et al. (2015), Sanborn et al. (2015), Schmitz et al. (2016) and Schoenberg et al. (2016).

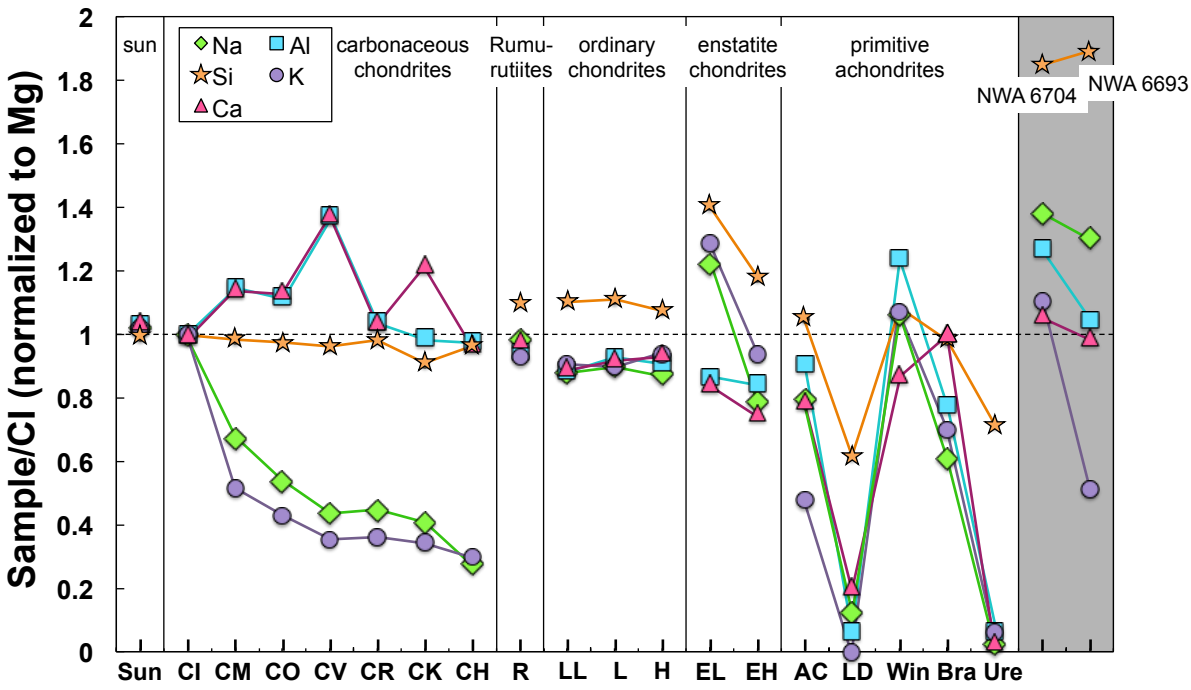

Fig. 27. Mg and CI-normalized whole rock elemental abundances of NWA 6704 (XRF data in Table 9), compared with those of Sun (Palme and Beer, 1993), various chondrites (CI, CM, CO, CV, CR, CK, CH, LL, L, H, EH and EL from Wasson and Kallemeyn, 1988; R from Schulze et al., 1994) and primitive achondrites (Acapulcoite from Palme et al., 1981; Lodranite and Brachinite from Mittlefehldt et al., 1998; Winonaite from Graham et al., 1977; Ureilite from Wiik, 1972; NWA 6693 from Warren et al., 2013).

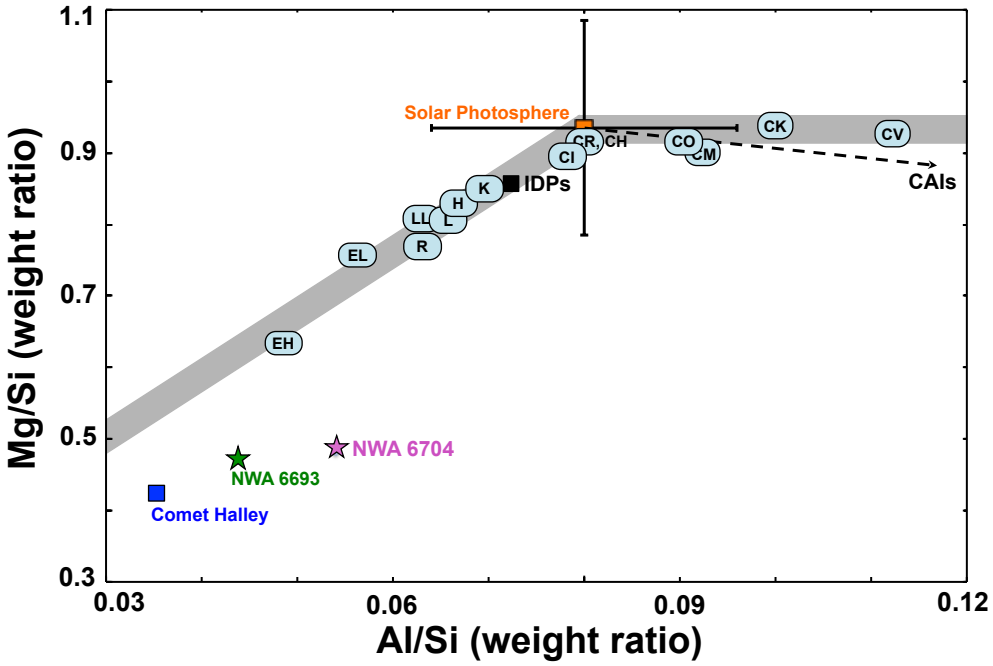

Fig. 28. Plot of Mg/Si vs. Al/Si diagram, comparing NWA 6704 (XRF data in Table 9) with solar photosphere, chondrites, primitive materials (IDPs from Schramm et al., 1989; Comet's Halley dust from Jessberger et al., 1988), and NWA 6693 (Warren et al. 2013). The gray bars show two distinct trends intersect at solar composition; one is defined by carbonacous chondrites, and the other by non-carbonaceous chondrites.

3. 4. 5. Potential of NWA 6704 as a new "*Time anchor*"

Based on our petrological, geochemical, and isotope cosmochemical study of NWA 6704, we finally discuss the potential utility of this meteorite as a new anchor to map extinct radionuclide chronometers onto an absolute time scale ("*Time anchor*"; see section 1.1.1.). As mentioned above, to be the *Time anchor*, one meteorite must satisfy the following conditions to tie Nb–Zr age to an absolute U–Pb chronology (Fig. 1): (1) The U–Pb age can be obtained (while the short-lived radionuclide was still alive); (2) an (internal) isochron of the short-lived radionuclide can be obtained. In other words, the chemical fractionation of a parent element from its radiogenic daughter element results in a linear correlation of excesses of the daughter isotope with the relative abundance of the parent isotope; (3) a cooling rate is rapid enough not to cause the age difference exceeding the range of the error (isotopic closure is rapidly achieved). (4) sample is not affected by secondary alternation or exotic components that disturbed the age.

Given the high-precise ancient U-Pb age (4562.76 ± 0.30 Ma) determined by (Amelin et al., 2019) and the modal composition of mineral assemblage that makes internal isochron dating with various extinct radionuclide chronometers applicable (Table 13), NWA 6704 satisfies the condition of (1) and (2). The inferred rapid cooling rate (> 10^{-1} ℃/yr) during crystallization is rapid enough to cover the differences in closure temperatures (up to several hundred degrees) of multiple chronometers within thousands of years (~0.001 Ma). Considering that the current techniques can have precisions of 0.1–1.0 Ma in isotope dating (e.g., Connelly et al., 2012; Amelin et al.,

2019), the cooling rate of NWA 6704 does not affect the age interpretation. Our finding of the relict grain such as vermicular olivine (Fig. 15b) and some Mg-rich cores in orthopyroxene (Fig. 16) suggests the presence of exotic components within this meteorite. However, such exotic grains are also observed in the quenched angrites including D'Orbigny (Mikouchi et al., 2011), which is currently the most widely used *Time anchor* (Glavin et al., 2004; Brennecka and Wadhwa 2012; Spivak-Birndorf et al., 2009; Schiller et al., 2010a; Schiller et al., 2015). Compared with the sizes of xenocrysts in D'Orbigny up to 3 mm (Mikouchi et al., 2011), the relict grains with sizes less than 500 μm observed in this study is negligible. Given these facts and the textures indicative of limited weathering and a very low shock stage (S1–S2), NWA 6704 also satisfies the condition of (3) and (4). Consequently, our study can reasonably suggest that NWA 6704 ungrouped primitive achondrite is a viable, new *Time anchor*.

Importantly, as discussed in the previous section, the O, Cr and Ti stable isotope comparison (Fig. 26) shows that the parent body of NWA 6704 sampled the same reservoirs of O, Cr and Ti in the outer solar system as the carbonaceous chondrite parent bodies. Those O, Cr and Ti isotope systematics indicate that the NWA 6704 parent body was accreted in a different region from the parent body of angrite, which is now widely used as *Time anchor* (e.g., D'Orbigny, $\varepsilon^{54}Cr = -0.46 \pm 0.09$, 2 SE; Yamashita et al., 2015; $\varepsilon^{50}Ti = -1.55 \pm 0.22$, 2 SE; Trinquier et al., 2009). Further, the Cr and Ti isotope systematics of all meteorites previously studied for determining the initial ^{92}Nb abundance (angrites, eucrites, Ibitira ungrouped achondrite, ordinary chondrites, and Vaca Muerta mesosiderites; Fig. 29) are plotted within the region of non-carbonaceous

chondrites, suggesting that their parent bodies sampled the same reservoirs of O, Cr, and Ti in the inner solar system (originated from < ~5 astronomical units (AU); Warren, 2011). This is consistent with the volatility-depleted nature of these meteorites, which have been mentioned in section 1.2. Hence, newly establishing NWA 6704 as a *Time anchor* and applying the internal Nb–Zr isochron approach to this meteorite would allow us to evaluate spatial distribution of ^{92}Nb in the solar nebula, between the inner and outer solar system.

Table 13: Summary of short-lived isotope chronometers applicable to NWA 6704.

Parent - Daughter	Half-life	Usable minerals
^{26}Al → ^{26}Mg	717 Kyr	Pl – Olv, Px
^{60}Fe → ^{60}Ni	2.6 Myr	Chr – Metal
^{53}Mn → ^{53}Cr	3.74 Myr	Olv – Chr
^{182}Hf → ^{182}W	8.9 Myr	Px – metal
^{92}Nb → ^{92}Zr	37 Myr	Px – Chr
^{146}Sm → ^{142}Nd	68 Myr	Chr, Px – Pl

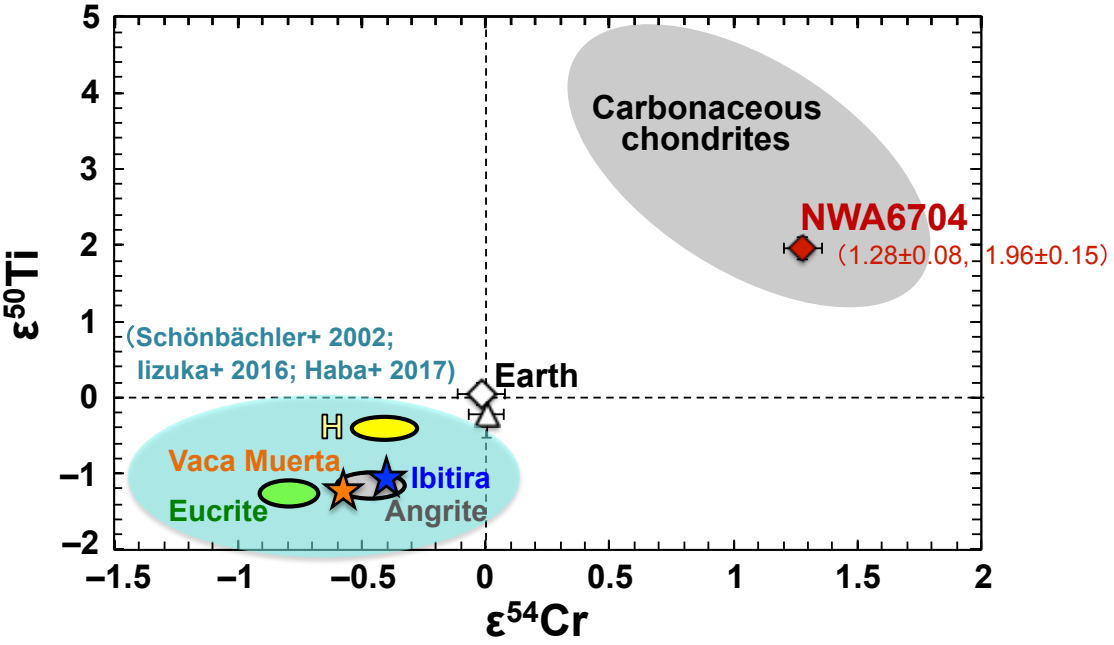

Fig. 29. Comparisons of Cr-Ti stable isotope compositions of NWA 6704 with all samples previously studied using the internal Nb-Zr isochron approach: Data sources are Yamashita et al. (2005), Trinquier et al. (2007, 2009), Larsen et al. (2011), Zhang et al. (2012), and Sanborn et al. (2014).

3. 5. Conclusion

The unique achondrite NWA 6704 consists of orthopyroxene megacrysts with finer interstitial crystals of olivine, chromite, awaruite, sulfides, plagioclase and merrillite. The petrology, morphology and mineral chemistry collectively indicate the following crystallization sequence for NWA 6704: (1) melt-dominant state with a few grains of relict Mg-rich orthopyroxene and vermicular olivine-bearing orthopyroxene, (2) following rapid growth of orthopyroxene mostly on the pre-existing seeds under high super-saturation conditions, which suppressed homogeneous nucleation and resulted in the formation of orthopyroxene megacrysts (up to ~1.7 cm) with dendritic and branching morphology, (3) as the temperature fell, dendritic growth of orthopyroxene ceased and thickening of branches proceeded with crystallization of awaruite and chromite followed by olivine and merrillite in the pore space between the orthopyroxene branches, and (4) finally plagioclase crystallized with limited numbers of nuclei and filled the well-connected pore space, resulting in the interlocking between plagioclase and othropyroxene megacrysts. The diffusional zoning profile in a high Mg# pyroxene core, together with the presence of vermicular olivine inclusions, indicates that the initial melt-dominant state was instantaneous. The dendritic textures of orthopyroxene also indicate its rapid crystallization under super-cooling ($1–10^2$ ˚C/hour) conditions. By contrast, the olivine–spinel geospeedometry records the notable decrease in cooling rate at a later stage of crystallization ($<10^{-4}–10^{-2}$ ˚C/hour at below ~1100 ˚C).

The Re–Os isochron age of 4576 ± 250 Ma, defined by the bulk and metal fractions, suggests system closure since crystallization. The roughly chondritic HSE abundances of the bulk fragments with only weakly fractionated HSE and REE patterns require that the parental melt and precursor had undergone neither significant segregation of metals, sulfides, nor silicate minerals. Furthermore, the variable degrees of depletion in elements having Tc of <900 K relative to chondrites suggest volatilization of the elements during the magmatism to form NWA 6704. The limited chemical fractionations among moderately and highly refractory elements during the igneous event can be attributed to the short-time scale of the melting of the precursor and following crystallization. The precipitous thermal event might occur as a result of an impact event, even though no diagnostic impact features are observed in the mineralogy of NWA 6704. Such impact melting has been previously inferred for the origin of acapulcoites, lodranites, and ureilites (Rubin, 2007; Warren and Rubin, 2010), while others have proposed that the internal radioactive decay of ^{26}Al was the heat source for melting and metamorphism of these meteorites (e.g., McCoy et al., 1996; Touboul et al., 2009; Keil and McCoy, in press). The consistent U–Pb (4562.76 +0.22 0.30 Ma: Amelin et al., in press), Al–Mg (4563.13 ± 0.27 Ma, Sanborn et al., in press) and Mn–Cr ages (4562.17 ± 0.76 Ma, Sanborn et al., in press) of NWA 6704 indicate that the parent body accreted within ~4 Ma after CAI formation. It is, therefore, most likely that the parent body was internally heated by ^{26}Al decay. However, heating solely by the internal radioactive decay would not cause rapid melting well above liquidus temperature as inferred for NWA 6704. We envision that an impact event on the

radioactively heated, but not differentiated parent body induced a regional instantaneous melting up to a super-liquidus temperature immediately followed by rapid cooling. As a result, coarse orthopyroxene dendrites crystallized from the generated melt having a chondritic composition on the surface. The decrease of cooling rate in the late stage of the crystallization may reflect its burial under hot debris piled up within an ejecta blanket. Assuming that the cooling proceeded essentially by thermal conduction with a thermal diffusivity of 10^{-7} m^2/second (Horai and Winkler, 1974), the burial depth is estimated to be on the order of ~10^2 m.

The O, Cr and Ti isotope compositions of NWA 6704 are similar to those of carbonaceous chondrites and distinct from those of non-carbonaceous chondrites. Further similarities between NWA 6704 and carbonaceous chondrites are observed in fO_2 and refractory major element abundances such as Ca/Mg and Al/Mg ratios. However, NWA 6704 has a Mg/Si ratio significantly lower than observed in carbonaceous chondrites and non-carbonaceous chondrite trend. These findings imply that the NWA 6704 parent body formed under oxidized conditions in an outer region of the solar system where nebular fractionation of forsterite and earlier condensates proceeded efficiently, followed by implantation of a refractory component having elevated ε^{54}Cr and ε^{50}Ti values.

All results support this meteorite to be used as a viable, new "*Time anchor*". Further, the O, Cr and Ti stable isotope comparison shows that the parent body of NWA 6704 sampled the different reservoirs of O, Cr and Ti from those of all meteorites previously studied for determining the initial ^{92}Nb abundance (angrites, eucrites, Ibitira

ungrouped achondrite, ordinary chondrites, and Vaca Muerta mesosiderites). Hence, newly establishing NWA 6704 as a *Time anchor* and applying the internal Nb–Zr isochron approach to this meteorite, we can further clarify the homogeneous distribution of ^{92}Nb in the solar nebula between the inner and outer solar system.

4. ^{92}Nb–^{92}Zr chronology

4. 1. Background

^{92}Nb decays to ^{92}Zr by electron capture with a half-life of 37 million years (My) (Holden, 1990). Both Nb and Zr are refractory (Lodders, 2003) and strongly incompatible elements. These elements can be fractionated from each other during the silicate partial melting and crystallization as well as and the metal-silicate separation (e.g., Tiepolo et al., 2001; Münker et al., 2017), making the Nb-Zr system to be promising chronometer for addressing the early solar system evolution. Figure. 30 shows a nuclear chart for isotopes having nuclear masses around ^{92}Nb (A = 92). As shown in the figure, ^{92}Nb is shielded from β decays from other nuclides due to the presence of surrounding stable isobars (^{92}Mo and ^{92}Zr). Thus, ^{92}Nb is a rare "*p*-process-only" nuclide, which cannot be synthesized by the rapid(r) or slow(s) neutron captures, and can only be synthesized by direct nuclear reactions such as (γ, n) and (ν, ν'n) reactions on ^{93}Nb and (ν_e, e^-) reaction on ^{92}Zr. This makes ^{92}Nb to be a promising monitor for constraining the origin of nucleosynthetic isotope variations in the early solar system. In addition, the potential of ^{92}Nb as a nuclear cosmochronometer has long been recognized (Minster and Allegre 1982; Wasserburg et al., 1996), once the stellar origin of ^{92}Nb is well established. The initial abundance of now-extinct ^{92}Nb and its distribution at the start of solar system are, therefore, required to be clearly determined for both chronological and astrophysical points of view.

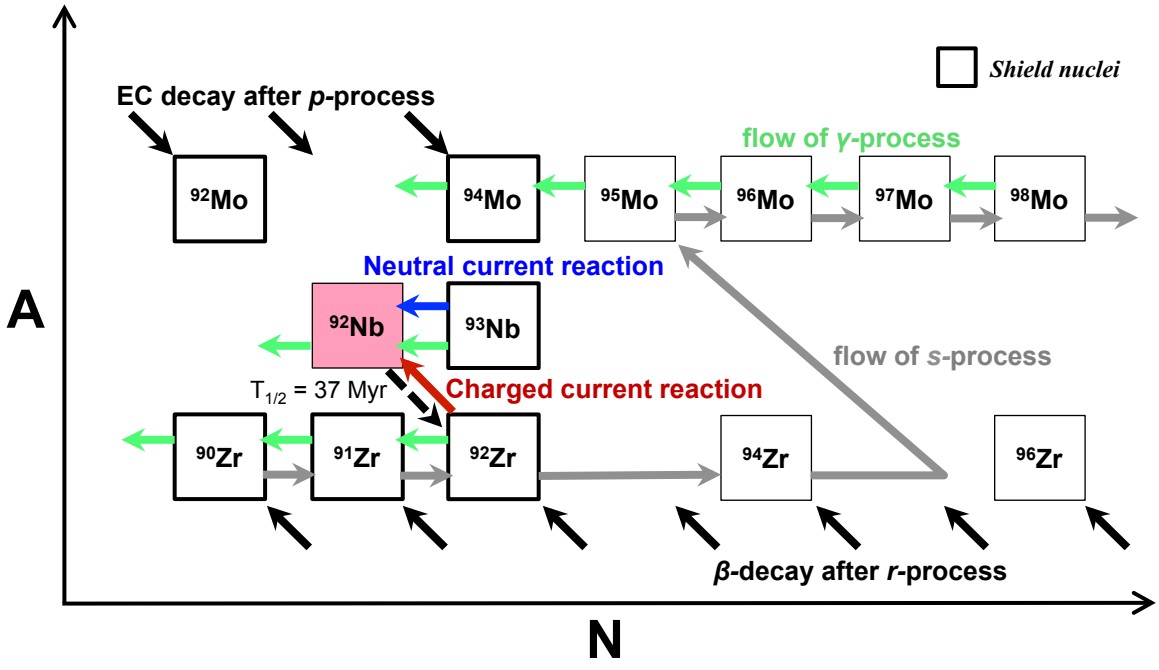

Fig. 30. Nuclear chart around ^{92}Nb and the relevant nucleosynthesis flows.

The best way to determine the initial abundance of ^{92}Nb at the time of solar system formation is to apply the internal mineral isochron approach to a fresh meteorite in which the ancient high precision U-Pb absolute age is known, i.e., *Time anchor*. In the Nb-Zr decay system, the decay equations of (i) ~ (iv) in section 1.1.1. are rewritten as follows;

$$(^{92}Zr / ^{90}Zr)_{present} = (^{92}Zr / ^{90}Zr)_{initial} + (^{92}Nb / ^{90}Zr)_{initial} \times (1 - e^{-\lambda T}) \qquad (i)'$$

where subscripts "present" and "initial" refer at the present and the time of the system closure (at T), and λ is the decay constant for the parent nuclide.

Because the age T is much larger than the half-life of short-lived parent nuclide ^{92}Nb, $(^{92}Nb / ^{90}Zr)_{initial} \times (1 - e^{-\lambda T})$ approaches to the value of $(^{92}Nb / ^{90}Zr)_{initial}$, and equation (i)' is rewritten as follows;

$$(^{92}Zr / ^{90}Zr)_{present} = (^{92}Nb / ^{90}Zr)_{initial} + (^{92}Nb / ^{93}Nb)_{initial} \times (^{93}Nb / ^{90}Zr)_{present} \qquad (ii)'$$

Hence, an Nb-Zr internal isochron (Fig. 31) on a plot of $(^{92}Zr / ^{90}Zr)_{present}$ vs. $(^{93}Nb / ^{90}Zr)_{present}$ gives a slope corresponding to $(^{92}Nb / ^{93}Nb)_{initial}$. Furthermore, $(^{92}Nb / ^{93}Nb)_{initial}$ can be related to the ratio at the time of solar system formation $(^{92}Nb / ^{93}Nb)_0$:

$$(^{92}Nb / ^{93}Nb)_{initial} = (^{92}Nb / ^{93}Nb)_0 \times e^{-\lambda \Delta t} \qquad (iii)'$$

where Δt is the time interval between the system closure and solar system formation (Δt = 4567.3 Ma – T; Connelly et al., 2012). This equation is rewritten as follows:

$$\Delta t = -(\ln[(^{92}Nb / {}^{93}Nb)_{initial} / (^{92}Nb / {}^{93}Nb)_0]) / \lambda \qquad \text{(iv)'}$$

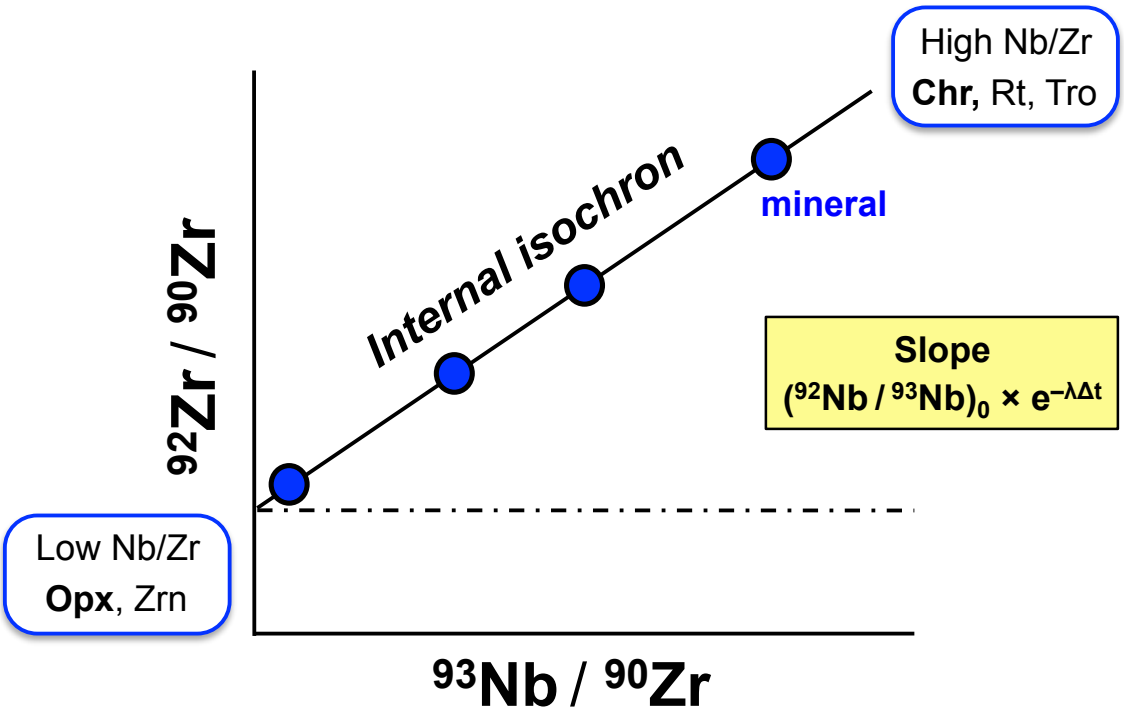

Fig. 31. Schematic diagram of internal ^{92}Nb–^{92}Zr mineral isochron. A plot of (^{92}Zr / ^{90}Zr) vs. (^{93}Nb / ^{90}Zr) gives a slope corresponding to $(^{92}Nb / {}^{93}Nb)_0 \times e^{-\lambda\Delta t}$, where ($^{92}Nb$ / $^{93}Nb)_0$ is the Nb isotopic ratio at the time of solar system formation. Minerals with high Nb/Zr include chromite, rutile, and troilite. Minerals with low Nb/Zr include pyroxenes, and zircon.

As described above, NWA 4590 angrite has been the only meteorite that satisfies the conditions to be used as a *Time anchor* for the Nb-Zr system. The internal isochron applied to this meteorite showed the slope of $(1.4 \pm 0.5) \times 10^{-5}$ at the time of the system closure, i.e., the U-Pb age of 4557.93 ± 0.36 Ma (Amelin et al., 2011a). Using this meteorite as *Time anchor*, the initial ^{92}Nb abundance at the solar system formation was determined to be $(^{92}Nb/^{93}Nb)_0 = (1.7 \pm 0.6) \times 10^{-5}$ (Iizuka et al. 2016). Further, all initial values obtained after Schönbächler et al. (2002) using the internal isochron approach are consistent with each other. The concordance has been interpreted as reflecting a homogeneous distribution of ^{92}Nb at the canonical value of $(^{92}Nb/^{93}Nb)_0 = (1.7 \pm 0.6) \times 10^{-5}$ in the early solar system.

In this study, we determined the initial abundance of ^{92}Nb ($^{92}Nb/^{93}Nb$) by applying the internal isochron approach to the NWA 6704 primitive achondrite. As concluded in the chapter 3, our petrological, geochemical, and isotope study of NWA 6704 suggested that this meteorite is a viable, new *Time anchor*. Furthermore, since the parent body of NWA 6704 samples the same reservoirs of Δ^{17}O, ^{54}Cr, ^{50}Ti, and ^{84}Sr as the carbonaceous chondrite parent bodies (section 3.3.5 in this study, Amelin et al., 2019), this meteorite allows us to obtain the information from the outer solar system. Thus, NWA 6704 is of vital importance in that it enables us to take the first step in evaluating the distribution of ^{92}Nb between the inner and outer solar system.

4. 2. Methods

4. 2. 1. Sample digestion

We prepared mineral fractions and whole rock fractions from five fragments of NWA 6704 (Table 14: two ~50 mg fractions of whole rock from fragment #6 that is the same fragment as the #6 in the petrologic study in section 3.2.1, two 40–50 mg fractions of orthopyroxene and two ~4 mg fractions of chromite from a new fragment #7, one ~30 mg fraction of orthopyroxene and one ~3 mg fraction of chromite from a new fragment #8, one 50 mg fraction of orthopyroxene, two ~4 mg fractions of chromite, and one ~165 mg fraction of metal from a new fragment #9, and one ~7 mg fraction of chromite from a new fragment #10). All fragments (#7–#10: 2.4–12.3 g) except for #6 (already crushed into fine powders for solution-based bulk chemistry in petrologic study) were crushed into medium-grain size using an agate mortar and pestle. All non-magnetic mineral fractions were hand-picked under a stereoscopic microscope, and the metal fraction was separated using a neodymium hand magnet from a disaggregated specimens of NWA 6704.

All non-magnetic sample aliquots were digested with a mixture of ~1.2 mL of concentrated HF and ~0.9 ml of concentrated HNO_3 in a *Parr*® bomb at 190 ˚C for >65 hours. All acids used in this study are ultrapure grade reagents from Kanto Chemical CO. Inc., Japan. Once digested, the HF–HNO_3 mixtures were evaporated to dryness. The sample aliquots were then digested with ~0.9 ml of concentrated HNO_3 in a *Parr*®

bomb at 160 ˚C for >12 hours, and again, were evaporated to dryness. This step was repeated one more time. Finally, the samples were dissolved with 2 mL of 6 mol l^{-1} HCl in a *Parr*® bomb at 140 ˚C for 1 day. These procedures ensured complete digestion of all minerals, and no residues were recognizable in the vials.

For the digestion of metal fraction, we modified the method of Cook et al. (2008). Metal grains were digested in Teflon® vials by treatment with reverse aqua regia (2:1 concentrated HNO_3 to concentrated HCl) at 130 ˚C for 1 day, and then evaporated to dryness. Then, the sample was treated with 6 mol l^{-1} HCl + 1 mol l^{-1} HF at 140°C for 1 day and again evaporated to dryness. The sample was then treated with 0.5 mol l^{-1} HCl + 0.5 mol l^{-1} HF at 130 ˚C for 1 day, evaporated to dryness. This step was repeated one more time. Finally, the sample was re-dissolved in ~2 ml of 6 mol l^{-1} HCl heated on a hotplate at 140 ˚C for 1 day.

The digested solutions of Whole rock #6–1, Orthopyroxene #7–1 and #8, and Chromite #7–1,–2, and #8 were each split into two aliquots, 1.5% for Nb/Zr elemental ratio measurements and the remaining for chemical separation of Zr. The other digested solutions were each split into two aliquots, 10% for Nb/Zr elemental ratio measurements and the remaining for chemical separation of Zr.

Table 14: Summary of rock fragments of NWA 6704 for Nb-Zr dating

Speciman (#6~10)	**#6**	**#7**	**#8**	**#9**	**#10**
used sample size (mg)	42.9	7850	2400	12300	11200
Whole rock	2 fractions (6–1, –2)	–	–	–	–
Orthopyroxene	–	2 fractions (7–1, –2)	1 fraction	1 fraction	–
Chromite	–	2 fractions (7–1, –2)	1 fraction	2 fractions (9–1, –2)	1 fraction
Metal	–	–	–	1 fraction	–

4. 2. 2. Chemical separation

The purification of Zr was required to avoid matrix effects and isobaric interferences of Mo (^{92}Mo, ^{94}Mo, and ^{96}Mo), and Ru (^{96}Ru) during the measurements. Table 15 summarizes potential interferences in Zr isotope analysis. It should also be noted that major elements (Ca, Ti, Cr, Fe, and V) whose argides or dimers interfere with Zr ion signals during MC-ICP-MS analysis. Hence, these elements must be efficiently separated using column chromatography.

Our samples were processed through a two-step with additional one- or two- step ion-exchange procedure modified from Münker et al. (2001) and Iizuka et al. (2016) (Table 16). The two step ion-exchange procedure comprised (i) Fe removal using AG1-X8 anion exchange resin (200–400 mesh), and (ii) Zr separation using Ln-Spec resin (100–150 μm). All acids used in the chemical separation are ultrapure grade reagents from Kanto Chemical CO. Inc., Japan.

Column 1

In the first step, Fe was removed from most elements including Zr using anion exchange chromatography. Two ml of Bio-Rad AG1-X8 resin (200–400 mesh) was packed in a medium-sized polypropylene column purchased from Muromachi Chemical Inc., Japan (d = ~6.5 mm, h = 54 mm). The resin was washed by passing 2 mol l^{-1} HF, 0.5 mol l^{-1} HNO_3, and 6 mol l^{-1} HCl. After conditioning the resin using 5 ml of 6 mol l^{-1} HCl, samples dissolved in 2 ml of 6 mol l^{-1} HCl were loaded onto the column.

Before loading, sample solutions were heated on a hotplate at 140 ˚C for 1 day. The fraction containing Zr, which began to be eluted immediately, was collected by passing an additional 4 ml of 6 mol l^{-1} HCl.

After Fe removal, the Zr fraction in ~6 ml of 6 mol l^{-1} HCl was evaporated slowly until the total volume became ~1 ml. Subsequently, the sample aliquots were converted to a total volume of 3 ml of 2 mol l^{-1} HCl solution by dilution with H_2O, and then heated on a hotplate at 100 °C for 1 day. Before column loading, the sample was cooled down at room temperature.

Column 2

In the second step, Zr was purified from the matrix elements. Eichrom Ln-spec resin (100–150 μm) was packed in a Savillex PFA microcolumn (d = ~2.4 mm, h = 20 cm). After conditioning the resin using 0.5 ml of 2 mol l^{-1} HNO_3 + 1–1.1 wt% H_2O_2 solution, samples dissolved in ~3 ml of 2 mol l^{-1} HCl solution were loaded onto the column. Then, matrix elements including Ca, Ti, Cr, residual-Fe, V, Mo and Ru were eluted in 30.5 ml of 2 mol l^{-1} HNO_3 + 1–1.1 wt% H_2O_2 solution, followed by elution of REE in 1 ml of 0.5 mol l^{-1} HNO_3, 5 ml of 3 mol l^{-1} HCl, 5 ml of 6 mol l^{-1} HCl, 1 ml of 0.5 mol l^{-1} HNO_3, and 1–2 ml of 0.5 mol l^{-1} HCl + 0.06 mol l^{-1} HF. For all steps using H_2O_2, H_2O_2 was mixed with HNO_3 1 hour before the loading. This is because H_2O_2 dissociates into H_2O and O_2 with time, whereas the addition of H_2O_2 to 12 mol l^{-1} HNO_3 immediately before the loading can cause insufficient reaction

between H_2O_2 and HNO_3 (Yang et al. 2015). Finally, Zr was collected with 16 ml of 0.5 mol l^{-1} HCl + 0.06 mol l^{-1} HF.

Since remaining traces of Fe, Ti, Cr, Mo and/or Ru in the sample require significant interference corrections on Zr isotope ratio measurements, some samples were passed through additional column chemistry identical to the first Fe removal step and the second Zr separation step, but using smaller resin volumes of ~0.5 ml and 1 ml, respectively (Table 16). Each sample was monitored prior to analysis by MC-ICP-MS for Zr concentrations and samples containing Fe, Cr, or Ti at a level of 10% of Zr concentration were re-processed through the Fe and/or Zr separation step. After Zr separation step, the Zr fraction in ~16 ml of 0.5 mol l^{-1} HCl + 0.06 mol l^{-1} HF was evaporated slowly at about 150 ˚C until the solution formed ~10 μl-sized droplet at the bottom of vial. The sample was not completely dried, because the solid-state Zr fractions can be difficult to re-dissolve in dilute acid. This associates with the low recovery yield of Zr during the whole chemical separation procedure. Thus, when changing the sample acid solvent for the next additional separation step, we must take care not to evaporate samples completely. After the droplet was formed, the conc. HCl (ultrapure grade reagents from Kanto Chemical CO. Inc., Japan) was added and evaporated slowly until the solution formed ~10 μl-sized droplet again at the bottom of vial, and gradually change the solvent to only HCl. This step was repeated again, and finally converted to a total volume of 0.2 ml of 6 mol l^{-1} HCl solution by dilution with H_2O for the additional Fe separation step. If the samples were processed

through only additional Zr separation step, the solution was converted to 0.2 ml of 2 mol l^{-1} HCl solution by dilution with H_2O.

Prior to analysis using MC-ICP-MS, the organic matter was decomposed. After Zr separation step, the Zr fraction in 0.5 mol l^{-1} HCl + 0.06 mol l^{-1} HF was evaporated at about 150 ˚C for more than 7 hours to dryness. Then about 0.5 ml of concentrated HF, HNO_3 and $HClO_4$ in a volume ratio of 1 : 10 : 5 were added, and the mixtures were heated on a hotplate to dryness. In this evaporation step, the temperature was increased from 80 ˚C to 180 ˚C in 10–20 ˚C steps (about 40 minutes for each step). Then, the sample was heated at 215 ˚C for more than 2 hours to evaporate $HClO_4$ completely. Subsequently, about 0.5 ml of concentrated HF, concentrated HNO_3 and H_2O in a volume ratio of 1 : 10 : 5 were added, and heated on a hotplate at 130 ˚C for 1 night then evaporated to dryness. In this evaporation step, the hotplate temperature was increased from 80 ˚C to 130 ˚C in 10 ˚C steps (about 15 minutes for each step). Again, caution was taken not to evaporate sample to completely dry, and the sample was evaporated until the solution formed ~10 μl-sized droplet at the bottom of vial. After the droplet was formed, the conc. HNO_3 was added and evaporated slowly until the solution formed ~10 μl-sized droplet again at the bottom of vial, gradually decomposing fluorides and changing the solvent to only HNO_3. This step was repeated again, and finally converted to a 0.5 mol l^{-1} HNO_3 + trace HF solution containing ~10 ppb of Zr by dilution with H_2O. The sample was heated on a hotplate at 130 ˚C for 1 day, for the analysis using MC-ICP-MS.

Total procedural blanks of the whole procedure were ~20–40 pg of Zr, or 800

pg–1300 pg of Zr if a Parr® bomb was used, and is inconsequential considering the size of the samples (> 100 ng for whole rock, metal and orthopyroxene).

Table 15:
Possible interferences in Zr isotope measurements

Mass	**90**	**91**	**92**	**94**	**96**
Single charged ion	$^{90}Zr^+$	$^{91}Zr^+$	$^{92}Zr^+$	$^{94}Zr^+$	$^{96}Zr^+$
			$^{92}Mo^+$	$^{94}Mo^+$	$^{96}Mo^+$
					$^{96}Ru^+$
Doubly-charged ion	$^{180}Hf^{++}$				
	$^{180}Ta^{++}$				
	$^{180}W^{++}$	$^{182}W^{++}$	$^{184}W^{++}$		
			$^{184}Os^{++}$	$^{188}Os^{++}$	$^{192}Os^{++}$
					$^{192}Pt^{++}$
Polyatomic ion	$^{45}Sc^{45}Sc^+$		$^{46}Ca^{46}Ca^+$, $^{46}Ti^{46}Ti^+$	$^{47}Ti^{47}Ti^+$	$^{48}Ca^{48}Ca^+$, $^{48}Ti^{48}Ti^+$
(Dimer, Argides, Oxide, Carbides, Chlorides)	$^{40}Ar^{50}Ti^+$, $^{40}Ar^{50}V^+$	$^{40}Ar^{51}V^+$	$^{40}Ar^{52}Cr^+$	$^{40}Ar^{54}Cr^+$, $^{40}Ar^{54}Fe^+$	$^{40}Ar^{56}Fe^+$
	$^{40}Ar^{50}Cr^+$				
	$^{74}Ge^{16}O^+$, $^{74}Se^{16}O^+$	$^{75}As^{16}O^+$	$^{76}Ge^{16}O^+$, $^{76}Se^{16}O^+$	$^{78}Se^{16}O^+$, $^{78}Kr^{16}O^+$	$^{80}Se^{16}O^+$, $^{80}Kr^{16}O^+$
	$^{78}Se^{12}C^+$, $^{78}Kr^{12}C^+$	$^{79}Br^{12}C^+$	$^{80}Se^{12}C^+$, $^{80}Kr^{12}C^+$	$^{82}Se^{12}C^+$, $^{82}Kr^{12}C^+$	$^{84}Kr^{12}C^+$, $^{84}Sr^{12}C^+$
	$^{35}Cl^{55}Mn^+$, $^{37}Cl^{53}Cr^+$	$^{35}Cl^{56}Fe^+$, $^{37}Cl^{54}Cr^+$	$^{35}Cl^{57}Fe^+$, $^{37}Cl^{55}Mn^+$	$^{35}Cl^{59}Co^+$, $^{37}Cl^{57}Fe^+$	$^{35}Cl^{61}Ni^+$, $^{37}Cl^{59}Co^+$

Table 16:
Zirconium column chromatography

Step	Volume (mL)	Acid
Column 1 (2mL AG1-X8 anion resin 200-400 mesh d=~6.5 mm, h=54 mm)		
Wash	10	2 $molL^{-1}$ HF
	10	0.5 $molL^{-1}$ HNO_3
	2	6 $molL^{-1}$ HCl
Precondition	5	6 $molL^{-1}$ HCl
Load	2	6 $molL^{-1}$ HCl
Elute Zr	4	6 $molL^{-1}$ HCl
Column 2 (2.5mL Ln-Spec resin 100-150 micron d=~2.4 mm, h=20 cm)		
Wash	6	2 $molL^{-1}$ HF
	6	6 $molL^{-1}$ HCl
	3	3 $molL^{-1}$ HNO_3
Precondition	0.5	2 $molL^{-1}$ HNO_3 - 1wt % H_2O_2
Load	3	2 $molL^{-1}$ HCl
	30.5	2 $molL^{-1}$ HNO_3 - 1wt % H_2O_2
	1	0.5 $molL^{-1}$ HNO_3
	5	3 $molL^{-1}$ HCl
	5	6 molL–1 HCl
	1	0.5 $molL^{-1}$ HNO_3
	2	0.5 $molL^{-1}$ HCl - 0.06$molL^{-1}$ HF
Elute Zr	16	0.5 $molL^{-1}$ HCl - 0.06$molL^{-1}$ HF
Additional 1 (0.5mL AG50W-X8 cation resin 200-400 mesh d=~2 mm, h=30 mm)		
Wash	1	2 $molL^{-1}$ HF
	1	0.5 $molL^{-1}$ HNO_3
	1	6 $molL^{-1}$ HCl
Precondition	5	6 $molL^{-1}$ HCl
Load	0.2	6 $molL^{-1}$ HCl
Elute Zr	1.5	6 $molL^{-1}$ HCl
Additional 2 (0.5mL Ln-Spec resin 100-150 micron d=~2 mm, h=30 mm)		
Wash	1	2 $molL^{-1}$ HF
	1	6 $molL^{-1}$ HCl
	0.5	3 $molL^{-1}$ HNO_3
Precondition	0.5	2 $molL^{-1}$ HNO_3 - 1wt % H_2O_2
Load	0.2	2 $molL^{-1}$ HCl
	6	2 $molL^{-1}$ HNO_3 - 1wt % H_2O_2
	0.1	0.5 $molL^{-1}$ HNO_3
	0.5	3 $molL^{-1}$ HCl
	1	6 $molL^{-1}$ HCl
	0.1	0.5 $molL^{-1}$ HNO_3
Elute Zr	4	0.5 $molL^{-1}$ HCl - 0.06$molL^{-1}$ HF

4. 2. 3. Nb/Zr ratio measurement by solution-ICP-MS

The Nb/Zr ratios of the digested solutions of Whole rock #6–1, Orthopyroxene #7–1 and #8, and Chromite #7–1,–2, and #8 were obtained using a *Thermo Fisher Scientific*^{TM} *iCAP Q*^{TM} ICP–MS interfaced to a *Cetac Aridus II* desolvating nebulizer at the University of Tokyo without chemical separation. The samples were typically measured with ~0.5 ppb of Zr concentration.

The Nb/Zr ratios of the other solutions were obtained using the *Thermo Fisher Scientific*^{TM} *iCAP Q*^{TM} ICP–MS with a spray chamber at the University of Tokyo without chemical separation. The samples were typically measured with ~4–5 ppb of Zr concentration. Repeated sample measurements yielded analytical uncertainties (2 standard deviation) of ± 0.04–0.09 for $^{93}Nb/^{90}Zr$ (Table 17).

4. 2. 4. Zr isotope measurement by MC-ICP-MS

The Zr isotopic compositions were measured using a *Thermo Fisher Scientific Neptune Plus* MC-ICP-MS interfaced to the *Cetac Aridus II* desolvating nebulizer at the University of Tokyo. The measurements were conducted using a Jet sample cone and a skimmer H-cone in the low-resolution mode, which resulted in a typical sensitivity for Zr of 0.35–0.5 V•ppb^{-1} (10^{11} Ω resistor). Data were acquired with static mode on Faraday cups to monitor species $^{90}Zr^+$, $^{91}Zr^+$, $^{92}Zr^+$, $^{94}Zr^+$, $^{95}Mo^+$, $^{96}Zr^+$ and $^{99}Ru^+$ with

integration time per cycle of 8.4 seconds. Each measurement comprised 60 cycles. Instrumental mass fractionation was corrected relative to $^{94}Zr/^{90}Zr = 0.3381$ (Minster and Allègre, 1982), and the interferences of $^{92,94}Mo$ on $^{92,94}Zr$ and ^{96}Mo and ^{96}Ru on ^{96}Zr were corrected following the protocol of Schönbächler et al. (2004). The interference correction yielded accurate results for Mo-, Fe-, Cr-, Ti- doped synthetic 10 ppb Zr standard solutions with ratios of Mo/Zr of up to 0.004 (Fig. 32), Fe/Zr of up to 0.8, Cr/Zr of up to 0.1, and Ti/Zr of up to 0.3. All Zr isotope ratios of samples are expressed as the epsilon (ε) notation relative deviation from the National Institute Standards and Technology Standard Reference Material 3169 standard as follows;

$$\varepsilon^{91,\,92,\,\text{or}\,96}Zr = 10^4 \times [(^{91,\,92,\,\text{or}\,96}Zr/^{90}Zr)_{sample} / (^{91,\,92,\,\text{or}\,96}Zr/^{90}Zr)_{NIST3169} - 1] \qquad \text{(vii)}$$

We obtained the analytical uncertainties (2 standard deviation) of ± 0.2–0.5 ε for $\varepsilon^{91}Zr$, ± 0.2–0.4 ε for $\varepsilon^{92}Zr$, and ± 0.5–0.7 ε for $\varepsilon^{96}Zr$ with only 10 ng of Zr (Table 17).

4. 3. Results

As shown in the Fig. 33a-d, there is no correlation between measured Zr isotopes and $^{95}Mo/^{90}Zr$ and $^{99}Ru/^{90}Zr$. These indicate that the Zr isotope excesses are not artifacts of either $^{92,\,96}Mo$ interferences or ^{96}Ru interference. Also, our ion-exchange procedure ensures a good separation of Zr from the major spectral interferences. All of the sample

solutions after purification had Mo/Zr, Ru/Zr, Fe/Zr, Cr/Zr, and Ti/Zr that are always less than 0.002, 1.0×10^{-4}, 0.05, 0.01, and 0.01, respectively. The ratios are much smaller than the accurate correction limits (e.g., Fig. 32).

All Zr isotopic data are presented together with the $^{93}Nb/^{90}Zr$ ratios in Table 17. The $\varepsilon^{91}Zr$ and $\varepsilon^{96}Zr$ values of the whole rock and all mineral fractions of NWA 6704 overlap within analytical uncertainty, with average values of $\varepsilon^{91}Zr = 0.01 \pm 0.19$ (2 S.D.), and $\varepsilon^{96}Zr = 1.54 \pm 0.84$ (2 S.D.), respectively. The Zr isotope data including four orthopyroxene fractions and one metal fraction and the two whole rock data for NWA 6704 are all identical with the value obtained for a standard solution of NIST-SRM 3169 Zr within analytical uncertainty. In contrast, six chromite fractions with high $^{93}Nb/^{90}Zr$ yielded distinctly higher $\varepsilon^{92}Zr$ up to $+1.52 \pm 0.40$. Using the $^{93}Nb/^{90}Zr$ values obtained for eleven mineral fractions (four orthopyroxene, one metal, six chromite) and two whole rock fractions, the positive correlation line was obtained as shown in Fig. 34a. The y-intercept defines the value of -0.17 ± 0.09, and the slope of the regression line is $(2.8 \pm 0.3) \times 10^{-5}$.

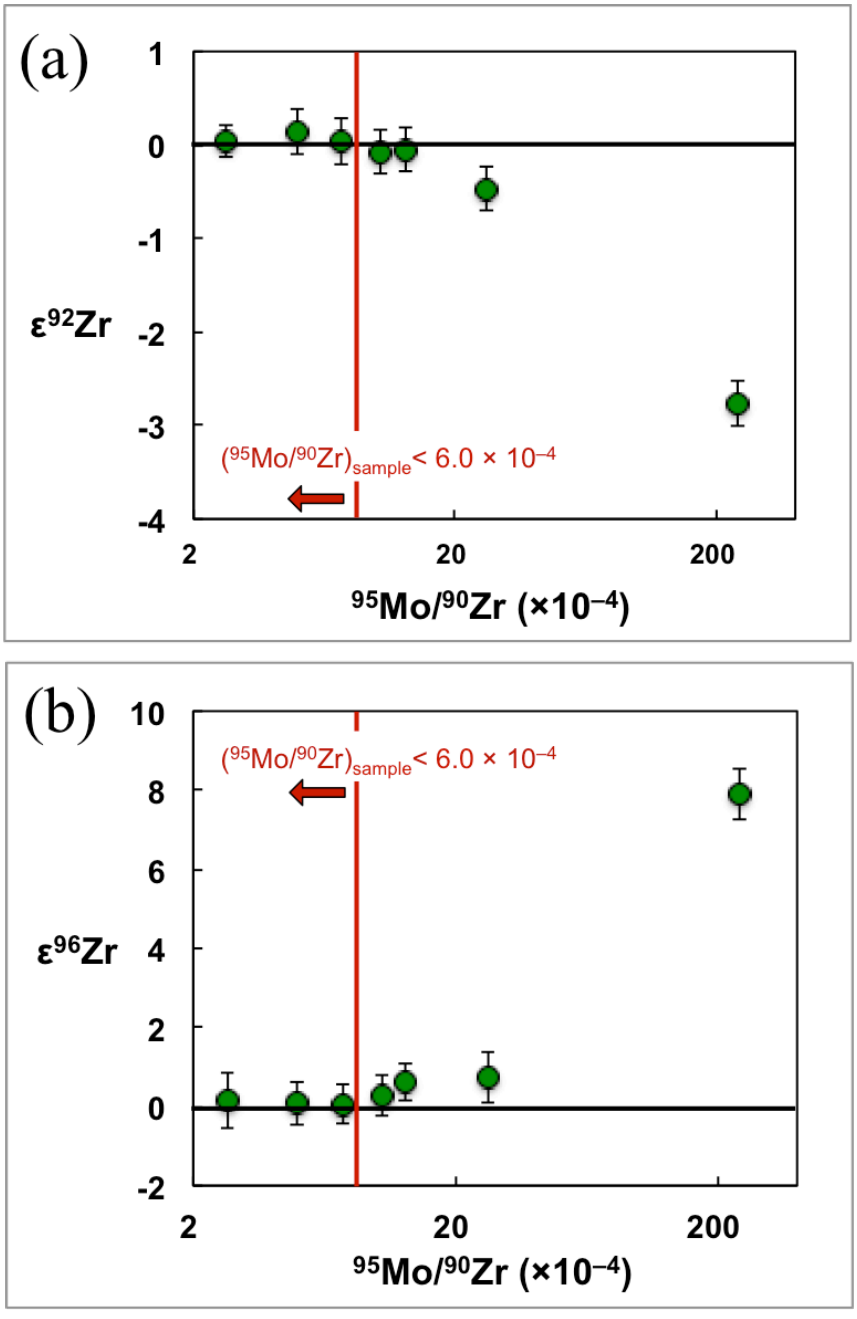

Fig. 32. (a) ε^{92}Zr and (b) ε^{96}Zr values obtained after interference corrections for Mo-doped synthetic Zr standard (10 ppb) solutions. The Mo/Zr ratios of our sample solutions after purification were much smaller than the accurate correction limits. Error bars represent 2 s.d. quoted in the Table 17.

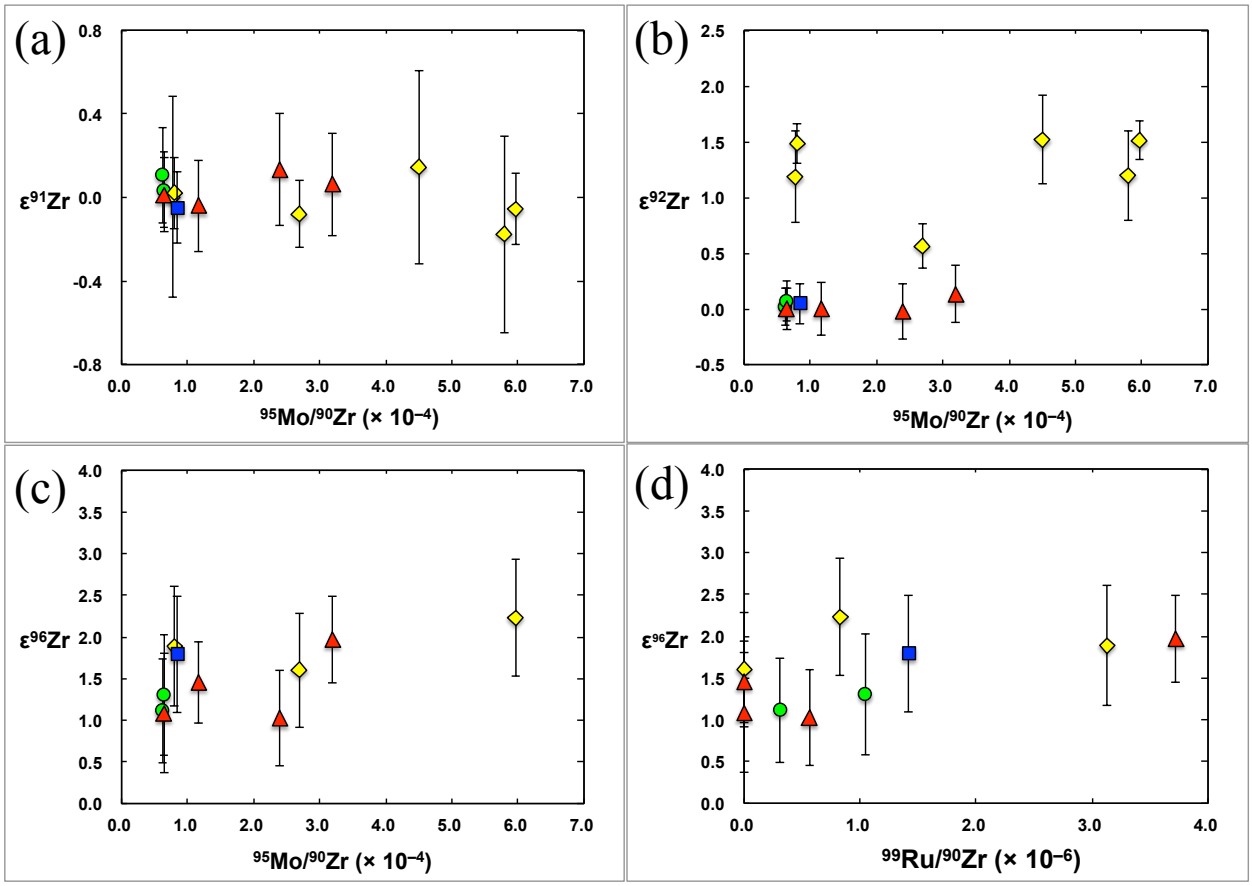

Fig. 33. (a) ε^{91}Zr vs. Mo/Zr ratios, (b) ε^{92}Zr vs. Mo/Zr ratios, (c) ε^{96}Zr vs. Mo/Zr ratios, and (c) ε^{96}Zr vs. Ru/Zr ratios obtained for whole rock fractions (green circles), orthopyroxene fractions (red triangles), chromite fractions (yellow diamonds), and metal fractions (blue square) are compared. There is no correlation observed between measured Zr isotopes and ^{95}Mo/^{90}Zr and ^{99}Ru/^{90}Zr. These indicate that the Zr isotope excesses are not artifacts of either $^{92, 96}$Mo interferences or ^{96}Ru interference. Error bars represent 2 s.d. quoted in the Table 17.

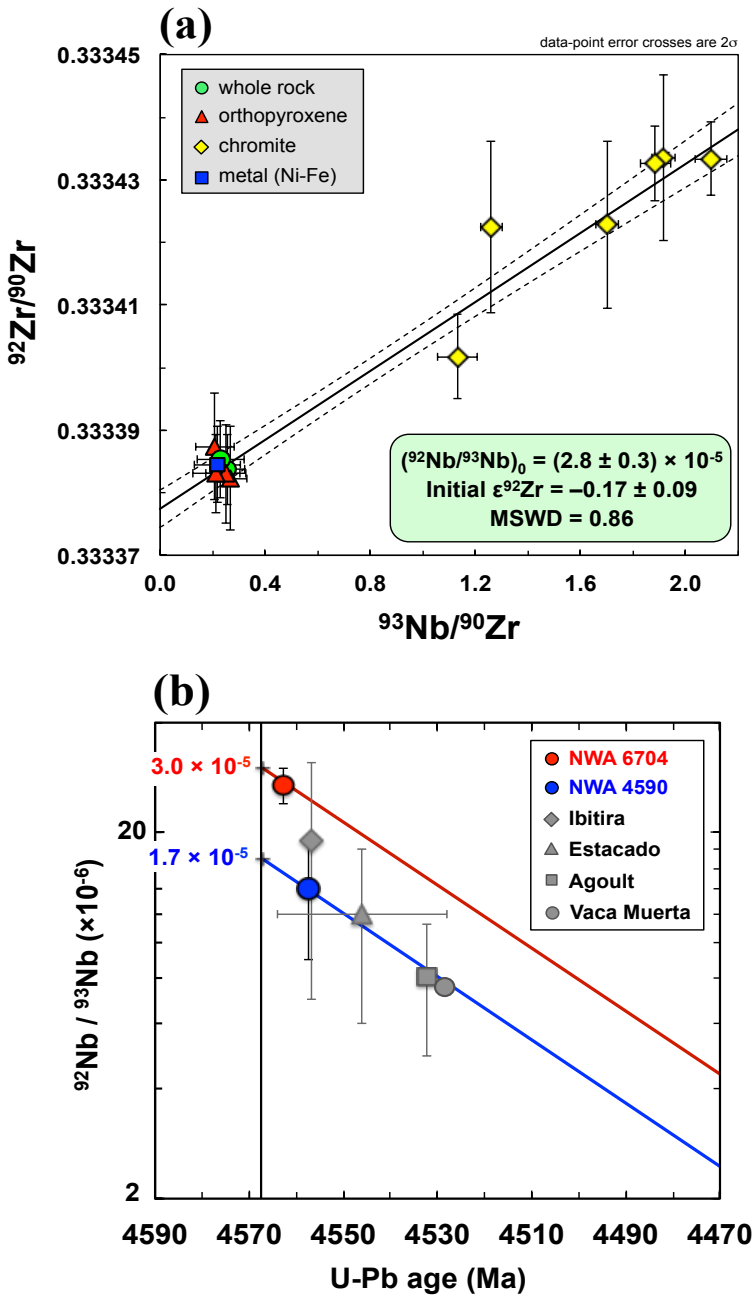

Fig. 34. (a) The $^{92}Zr/^{90}Zr$ ratio vs. $^{93}Nb/^{90}Zr$ ratio for whole rock and mineral fractions of the NWA 6704 primitive achondrite, and (b) The comparison of the initial ^{92}Nb value obtained in this study, $^{92}Nb/^{93}Nb = (3.0 \pm 0.3) \times 10^{-5}$, with the value of $^{92}Nb/^{93}Nb = (1.7 \pm 0.6) \times 10^{-5}$ in the inner solar system (Iizuka et al., 2016), All $^{92}Zr/^{90}Zr$ ratios are normalized to the reference value $^{92}Zr/^{90}Zr = 0.333383$ for the standard solutions (Rehkämper et al., 2001). The slopes and y-intercepts of the isochrons define the initial $^{92}Nb/^{93}Nb$ and $^{92}Zr/^{90}Zr$ at the time of Nb–Zr closure.

Table 17:
Nb–Zr isotopic data for NWA 6704

Sample	Weight (mg)	Zr (ppm)	$^{93}Nb/^{90}Zr \pm 2\sigma$	$\varepsilon^{91}Zr \pm 2\sigma$	$\varepsilon^{92}Zr \pm 2\sigma$	$\varepsilon^{96}Zr \pm 2\sigma$	$^{95}Mo/^{90}Zr$ ($\times 10^{-4}$)	$^{99}Ru/^{90}Zr$ ($\times 10^{-6}$)
NWA 6704								
Whole rock #6-1	48.3	3.8	0.25 ± 0.068	0.11 ± 0.23	0.02 ± 0.17	1.11 ± 0.62	0.6	0.3
Whole rock #6-2	49.5	3.5	0.23 ± 0.089	0.04 ± 0.18	0.07 ± 0.18	1.30 ± 0.72	0.6	1.0
Orthopyroxene #7-1	40.6	3.4	0.27 ± 0.062	0.13 ± 0.27	–0.02 ± 0.25	1.02 ± 0.57	2.4	0.6
Orthopyroxene #7-2	48.9	3.1	0.21 ± 0.089	0.01 ± 0.18	0.00 ± 0.19	1.08 ± 0.71	0.6	0.0
Orthopyroxene #8	27.7	4.2	0.21 ± 0.073	0.06 ± 0.25	0.13 ± 0.25	1.97 ± 0.52	3.2	3.7
Orthopyroxene #9	49.1	3.4	0.25 ± 0.075	–0.04 ± 0.22	0.00 ± 0.24	1.45 ± 0.49	1.2	0.0
Chromite #7-1	4.1	14.6	1.26 ± 0.042	0.00 ± 0.48	1.18 ± 0.41			
Chromite #7-2	3.8	11.9	1.70 ± 0.042	–0.18 ± 0.47	1.20 ± 0.40			
Chromite #8	2.9	17.8	1.92 ± 0.045	0.15 ± 0.46	1.52 ± 0.40			
Chromite #9-1	7.6	15.2	1.88 ± 0.059	0.02 ± 0.17	1.49 ± 0.18	1.89 ± 0.72	0.8	3.1
Chromite #9-2	6.5	15.5	2.10 ± 0.061	–0.06 ± 0.17	1.51 ± 0.17	2.23 ± 0.70	6.0	0.8
Chromite #10	6.5	8.0	1.13 ± 0.076	–0.08 ± 0.16	0.56 ± 0.20	1.60 ± 0.69	2.7	0.0
Metal #9	165	2.2	0.22 ± 0.087	–0.05 ± 0.17	0.05 ± 0.18	1.79 ± 0.70	0.8	1.4

4. 4. Discussion

4. 4. 1. The initial abundance of ^{92}Nb in the outer solar system

The correspondence of ε^{96}Zr between the whole rock and mineral fractions ensures that all mineral fractions are co-genetic (i.e., not a foreign xenocryst inherited from impactor materials). This is consistent with the results of petrologic interpretations in Chapter 3. Like other stable isotopes stated in above (Δ^{17}O, ε^{54}Cr, and ε^{50}Ti), planetary-scale distinctive mass independent isotope variations in carbonaceous chondrites relative to other meteorites have also been observed in ε^{96}Zr (Harper et al., 1991; Schönbächler et al., 2003, 2004, 2005; Akram et al., 2013, 2015). The ε^{91}Zr and ε^{96}Zr values of NWA 6704 (ε^{91}Zr = 0.01 ± 0.19; ε^{96}Zr = 1.54 ± 0.84; Table 17) are plotted within the range of carbonaceous chondrites (Akram et al., 2015). More specifically, the ε^{96}Zr value of NWA 6704 overlaps with the range of ε^{96}Zr of metal-rich CR/CB and CV, CM, CO chondrites, and distinctively higher than those of CK and CI chondrites.

What the regression line of Fig. 34a means is a matter of critical importance in this study. A recent ^{92}Nb study of Group II CAI (Lai et al. 2017) found a weak correlation between ^{93}Nb/^{90}Zr and ^{92}Zr/^{90}Zr. The slope of the regression line corresponds to the value of ^{92}Nb/^{93}Nb = (3.7 ± 0.6) × 10^{-5} at the time of solar system formation. They interpreted the Nb–Zr data of CAI as as a mixing line, reflecting the preserved local signature of "presolar *p*-process enriched dust". This interpretation is

based on a weak linear correlation observed between ε^{92}Zr and 1/Zr (Lai et al. 2017). On the other hand, our results show no linear trend between ε^{92}Zr and 1/Zr (Fig. 35a), demonstrating that the regression line (Fig. 34a) is not a mixing line. Fig. 35b compares the Nb concentrations and ^{93}Nb/^{90}Zr variations in individual chromite grains from fractions #6–10 obtained by LA-ICPMS. The figure shows that the Nb concentrations in chromite grains systematically differ among the meteorite fractions, and the average concentrations are positively correlated with the average ^{93}Nb/^{90}Zr values. Moreover, ^{93}Nb/^{90}Zr in these chromite grains covers the range of ^{93}Nb/^{90}Zr obtained from chromite fractions for Nb-Zr isochron dating (Fig. 34a). These lines of evidence indicate that the ^{93}Nb/^{90}Zr variations of chromite fractions in the regression line reflect the heterogeneity in the Nb concentrations originally existed at the time of crystallization. Note also that the spallation effect on ^{92}Zr is too small to generate significant variations in the calculated slope, i.e., the initial ^{92}Nb/^{93}Nb ratio (Leya et al., 2001). Consequently, we conclude that the obtained trend (Fig. 34a) is an isochron rather than a mixing line, and the observed ^{92}Zr excesses are due to the radioactive decay of ^{92}Nb. Thus, the y-intercept in Fig. 34b defines an initial ε^{92}Zr of –0.17 ± 0.09, and the slope of the regression line defines an initial ^{92}Nb/^{93}Nb of (2.8 ± 0.3) × 10^{-5} at the time of NWA 6704 formation. By combining this value with the U–Pb age of NWA 6704 (4562.76 ± 0.30 Ma; Amelin et al., 2019), an initial ^{92}Nb/^{93}Nb of (3.0 ± 0.3) × 10^{-5} at the time of solar system formation can be derived (Fig. 34b).

Since all five stable isotopes of Zr ($^{90, 91, 92, 94, 96}$Zr) show distinct contributions from *s*- and *r*-process nuclides (e.g., Bisterzo et al. 2014), the nucleosynthetic

contributions to the analysis of Zr isotopes should be considered here. Among the Zr isotopes, ^{90}Zr (39.7%) and ^{96}Zr (61.3%) have higher contributions from *r*-process relative to the other Zr isotopes (^{91}Zr: 28.8%; ^{92}Zr: 31.8%; ^{94}Zr: 16.7%; after Bisterzo et al. 2014). Considering that the ^{96}Zr/^{90}Zr raios of whole rock and mineral fractions of NWA 6704 yielded positive anomalies (Table 17), the different degrees of nucleosynthetic contributions to the Zr isotopes might affect the results of Nb-Zr internal isochron dating. Here, we tentatively assume that all of the ^{96}Zr positive anomalies (Table 17) were solely caused by a nucleosynthetic shift in ^{94}Zr/^{90}Zr ratio that is used for the mass bias correction (reference value = 0.3381; Minster and Allègre, 1982). In this case, all of the ^{96}Zr positive anomalies in NWA 6704 can be explained by a nucleosynthetic shift of ^{94}Zr/^{90}Zr to 0.338065. This shift lowers the resultant ε^{92}Zr by –0.52 ε. Note, however, that the changes of ε^{92}Zr are identical among all the analyzed fractions, and that the slope of isochron obtained in this study should not be altered (Fig. 34a). Moreover, the y-intercept of the isochron that defines the initial ε^{92}Zr of –0.17 ± 0.09 at the time of NWA 6704 formation is identical to the value of inner solar system (Iizuka et al. 2016) within analytical uncertainty. Furthermore, ε^{91}Zr values obtained in this study are also identical to those of the standard within analytical uncertainty. These results indicate that the different degrees of nucleosynthetic contributions are significant only for ^{96}Zr in Zr isotopes and also that the initial abundance of ^{92}Nb as well as initial ^{92}Zr/^{90}Zr obtained in this study is valid.

The obtained initial ^{92}Nb/^{93}Nb value of $(3.0 \pm 0.3) \times 10^{-5}$ at the time of solar system formation is distinctly higher than the initial value in the inner solar system of

$(1.7 \pm 0.6) \times 10^{-5}$ (Iizuka et al. 2016) (Fig. 34b). The isotopic anomalies of $\Delta^{17}O$, $\varepsilon^{54}Cr$, $\varepsilon^{50}Ti$ (section 3.3.5.), $\varepsilon^{84}Sr$ (Amelin et al., 2019), and $\varepsilon^{96}Zr$ in NWA 6704 suggest that its parent body sampled the same reservoirs as the carbonaceous chondrite parent bodies. Thus, the initial $^{92}Nb/^{93}Nb$ value of $(3.0 \pm 0.3) \times 10^{-5}$ can be considered to record the information of the outer solar system. This finding indicates that ^{92}Nb was heterogeneously distributed in the protoplanetary disk before the formation of NWA 6704 (4562.76 ± 0.30 Ma; Amelin et al., 2019), and was relatively enriched in the outer solar system. The difference between these two values of $(1.7 \pm 0.6) \times 10^{-5}$ and $(3.0 \pm 0.3) \times 10^{-5}$ corresponds to the age shift of up to 30 Myr, which seriously affects the interpretation of the Nb-Zr early solar system chronology. We therefore conclude that the canonical initial $^{92}Nb/^{93}Nb$ value of $(1.7 \pm 0.6) \times 10^{-5}$ should not be used for Nb-Zr dating of materials originated from the outer solar system. Owing to the precisely determined initial $^{92}Nb/^{93}Nb = (3.0 \pm 0.3) \times 10^{-5}$ (relative uncertainty: 10%) from this study together with its rapid closure of isotopic systems indicated from the thermal history (Chapter 3), NWA 6704 would serve as the most reliable *Time anchor* for the Nb-Zr chronometry in the accretion region of carbonaceous chondrite parent bodies at this time. Yet, it is obvious that the homogeneity of ^{92}Nb distribution within the outer solar system needs to be further evaluated by establishing other reliable *Time anchors*.

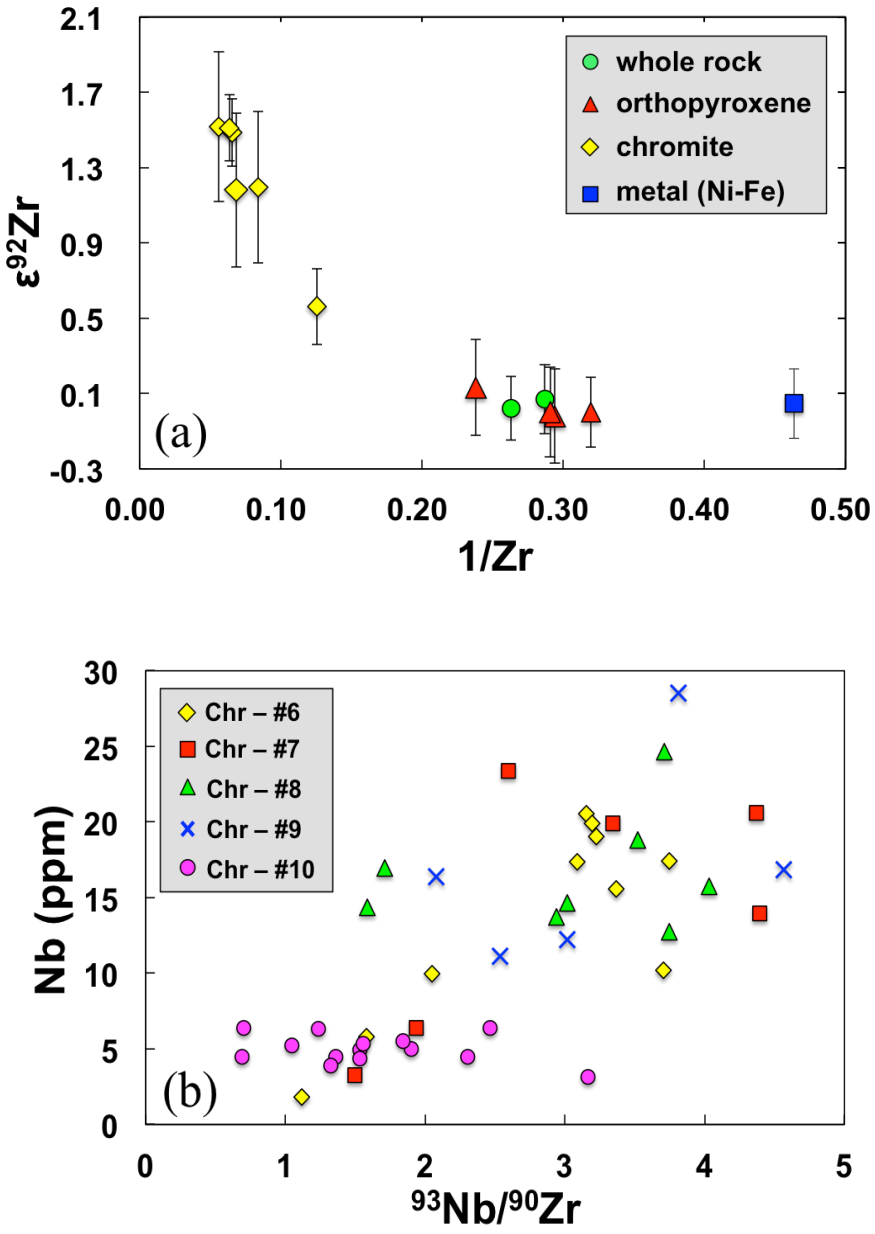

Fig. 35. (a) $\varepsilon^{92}Zr$ vs. 1/Zr for for whole rock and mineral fractions of NWA 6704 primitive achondrite. Error bars represent 2 s.d. quoted in the Table 17. (b) Nb concentrations vs. $^{93}Nb/^{90}Zr$ ratios in respective chromite grains from fractions #6–10 obtained by LA-ICPMS.

4. 4. 2. The nucleosynthetic origin of ^{92}Nb

A few tens of nuclei located on the proton-rich side of the valley of *β*-stability, the so-called "*p*-process nuclei" cannot be produced by neutron captures, and typically one to two orders of magnitude less than the *s*- and *r*- process isotopes of the same elements. The *p*-process nuclides might be, therefore, sensitive monitors for the distribution of supernova material, and the initial abundance of them deduced from meteorites (i.e., *Time anchors*), are expected to place constraints on the origin of nucleosynthetic isotope variations in the early solar system. The origin of "*p*-process nuclei" has been studied for more than 50 years since the pioneering works by Cameron (1957) and Burbidge et al. (1957), and they suggested *p*-process nuclei were produced by a combination of proton addition reaction (*p, γ*) or photodisintegration reaction (*γ, n*) occurring on previously existing *s*- and *r*- process seed nuclei in a proton-rich environment. Since then, several different types of processes and astrophysical sites have been proposed for the origin of "*p*-nuclei", including *γ*-process, *α*-process, *rp*-process, *νp*-process, and *ν*-process.

The *γ*-process was first suggested by Woosley and Howard (1978), which comprises the combination of photodisintegration reactions, and (*γ, n*), (*γ, p*) or (*γ, α*). It occurs in the O-Ne-rich zone of core-collapse massive star during Type II supernova (hereafter, SNII) as the possible mechanism for the origin of *p*-nuclei. It also has been suggested that the Type Ia supernovae (hereafter, SNeIa) derived from the thermonuclear explosion of a white dwarf above the Chandrasekhar limit was the

possible site of the γ-process (Travaglio et al., 2014).

The α-process, so-called α-rich freezeout, is the charged particle reactions occurred during the freezeout of material from nuclear statistical equilibrium (NSE) at high temperature and contains a large fraction of α-particles. When the material expanded and cooled so rapidly that not all α-particles have time to reassemble, α-, proton- neutron- captures and their reverse reactions can occur. The possible site for α-process is in a SNII (Woosley and Howard, 1992; Hoffman et al., 1996; Meyer, 2003).

The *rp*-process is a sequential reaction of successive proton capture followed by β^+ decay (Rauscher et al., 2013). It is expected to take place in X-ray bursts (Schatz et al., 1998, Dauphas et al., 2003). During the process, the proton capture reaction rates are orders of magnitude faster than the competing β^+ decays.

The *vp*-process and *v*-process are the direct interactions of neutrino matter occurring on the two different sites in SNeII. The *vp*-process is the proton capture, which occurs in the neutrino driven winds (matter outflows coming from near the neutron star that are driven outwards by neutrino matter interaction) emitted by the neutron star formed during SNII (Wanajo, 2006). This process takes place in the innermost layers of SNII. The nuclei having equal neutron and proton numbers act as seeds, and capture protons until the β^+-half-life of a nucleus is longer than the expansion time of the winds. The *v*-process takes place in the outer layers of the star that survives the SN explosion (Woosley et al. 1990; Heger et al. 2005; Byelikov et al., 2007; Cheoun et al., 2012). As neutrinos pass through the star, neutrinos can interact via

charged-current (CC; mediated by either the W^+ or the W^- boson) or neutral current (NC; mediated by the charge zero Z_0 boson) interactions with the atomic nuclei in the outer layers. Although various nuclides are synthesized by *v*-process, the produced abundances are usually negligibly small compared to the production by other nucleosynthetic processes (Hayakawa et al. 2013). Thus, it is expected that the *v*-process is important only for rare isotopes such as ^{138}La, ^{180}Ta, ^{92}Nb, and ^{98}Tc (Woosley et al. 1990; Heger et al. 2005; Hayakawa et al. 2013; Hayakawa et al. 2018).

The obtained initial high abundance of ^{92}Nb provides clues on the origin of the proton-rich "*p*-process" nucleosynthesis. Several processes have been proposed to account for the current initial ^{92}Nb/^{93}Nb in the early solar system, that is, the initial abundance of ^{92}Nb/^{93}Nb in the inner solar system. Among the *p*-process nucleosynthetic models described above, the *γ*-process, *rp*-process and *vp*-process in the CCSN under-propduce the observed abundance of ^{92}Nb, because it is shielded from a contribution by proton-rich progenitors during freeze-out by the stable ^{92}Mo (Rauscher et al., 2013). As a consequence, the possible candidates for the nucleosynthesis of ^{92}Nb are the photodisintegration reactions (*γ*-process) in SNIa (Travaglio et al., 2014), or the neutrino-induced reactions (*v*-process) in core-collapse SNII (Hayakawa et al., 2013). Recently, Lugaro et al. (2016) extended the study of Travaglio et al. (2014) to investigate if the initial abundances of ^{92}Nb and radionuclide ^{53}Mn can be accounted for simultaneously by one process in SNIa. They compared the heoretically expected ^{92}Nb/^{92}Mo ratio of $(1.72\ +1.40/-0.06) \times 10^{-5}$ (i.e., ^{92}Nb/^{92}Mo = 3.12×10^{-5}) in the

interstellar medium (hereafter, ISM) at the time of the birth of the Sun (Travaglio et al., 2014) with the initial solar system $^{92}Nb/^{92}Mo$ ratio of $(3.4 \pm 0.6) \times 10^{-5}$ (i.e., 2.8×10^{-5}) obtained from studies of meteorites, and derived a maximum $T_{isolation}$ (an isolation time: the interval between the time when the material that ended up in the solar system was isolated from the ISM and the time of the formation of the solar system) of 5.4 Myr. Moreover, they calculated the abundance ratio of a short-lived radionuclide to a stable isotope (N_{radio}/N_{stable}) in the material that built up the solar system just after the last addition from a nucleosynthetic event using the equation as follows (Lugaro et al. 2016);

$$N_{radio}/N_{stable} = K \times p_{radio}/p_{stable} \times \delta/T \times \{1 + e^{-\delta/\tau} / (1 - e^{-\delta/\tau})\} \quad \text{(viii)}$$

where p_{radio}/p_{stable} is the production ratio (1.58×10^{-3} for ^{92}Nb and 0.108 for ^{53}Mn; Travaglio et al. 2011, 2014) of each single SN event, τ is the mean-life of the radionuclide (50 Myr for ^{92}Nb and 5.3 Myr for ^{53}Mn), T (they used ~9,200 My) is the timescale of the evolution of the galaxy up to the formation of the Sun, and δ (they used ~8 My) is the free parameter of recurrence time between the events. The number K is a free parameter reflecting the effect of infall of low-metallicity gas, which was set to be 2 in the study. The obtained $^{53}Mn/^{55}Mn$ ratio of 2.41×10^{-4} results in a ratio of 5.82×10^{-5} after the isolation time of 5.4 Myr, which is one order of magnitude higher than the early solar system value $(6.28 \pm 0.66) \times 10^{-6}$ estimated from meteorite analysis (Trinquier et al. 2008b). In order to reconcile this contradiction in the abundance of

^{53}Mn in the early solar system as produced primarily by SNIa event, the isolation time needs to be at least 15 Myr. Taking into account the uncertainty in the half-life of ^{92}Nb did not solved the problem. Hence, Lugaro et al. (2016) concluded that the initial abundances of ^{92}Nb and ^{53}Mn cannot be consistently explained by a SNIa process unless the initial abundance of ^{92}Nb/^{92}Mo ratio in the early solar system was at least 50% lower than the current nominal value of ^{92}Nb/^{92}Mo = (3.4 ± 0.6) × 10^{-5}. Besides, Sanborn et al. (2019) recently estimated the initial ^{53}Mn abundance (^{53}Mn/^{55}Mn)$_0$ at the time of solar system formation by applying the Mn-Cr internal isochron dating to NWA 6704. The result yielded an initial ^{53}Mn/^{55}Mn ratio that is consistent with the canonical value within uncertainties, indicating the homogeneous distribution of ^{53}Mn in the early solar system. On the contrary, our study defines the initial ^{92}Nb/^{92}Mo value of (6.3 ± 0.6) × 10^{-5} using the obtained initial ^{92}Nb/^{93}Nb alue of (3.0 ± 0.3) × 10^{-5} and the solar Mo/Nb of 3.27 (Lodders et al. 2009). The initial ^{92}Nb/^{92}Mo value is distinctively higher than the maximum value in ISM (^{92}Nb/^{92}Mo = 3.12 × 10^{-5}) at the time of Sun's birth suggested in the SNIa model (Travaglio et al., 2014). Our results, therefore, can exclude the possibility of SNIa as the nucleosynthetic site of ^{92}Nb, and require another production site to be invoked for selectively producing ^{92}Nb.

At the moment, only the *ν*-process in SNII (e.g., Hayakawa et al. 2013, 2018) satisfies such a requirement of selective ^{92}Nb production (Fig. 30). Considering that ^{92}Nb is a short-lived radionuclide, the time-scale from the last SNII explosion to the formation of our solar system should not be so long. Consequently, our study hints at the existence of SNII shortly before the formation of the solar system, and the SNII

explosion as the nucleosynthetic origin of ^{92}Nb. Hayakawa et al. (2013) considered a scenario in which the observed ^{92}Nb was produced by a single injection of material from a nearby SNII into the precursor of solar system materials. Assuming that injected materials are well mixed with pre-existing materials in the protosolar cloud, the initial ^{92}Nb/^{93}Nb ratio will be;

$$[^{92}\mathrm{Nb}/^{93}\mathrm{Nb}]_{SSF} = f \times (^{92}\mathrm{Nb})_{SN} \times e^{-\Delta/\tau} / \{(^{93}\mathrm{Nb})_0 + f \times (^{93}\mathrm{Nb})_{SN}\} \quad \text{(ix)}$$

where $(^{92}\mathrm{Nb})_{SN}$ and $(^{93}\mathrm{Nb})_{SN}$ are the abundances in the SN ejecta, $(^{93}\mathrm{Nb})_0$ is the mass fraction of ^{93}Nb in the collapsing cloud, and τ is the mean-life of ^{92}Nb. The variables of Δ and f are free parameters in the injection model that represent the isolation time (i.e., time interval between the production of the short-lived radionuclide and the solar system formation) and the dilution factor (i.e., the fraction of material that mixes with the protosolar cloud of 1 $M_\odot$), respectively. Hayakawa et al. (2013) calculated the initial ^{92}Nb/^{93}Nb ratio taking the plausible values of Δ and f based on the evaluated values in the previous studies ($\Delta \sim 10^6$–10^8 yr; Dauphas 2005 / $f \sim 10^{-4}$–10^{-3}; Takigawa et al. 2008), and they concluded that the initial ^{92}Nb/^{93}Nb ratio of ~1.5 × 10^{-5} in the inner solar system can be reasonably explained with the value of $\Delta = 10^6 - 3 \times 10^7$ yr and $f = 3 \times 10^{-3}$. The results of this study revealed that the initial ^{92}Nb/^{93}Nb ratio should be higher than ~1.5 × 10^{-5} in the outer solar system, thereby requiring a shorter isolation time or a higher dilution factor than previously thought.

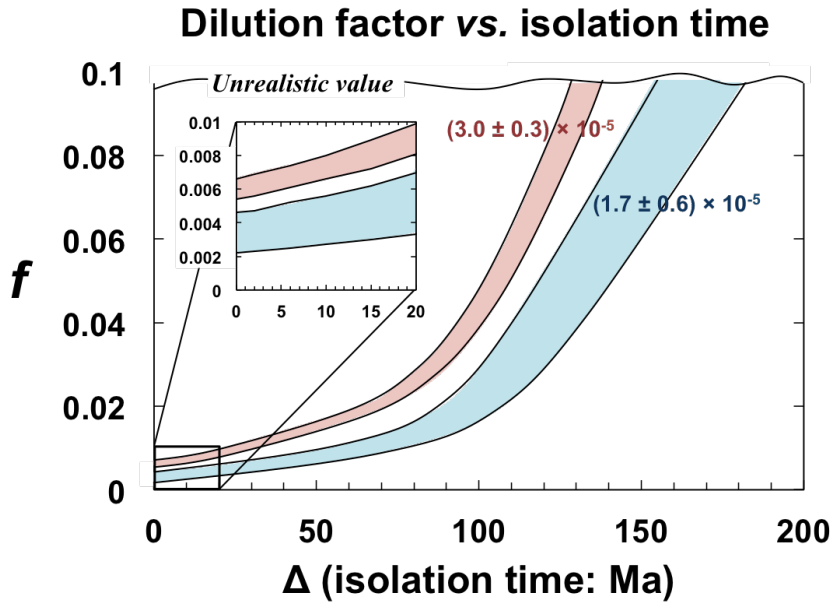

Fig. 36. The relation between dilution factor f vs. isolation time Δ. The pink area shows the possible range of the initial $[^{92}Nb/^{93}Nb]_{SSF} = (3.0 \pm 0.3) \times 10^{-5}$. The blue area shows the possible range of the initial $[^{92}Nb/^{93}Nb]_{SSF} = (1.7 \pm 0.6) \times 10^{-5}$. A required mass of 0.1 $M_{\odot}$ is unrealistically large. Although the isolation timescale are difficult to constrain precisely from ^{92}Nb because of its relatively long half-life, we can constrain from our study the value of f that shows the fraction of ^{92}Nb mixed with the protosolar cloud of 1 $M_{\odot}$ to be $f = \sim 6 \times 10^{-3}$.

4. 5. Conclusion

The initial abundance of a now-extinct radionuclide niobium-92 (^{92}Nb) provides valuable constraints on the timing of our solar system evolution, and on the origin of *p*-process nucleosynthesis. Although recent studies have defined an initial $^{92}Nb/^{93}Nb$ ratio of $(1.7 \pm 0.6) \times 10^{-5}$ at the time of the solar system formation, all samples have

been limited to the materials originated from the inner solar system. In this study, we have determined the initial abundance of ^{92}Nb in the outer solar system by applying the internal isochron approach to the NWA 6704 primitive achondrite, which samples the same isotopic reservoirs as the carbonaceous chondrite parent bodies. The results of Zr isotope measurements demonstrate that the ε^{96}Zr value of NWA 6704 (ε^{96}Zr = 1.54 ± 0.84) overlaps with the range of carbonaceous chondrites, which is consistent with the results of other stable isotope systematics in NWA 6704 (O, Cr, Ti, and Sr). The Nb-Zr isotope systematics of NWA 6704 defined the initial ^{92}Nb/^{93}Nb ratio of (2.8 ± 0.3) $\times 10^{-5}$ at the time of NWA 6704 formation (4562.76 ± 0.30 Ma), which corresponds to an initial ^{92}Nb/^{93}Nb of (3.0 ± 0.3) × 10^{-5} at the time of solar system formation. The obtained ratio is distinctly higher than the initial value in the inner solar system, which significantly affects the interpretation of the Nb-Zr early solar system chronology. At this time, the precise initial ^{92}Nb/^{93}Nb determined for NWA 6704 serves as the most reliable reference point for the Nb-Zr chronometry in the accretion region of the carbonaceous chondrite parent bodies. Using the newly obtained value, we further investigated the nucleosynthetic origin of ^{92}Nb. The obtained ^{92}Nb/^{92}Mo value of (6.3 ± 0.6) × 10^{-5} is clearly higher than the maximum ISM suggested in the SNIa model, which excluded the possibility of SNIa as the nucleosynthetic site of ^{92}Nb. The *ν*-process in SNII is the most probable origin for ^{92}Nb at the moment. If the initial ^{92}Nb abundance obtained in this study is representative of that of the bulk solar system, the time-scale from the last SNII explosion to the formation of our solar system and the dilution factor were roughly estimated to be <100 My and ~ 6 × 10^{-3}, respectively.

Consequently, our results imply the existence of SNII within ~10^8 years before the formation of the solar system and the enrichment of nuclides synthesized during the SNII in the outer solar system relative to the inner solar system.

5. Summary and future perspectives

In this thesis, we evaluated the initial abundance and distribution of ^{92}Nb in the early solar system, on the largest scale in history. This was achieved by studying a recently found achondrite NWA 6704. The results allowed us to evaluate the distribution of ^{92}Nb between the inner and outer solar system, and to provide new constraints on the early solar system chronology and on the astrophysical context of early solar system processes related to ^{92}Nb. The key findings of this thesis are summarized as follows.

1. We developed a new method for combined Cr–Ti isotope analysis applicable to various planetary materials. The developed method consists of three steps: (i) Fe removal using AG1-X8 anion exchange resin, (ii) Ti separation using TODGA resin, and (iii) Cr separation using AG50W-X8 cation exchange resin (with one additional step of Ti purification using AG1-X8 anion exchange resin only for samples having high Cr/Ti and Ca/Ti ratios). Both the utility and the validity of the new method have been verified by its application to compositionally varied terrestrial and meteorite samples, including terrestrial basalt JB-1b, terrestrial peridotite JP-1, Allende carbonaceous chondrite, and Juvinas non-cumulate eucrite. The developed method enables the combined isotope analyses of 3 μg of Cr and 1.5 μg of Ti, highlighting its potential application to various types of planetary materials.

2. The petrology, morphology and mineral chemistry collectively indicate the following crystallization sequence for NWA 6704: (1) melt-dominant state with a few grains of relict Mg-rich orthopyroxene and vermicular olivine-bearing orthopyroxene, (2) following rapid growth of orthopyroxene mostly on the pre-existing seeds under high super-saturation conditions, (3) as the temperature fell, dendritic growth of orthopyroxene ceased and thickening of branches proceeded with crystallization of awaruite and chromite followed by olivine and merrillite in the pore space between the orthopyroxene branches, and (4) finally plagioclase crystallized with limited numbers of nuclei and filled the well-connected pore space, resulting in the interlocking between plagioclase and othropyroxene megacrysts.

3. The parent asteroid of NWA 6704 underwent significant but instantaneous melting followed by cooling at a high rate (1–10^2 ˚C/hour) in the initial stage but a significantly lower rate (<10^{-4}–10^{-2} ˚C/hour at below ~1100 ˚C) in the later stage. The decrease of cooling rate in the late stage of the crystallization may reflect its burial under hot debris piled up within an ejecta blanket.

4. The Re-Os isochron age of 4576 ± 250 Ma, defined by the bulk and metal fractions, suggests system closure since crystallization. The roughly chondritic HSE abundances of the bulk fragments with only weakly fractionated HSE and REE patterns require that the parental melt and precursor had undergone neither significant segregation of metals, sulfides, nor silicate minerals. The limited

chemical fractionations among moderately and highly refractory elements during the igneous event can be attributed to the short timescale of the melting of the precursor and following crystallization.

5. The O, Cr, Ti and Zr stable isotope data showed that the parent body of NWA 6704 sampled the same reservoirs to those of carbonaceous chondrites. The stable isotope systematics strongly suggest that the NWA 6704 parent body was formed in the outer solar system. Further similarities between NWA 6704 and carbonaceous chondrites are observed in fO_2 and refractory major element abundances such as Ca/Mg and Al/Mg ratios. However, NWA 6704 has a Mg/Si ratio significantly lower than carbonaceous chondrites. These findings may imply that the NWA 6704 parent body formed under oxidized conditions in an outer region of the solar system where nebular fractionation of forsterite and earlier condensates proceeded efficiently, followed by implantation of a refractory component having elevated $\varepsilon^{54}Cr$, $\varepsilon^{50}Ti$, and $\varepsilon^{96}Zr$ values.

6. The mineral assemblage of NWA 6704 enables various internal isochron dating. In addition, the high cooling rate and its ancient crystallization age render this meteorite the first reliable *Time anchor* from the outer solar system for short-lived isotope chronometers such as Nb-Zr, Mn-Cr, and Hf-W chronometers.

7. The Nb–Zr internal isochron dating was applied to NWA 6704, and the initial

$^{92}Nb/^{93}Nb$ of $(2.8 \pm 0.3) \times 10^{-5}$ at the time of NWA 6704 formation (4562.76 ± 0.30 Ma) was obtained, which corresponds to an initial $^{92}Nb/^{93}Nb$ of $(3.0 \pm 0.3) \times 10^{-5}$ at the time of solar system formation. The ratio is distinctly higher than the value in the inner solar system, which significantly affects the interpretation of the Nb-Zr early solar system chronology.

8. The *ν*-process in Type II supernova (SNII) is the most probable origin for ^{92}Nb at the moment. Furthermore, the higher initial ^{92}Nb abundance obtained in this study relative to the previous studies suggests that nuclides synthesized in SNII $<10^8$ years before the solar system formation were enriched in the outer solar system than the inner solar system.

Finally, several future perspectives and unsolved problems are listed below.

(1) *The application of combined Cr-Ti isotope analysis to planetary materials*

A new method for sequential Cr-Ti isotope analysis applicable to various materials was developed. As discussed in Chapter 2, the present method enables the combined isotope analyses of 3 μg of Cr and 1.5 μg of Ti. These amounts correspond to single ~1 mm chondrules and ~2 mm CAIs, assuming typical Cr and Ti abundances. Further refinement of the method will enable us to apply our new method to various micrometer-sized meteoritic components. Such combined Cr and Ti isotope analyses of primitive meteorite components will facilitate understanding

of the carrier of the isotopic anomalous observed among planetary materials, and of the nature and evolution of the protoplanetary disk. Furthermore, the application of our new method to various types of differentiated meteorites could provide new constraints on their genetic relationship.

(2) *On the origin of primitive achondrites*

The lines of evidence in Chapter 3 indicated that the NWA 6704 primitive achondrites formed by impact-induced instantaneous melting on an undifferenciated asteroid at a few million years after CAI formation. Further investigations of other ungrouped primitive achondrites for the petrology, geochemistry, and various isotope systematics are important for understanding whether such process was common in the early solar system or not. Moreover, we have argued the formation of NWA 6704 in the outer solar system based on the O-Cr-Ti-Zr isotope compositions plotted within the range of carbonaceous chondrites. However, the distinct nucleosynthetic isotope anomalies could be attributed to the significant addition of refractory components such as CAIs to the materials in the inner solar system. Indeed, our data indicate that NWA 6704 is clearly distinct from carbonaceous chondrites and rather similar to non-carbonaceous chondrites in terms of major element composition (e.g., Mg/Si and Al/Si). Thus, although we have attributed the Si enrichment in NWA 6704 to the forsterite fractionation and the following refractory component addition to NWA 6704 in the outer solar system, further validations of the inference need to be performed in the future.

(3) *Relevance to other short-lived nuclides*

Our finding of ^{92}Nb enrichment in the outer solar system requires that either the isolation time is shorter or the dilution factor *f* is higher than previously thought. However, such a high dilution factor would be hard to reconcile with the low initial abundances of other short-lived radionuclides which are considered to have originated from SNII (e.g., ^{26}Al, ^{182}Hf). Thus, although we have discussed the consistency/inconsistency between the initial ^{53}Mn and ^{92}Nb abundances in this thesis, more comprehensive inspections on short-lived radionuclides are required in the future.

(4) *The formation mechanism of the isotopic dichotomy in the early solar system*

Although it has been well established that carbonaceous and non-carbonaceous meteorites have distinctive nucleosynthetic isotopic anomalies for various elements including Cr and Ti, the mechanism of the isotopic dichotomy formation remains poorly known. Basically, two models have been proposed to generate the isotopic dichotomy at the planetary scale. One model is that extremely neutron-rich nano-phases produced in a supernova were injected into the solar nebula at a large heliocentric distance. The other model is that the local thermal processing of molecular cloud materials resulted in the preferential loss of thermally unstable presolar silicates. The results of this study indicate that carbonaceous meteorites are enriched in ^{92}Nb relative to non-carbonaceous meteorites, suggesting that nuclides

synthesized in the last SNII were preferentially sampled by the former. Furthermore, it has recently been suggested that Group II CAIs (amalgamation of many different presolar phases) might have an initial ^{92}Nb abundance comparable to our estimate for the outer solar system, whereas Group I CAIs would have the inner solar system initial abundance (Lai et al. 2017). The implication would be that nuclides from the last SNII were preferentially implanted/preserved either in the region of or during the Group II CAI formation rather than the Group I formation. It remains to be evaluated whether such preferential contribution of the last SNII to the outer solar system (the dilution factors $f = 3 \times 10^{-3}$ and 6×10^{-3} for the inner and outer solar system, respectively) can consistently account for the observed stable isotope dichotomy. Future combination of high-precision dating and nucleosynthetic isotopic study on single CAIs would provide further constraints on the formation mechanism of the isotopic dichotomy. Besides, the homogeneity of ^{92}Nb distribution within the early outer solar system needs to be explored by establishing another *Time anchor* originated from the outer solar system.

Acknowledgements

First of all, I would like to express my heartfelt gratitude to my supervisor, Prof. Tsuyoshi Iizuka. Without his continuous guidance and support since I started my research activity about five years ago, I could not have completed this PhD thesis.

Thanks are extended to Profs. Shogo Tachibana, Takafumi Hirata, Tetsuya Yokoyama, and Hajime Hiyagon, for their invaluable comments, which significantly improved the PhD thesis. I am also grateful to Prof. T. Tsuihiji, Drs. S. Kuehner, and R. Conrey, Messrs. A. Okubo, K. Ichimura, H. Yoshida, O. Sasaki, and K. Yoshizawa for their analytical support, Profs. Y. Amelin, T. Mikouchi, and T. Noguchi, Drs. V. A. Fernandes, M. Kimura, and Y. Takagi for fruitful discussions, Prof. J. A. Barrat for providing the whole rock chemistry data as well as constructive comments, and Drs. G. Hupé and J. Kashuba for kindly providing the images of NWA 6704.

The efforts of all co-workers are greatly appreciated. Analyses for highly siderophile element abundances and ^{187}Re–^{187}Os isotope systematics of NWA 6704 were conducted by Dr. Gregory Archer (at the University of Maryland), the U.S. Oxygen isotope analysis of NWA 6704 was conducted by Prof. Ryoji Tanaka (at the Institute for Planetary Materials, Okayama University), Japan. All micro X-ray CT raw data of NWA 6704 was obtained by Messr. Yuya Sato (at Tohoku Univesity, Japan). Part of the major element geochemistry of NWA 6704 was examined by Prof. A. J. Irving (at the Washington State University Geoanalytical Laboratory), the U.S. Part of the solution-based bulk and mineral chemistry measurement of NWA 6704/6693 was carried out by Dr. M. Sanborn (at the University of California, Davis, the U.S). I thank Prof.. K. Yamashita, Drs. S. Yoneda and A. Yamakawa for helping me the Cr isotope analyses, always keeping TIMS machines in the best condition as well as giving me a lot of advice and encouragement.

My research projects have been supported by the Japan Society for the Promotion of Science (Core-to-Core Program ‘‘International Network of Planetary Sciences”; Grants #16J04429 to YH; Grant #25707042 and #26220713 to TI) and NASA (Cosmochemistry grant NNX13AF83G to RJW, Emerging Worlds grant

NNX16AD34D to QZY). Continuous support from the administrative staff in the Department of Earth and Planetary Science of the University of Tokyo is also appreciated.

Yuki Hibiya
Tokyo, December 2018

References

Akram, W., Schönbächler, M., Sprung, P., and Vogel, N. (2013). Zirconium—Hafnium isotope evidence from meteorites for the decoupled synthesis of light and heavy neutron-rich nuclei. *The Astrophysical Journal,* **777**, 169.

Akram, W., Schönbächler, M., Bisterzo, S., andGallino, R. (2015). Zirconium isotope ev- idence for the heterogeneous distribution of s-process materials in the solar system. *Geochim. Cosmochim. Acta* **165**, 484–500.

Albarède, F., and Beard, B. (2004). Analytical methods for non-traditional isotopes. *Reviews in mineralogy and geochemistry,* **55**, 113–152.

Alexander, C. M. D. (2005). Re-examining the role of chondrules in producing the elemental fractionations in chondrites. *Meteoritics and Planetary Science*, **40**, 943–965.

Amelin Y., Kaltenbach A., Iizuka T., Stirling C. H., Ireland T. R., Petaev M. and Jacobsen S. B. (2010) U-Pb chronology of the Solar System's oldest solids with variable $^{238}U/^{235}U$. *Earth Planet. Sci. Lett.* **300,** 343–350.

Amelin Y., Koefoed P., Iizuka T., Fernandes V. A., Huyskens M., Yin Q.-Z. and Irving A. J. (2019) U-Pb, Rb-Sr and Ar-Ar systematics of the ungrouped achondrites Northwest Africa 6704 and Northwest Africa 6693. *Geochim. Cosmochim. Acta.* https://doi.org/10.1016/j.gca.2018.09.021.

Anders, E., and Goles, G. C. (1961). Theories on the origin of meteorites. *J. Chem. Educ*, **38**, 58.

Anders E., and Grevesse N. (1989). Abundances of the elements: Meteoritic and solar. *Geochim. Cosmochim. Acta*, **53**, 197–214.

Archer G.J., Ash R.D., Bullock E.S., and Walker R.J. (2014). Highly siderophile elements and ^{187}Re–^{187}Os isotopic systematics of the Allende meteorite: Evidence for

primary nebular processes and late-stage alteration. *Geochim. Cosmochim. Acta,* **131**, 402–414.

Arndt, N. T., and Fleet, M. E. (1979). Stable and metastable pyroxene crystallization in layered komatiite lava flows. *American Mineralogist*, **64**, 856–864.

Arnould, M., Goriely, S., and Takahashi, K. (2007). The r-process of stellar nucleosynthesis: Astrophysics and nuclear physics achievements and mysteries. *Physics Reports*, **450**, 97-213.

Ballhaus, C., Berry, R. F., and Green, D. H. (1991). High pressure experimental calibration of the olivine-orthopyroxene-spinel oxygen geobarometer: implications for the oxidation state of the upper mantle. *Contributions to Mineralogy and Petrology,* **107**, 27–40.

Barrat, J. A., Jambon, A., Bohn, M., Blichert-Toft, J., Sautter, V., Göpel, C., Gillet, Ph., Boudouma, O., and Keller, F. (2003). Petrology and geochemistry of the unbrecciated achondrite Northwest Africa 1240 (NWA 1240): an HED parent body impact melt. *Geochim. Cosmochim. Acta*, **67**, 3959–3970.

Barnes S.-J., Naldrett A.J., and Gorton M.P. (1985). The origin of the fractionation of platinum-group elements in terrestrial magmas. *Chemical Geology,* **53**, 302–323.

Becker H., Morgan J.W., Walker R.J., MacPherson G.L. and Grossman J.N. (2001). Rhenium–osmium systematics of calcium–aluminum-rich inclusions in carbonaceous chondrites. *Geochim. Cosmochim. Acta,* **65**, 3379–3390.

Bédard, J. H. (2007). Trace element partitioning coefficients between silicate melts and orthopyroxene: parameterizations of D variations. *Chemical Geology*, **244**, 263-303.

Benedix, G. K., McCoy, T. J., Keil, K., Bogard, D. D., and Garrison, D. H. (1998). A petrologic and isotopic study of winonaites: Evidence for early partial melting, brecciation, and metamorphism. *Geochim. Cosmochim. Acta*, **62**, 2535–2553.

Benedix, G. K., Lauretta, D. S., and McCoy, T. J. (2005). Thermodynamic constraints on the formation conditions of winonaites and silicate-bearing IAB irons. *Geochim. Cosmochim. Acta*, **69**, 5123–5131.

Birck, J. L., Barman, M. R., and Capmas, F. (1997). Re–Os isotopic measurements at the femtomole level in natural samples. Geostandards and Geoanalytical Research, **21**, 19–27.

Bogdanovski, O., and G. W. Lugmair. (2004). Manganese-chromium isotope systematics of basaltic achondrite Northwest Africa 011. In 35th *Lunar and Planetary Science Conference*, #1715 (abstract).

Bottke, W. F., Vokrouhlický, D., Marchi, S., Swindle, T., Scott, E. R. D., Weirich, J. R., and Levison, H. (2015). Dating the Moon-forming impact event with asteroidal meteorites. *Science*, **348**, 321-323.

Bonnand P., Parkinson I. J., James R. H., Karjalainen A. M., and Fehr M. A. (2011) Accurate and precise determination of stable Cr isotope compositions in carbonates by double spike MC-ICP-MS. *Journal of Analytical Atomic Spectrometry,* **26**, 528–535.

Bonnand P., Williams H. M., Parkinson I. J., Wood B. J. and Halliday A. N. (2016) Stable chromium isotopic composition of meteorites and metal–silicate experiments: Implications for fractionation during core formation. *Earth and Planetary Science Letters*, **435,** 14–21.

Bonnand, P., Parkinson, I. J., and Anand, M. (2016b). Mass dependent fractionation of stable chromium isotopes in mare basalts: Implications for the formation and the differentiation of the Moon. *Geochim. Cosmochim. Acta*, **175**, 208–221.

Borisov A. and Palme H. (1995). The solubility of iridium in silicate melts: new data from experiments with $Ir_{10}Pt_{90}$ alloys. *Geochim. Cosmochim. Acta,* **59**, 481–485.

Bouvier A., Spivak-Birndorf L. J., Brennecka G. A. and Wadhwa M. (2011a) New constraints on early Solar System chronology from Al-Mg and U-Pb isotope systematics in the unique basaltic achondrite Northwest Africa 2976. *Geochim. Cosmochim. Acta,* **75**, 5310–5323.

Bouvier A., Brennecka G. A. and Wadhwa M. (2011b) Absolute chronology of the first solids in the solar system. In Workshop on the Formation of the First Solids in the Solar System. *Lunar Planet. Inst.,* Houston. #9054. (abstract).

Brandon A.D., Humayun M., and Puchtel I.S. (2005). Re–Os isotopic systematics and platinum group element concentration of the Tagish Lake carbonaceous chondrite. *Geochim. Cosmochim. Acta,* **69**, 1619–1631.

Brandon A.D., Puchtel I.S., Walker R.J., Day J.M.D., Irving, A.J., and Taylor L.A. (2012). Evolution of the martian mantle inferred from the ^{187}Re–^{187}Os isotope and highly siderophile element abundance systematics of shergottite meteorites. *Geochim. Cosmochim. Acta,* **76**, 206–235.

Brearley, A. J. (1991). Subsolidus microstructures and cooling history of pyroxenes in the Zagami shergottite. *Lunar Planet. Sci. XXII,* Lunar Planet. Inst., Houston. #135 (abstract).

Brennecka, G. A., and Wadhwa, M. (2012). Uranium isotope compositions of the basaltic angrite meteorites and the chronological implications for the early Solar System. *Proceedings of the National Academy of Sciences,* **109**, 9299-9303.

Breton T. and Quitté G. (2014). High-precision measurements of tungsten stable isotopes and application to earth sciences. *Journal of Analytical Atomic Spectrometry*, **29**, 2284–2293.

Burbidge, E. M., Burbidge, G. R., Fowler, W. A., and Hoyle, F. (1957). Synthesis of the elements in stars. *Reviews of modern physics*, **29**, 547.

Burkhardt C., Dauphas N., Tang H., Fischer-Gödde M., Qin L., Chen J. H., Rout S. S., Pack A., Heck P. R., and Papanastassiou D. A. (2017). In search of the Earth - forming reservoir: Mineralogical, chemical, and isotopic characterizations of the ungrouped achondrite NWA 5363/NWA 5400 and selected chondrites. *Meteoritics and Planetary Science,* **52,** 807–826.

Byelikov, A., Adachi, T., Fujita, H., Fujita, K., Fujita, Y., Hatanaka, K., Heger, A., Kalmykov, Y., Kawase, K., Langanke, K., Martínez-Pinedo, G., Nakanishi, K., von Neumann-Cosel, P., Neveling, R., Richter, A., Sakamoto, N., Sakemi, Y., Shevchenko, A., Shimbara, Y., Shimizu, Y., Smit, F. D., Tameshige, Y., Tamii, A., Woosley, S. E., and Yosoi, M. (2007). Gamow-Teller Strength in the Exotic Odd-Odd Nuclei La-138 and Ta-180 and Its Relevance for Neutrino Nucleosynthesis. *Physical review letters*, **98,** 082501.

Cameron, A. G. W. (1957). Nuclear reactions in stars and nucleogenesis. *Publications of the Astronomical Society of the Pacific*, **69**, 201–222.

Capobianco C.J., Jones J. H., and Drake M.J. (1993). Metal-silicate thermochemistry at high temperature: Magma oceans and the "excess siderophile element" problem of the Earth's Upper Mantle. *J. Geophys. Res.* **98**, 5433–5443.

Carlson, R. W., and Boyet, M. (2009). Short-lived radionuclides as monitors of early crust–mantle differentiation on the terrestrial planets. *Earth and Planetary Science Letters*, **279**, 147–156.

Carlson R. W. and Hauri E. H. (2001). Extending the ^{107}Pd–^{107}Ag chronometer to low Pd/Ag meteorites with multicollector plasma-ionization mass spectrometry. *Geochim. Cosmochim. Acta,* **65**, 1839–1848.

Cheoun, M. K., Ha, E., Hayakawa, T., Chiba, S., Nakamura, K., Kajino, T., and Mathews, G. J. (2012). Neutrino induced reactions for ν-process nucleosynthesis of 92 Nb and 98 Tc. *Physical Review C*, **85,** 065807.

Choi, B. G., Huss, G. R., Wasserburg, G. J., and Gallino, R. (1998). Presolar corundum and spinel in ordinary chondrites: Origins from AGB stars and a supernova. *Science*, **282**, 1284–1289.

Clayton, R. N., Grossman, L., and Mayeda, T. K. (1973). A component of primitive nuclear composition in carbonaceous meteorites. *Science*, **182**, 485-488.

Clayton R. N., Onuma N., and Mayeda T. K. (1976). A classifi- cation of meteorites based on oxygen isotopes. *Earth Planet. Sci. Lett.* **30,** 10–18.

Clayton, R. N. (2002). Solar System: Self-shielding in the solar nebula. *Nature,* **415,** 860–861.

Clayton R. N., and Mayeda T. K. (1988). Formation of ureilites by nebular processes. *Geochim. Cosmochim. Acta.* **52**, 1313–1318.

Clayton R. N., Mayeda T. K., Goswami J. N., and Olsen E. J. (1991). Oxygen isotope studies of ordinary chondrites. *Geochim. Cosmochim. Acta,* **55**, 2317–2337.

Clayton, R. N., and Mayeda, T. K. (1996). Oxygen isotope studies of achondrites. *Geochim. Cosmochim. Acta*, **60**, 1999–2017.

Clayton, R. N., and Mayeda, T. K. (1999). Oxygen isotope studies of carbonaceous chondrites. *Geochim. Cosmochim. Acta*, **63**, 2089–2104.

Cody, A. M., and Cody, R. D. (1995). Dendrite formation by apparent repeated twinning of calcium oxalate dihydrate. *Journal of crystal growth*, **151**, 369–374.

Cohen A.S. and Waters F.G. (1996). Separation of osmium from geological materials by solvent extraction for analysis by thermal ionisation mass spectrometry. *Anal. Chim. Acta,* **332**, 269–275.

Cole D. B., Reinhard C. T., Wang X., Gueguen B., Halverson G. P., Gibson T., Hodgskiss M. S.W., McKenzie N. R., Timothy W. L., and Planavsky N. J. (2016). A shale-hosted Cr isotope record of low atmospheric oxygen during the Proterozoic. *Geology*, **44,** 555-558.

Connelly J. N., Bizzarro M., Krot A. N., Nordlund A., Wielandt D., and Ivanova M. A. (2012). The absolute chronology and thermal processing of solids in the solar protoplanetary disk. *Science* **338**, 651–655.

Cook, D. L., Clayton, R. N., Wadhwa, M., Janney, P. E., and Davis, A. M. (2008). Nickel isotopic anomalies in troilite from iron meteorites. *Geophysical Research Letters*, **35**.

Creaser R. A., Papanastassiou D. A., and Wasserburg G. J. (1991). Negative thermal ion mass spectrometry of osmium, rhenium and iridium. *Geochim. Cosmochim. Acta,* **55**, 397–401.

Dauphas, N., Rauscher, T., Marty, B., and Reisberg, L. (2003). Short-lived p-nuclides in the early solar system and implications on the nucleosynthetic role of X-ray binaries. *Nuclear Physics A*, **719,** C287-C295.

Dauphas, N. (2005). Multiple sources or late injection of short-lived r-nuclides in the early solar system?. *arXiv preprint astro-ph/0502514*.

Dauphas, N., Remusat, L., Chen, J. H., Roskosz, M., Papanastassiou, D. A., Stodolna, J., Guan, Y., Ma, C., and Eiler, J. M. (2010). Neutron-rich chromium isotope anomalies in supernova nanoparticles. *The Astrophysical Journal*, **720**, 1577.

Dauphas N. and Chaussidon M. (2011). A perspective from extinct radionuclides on a young stellar object: the Sun and its accretion disk. *Annu. Rev. Earth Planet. Sci.* **39**, 351–386.

Dauphas, N., Poitrasson, F., Burkhardt, C., Kobayashi, H., and Kurosawa, K. (2015). Planetary and meteoritic Mg/Si and δ^{30}Si variations inherited from solar nebula chemistry. *Earth Planet. Sci. Lett.,* **427,** 236–248.

Dauphas, N., and Schauble, E. A. (2016). Mass fractionation laws, mass-independent effects, and isotopic anomalies. *Annual Review of Earth and Planetary Sciences*, **44**, 709–783.

Davis, A. M., and McKeegan, K. D. (2014). Short-lived radionuclides and early solar system chronology. *Meteorites and Cosmochemical Processes*, 361–395.

Day J.M.D., Ash R.D., Liu Y., Bellucci J.J., Rumble D. III., McDonough W.F., Walker R.J., and Taylor L.A. (2009). Early formation of evolved asteroidal crust. *Nature,* **457**, 179–182.

Day J. M. D., Pearson D. G., Macpherson C. G., Lowry D. and Carracedo J. C. (2010). Evidence for distinct proportions of subducted oceanic crust and lithosphere in HIMU-type mantle beneath El Hierro and La Palma, Canary Islands. *Geochim. Cosmochim. Acta,* **74**, 6565–6589.

Day J. M. D., Walker R. J., Ash R. D., Liu Y., Rumble D. III., Irving A. J., Goodrich C. A., Tait K., McDonough W. F., and Taylor L. A. (2012). Origin of felsic achondrites Graves Nunataks 06128 and 06129, and ultramafic brachinites and brachinite-like achondrites by partial melting of volatile-rich primitive parent bodies. *Geochim. Cosmochim. Acta,* **81**, 94–128.

Day, J., Corder, C. A., Rumble, D., Assayag, N., Cartigny, P., and Taylor, L. A. (2015). Differentiation processes in FeO-rich asteroids revealed by the achondrite Lewis Cliff 88763. *Meteoritics and Planetary Science*, **50**, 1750–1766.

de Leuw S., Papanastassiou D., and Wasson J. T. (2010). Chromium isotopes in chondrites and the heterogeneous accretion of the solar nebula. *In* 4*1th Lunar and Planetary Science Conference*,#2703 (abstract).

Durant, D. G., and Fowler, A. D. (2002). Origin of reverse zoning in branching orthopyroxene and acicular plagioclase in orbicular diorite, Fisher Lake, California. *Mineralogical Magazine,* **66**, 1003–1020.

Fabriès, J. (1979). Spinel-olivine geothermometry in peridotites from ultramafic complexes. *Contributions to Mineralogy and Petrology*, **69**, 329–336.

Fernandes, V. A., Burgess, R., Crowther, S. A., Fritz, J. P., Gilmour, J. D., Irving, A., Meier, M. M. M., Nottingham, M., and Wieler, R. (2013). ^{40}Ar-^{39}Ar and Noble Gas Systematics of the Ungrouped Achondrite Northwest Africa 6704. *Lunar Planet. Sci. XLIV*, Lunar Planet. Inst., Houston. #1956 (abstract).

Fischer-Gödde M., Becker H., and Wombacher F. (2010). Rhodium, gold and other highly siderophile element abundances in chondritic meteorites. *Geochim. Cosmochim. Acta.,* **74**, 356–379.

Fitoussi, C., Bourdon, B., Kleine, T., Oberli, F., and Reynolds, B. C. (2009). Si isotope systematics of meteorites and terrestrial peridotites: implications for Mg/Si fractionation in the solar nebula and for Si in the Earth's core. *Earth Planet. Sci. Lett.,* **287**, 77–85.

Fleet, M. E., and MacRae, N. D. (1975). A spinifex rock from Munro Township, Ontario. *Canadian Journal of Earth Sciences,* **12**, 928–939.

Floss, C., Crozaz, G., Jolliff, B., Benedix, G., and Colton, S. (2008). Evolution of the winonaite parent body: Clues from silicate mineral trace element distributions. *Meteoritics and Planetary Science*, **43**, 657–674.

Fortenfant, S. S., Günther, D., Dingwell, D. B., and Rubie, D. C. (2003). Temperature dependence of Pt and Rh solubilities in a haplobasaltic melt. *Geochim. Cosmochim. Acta*, **67**, 123–131.

Franchi, I. A., Wright, I. P., Sexton, A. S., and Pillinger, C. T. (1999). The oxygen-isotopic composition of Earth and Mars. *Meteoritics and Planetary Science,* **34**,

657–661.

Frei R., Gaucher C., Poulton S. W., and Canfield D. E. (2009). Fluctuations in Precambrian atmospheric oxygenation recorded by chromium isotopes. *Nature*, **461**, 250–254.

Fritz, J., Greshake, A., and Fernandes, V. A. (2017). Revising the shock classification of meteorites. *Meteoritics and Planetary Science*, **52**, 1216–1232.

Gardner-Vandy, K. G., Lauretta, D. S., Greenwood, R. C., McCoy, T. J., Killgore, M., and Franchi, I. A. (2012). The Tafassasset primitive achondrite: Insights into initial stages of planetary differentiation. *Geochim. Cosmochim. Acta,* **85**, 142–159.

Gerber S., Burkhardt C., Budde G., Metzler K., and Kleine T. (2017). Mixing and transport of dust in the early solar nebula as inferred from titanium isotope variations among chondrules. *The Astrophysical Journal Letters,* **841**, 1–7.

Ghosh, A., Weidenschilling, S. J., McSween Jr, H. Y., and Rubin, A. (2006). Asteroidal heating and thermal stratification of the asteroid belt. *Meteorites and the early solar system II*, 555–566.

Glavin D. P., Kubny A., Jagoutz E., and Lugmair G. W. (2004). Mn-Cr isotope systematics of the D'Orbigny angrite. *Meteor. Planet. Sci*., **39**, 693–700.

Goodrich, C. A. (1992). Ureilites-A critical review, *Meteoritics*, **27**, 327–352.

Goodrich, C. A., and Delaney, J. S. (2000). Fe/Mg–Fe/Mn relations of meteorites and primary heterogeneity of primitive achondrite parent bodies. *Geochim. Cosmochim. Acta,* **64**, 149–160.

Goodrich C. A., Kita N. T., Yin Q. Z., Sanborn M. E., Williams C. D., Nakashima D., Lane M. D. and Boyle S. (2017). Petrogenesis and provenance of ungrouped achondrite Northwest Africa 7325 from petrology, trace elements, oxygen, chromium and titanium

isotopes, and mid-IR spectroscopy. *Geochim. Cosmochim. Acta,* **203**, 381–403.

Göpel, C., and Birck, J. L. (2010). Mn/Cr systematics: A tool to discriminate the origin of primitive meteorites. *Goldschmidt Conference* #348 (abstract).

Göpel, C., Birck, J. L., Galy, A., Barrat, J. A., and Zanda, B. (2015). Mn–Cr systematics in primitive meteorites: Insights from mineral separation and partial dissolution. *Geochim. Cosmochim. Acta*, **156**, 1–24.

Goswami, J. N. (2004). Short-lived nuclides in the early solar system: the stellar connection. *New Astronomy Reviews*, **48**, 125–132.

Gounelle, M., Shu, F. H., Shang, H., Glassgold, A. E., Rehm, K. E., and Lee, T. (2006). The irradiation origin of beryllium radioisotopes and other short-lived radionuclides. *The Astrophysical Journal*, **640**, 1163.

Graham, A. L., Easton, A. J., and Hutchison, R. (1977). Forsterite ehondrites; the meteorites Kakangari, Mount Morris (Wisconsin), Pontlyfiri, and Winona. *Mineral. Mag,* **41**, 201–210.

Greenwood, R. C., and Franchi, I. A. (2004). Alteration and metamorphism of CO3 chondrites: Evidence from oxygen and carbon isotopes. *Meteoritics and Planetary Science Archives*, **39**, 1823–1838.

Greenwood R. C., Franchi I. A., Jambon A. and Buchanan P. C. (2005). Widespread magma oceans on asteroidal bodies in the early Solar System. *Nature,* **435**, 916–918.

Greenwood, R. C., Franchi, I. A., Kearsley, A. T., and Alard, O. (2010). The relationship between CK and CV chondrites. *Geochim. Cosmochim. Acta*, **74**, 1684–1705.

Greenwood, R. C., Franchi, I. A., Gibson, J. M., and Benedix, G. K. (2012). Oxygen isotope variation in primitive achondrites: The influence of primordial, asteroidal and

terrestrial processes. *Geochim. Cosmochim. Acta*, **94**, 146–163.

Gueguen B., Reinhard C.T., Algeo T.J., Peterson L.C., Nielsen S.G., Wang X. and Planavsky N.J. (2016) The chromium isotope composition of reducing and oxic marine sediments. *Geochim. Cosmochim. Acta,* **184**, 1–19.

Haba, M. K., Lai Y. J., Wotzlaw J. F., Yamaguchi A., von Quadt A., and Schönbächler M. (2017) Rutiles and Zircons of Mesosiderites: Combined Niobium-Zirconium and Uranium-Lead Chronometry and the Initial Abundance of Niobium-92 in the Solar System. in *48th Lunar and Planetary Science Conference*, The Woodlands, Texas, 20 to 24 March 2017 (LPSC 2017), Abstract # 1739.

Harju, E. R., Rubin, A. E., Ahn, I., Choi, B. G., Ziegler, K., and Wasson, J. T. (2014). Progressive aqueous alteration of CR carbonaceous chondrites. *Geochim. Cosmochim. Acta*, **139**, 267–292.

Harper Jr., C.L. (1996). Evidence for $^{92}{}_{g}$Nb in the early solar system and evalua- tion of a new *p*-process cosmochronometer from $^{92}{}_{g}$Nb/^{92}Mo. *Astrophys. J.,* **466**, 437–456.

Hayakawa T., Nakamura K., Kajino T., Chiba S., Iwamoto N., Cheoun M. K., and Mathews G. J. (2013). Supernova neutrino nucleosynthesis of the radioactive ^{92}Nb observed in primitive meteorites. *Astrophys. J. Lett.,* **779**, L9.

Hayakawa, T., Ko, H., Cheoun, M. K., Kusakabe, M., Kajino, T., Usang, M. D., Chiba, S., Nakamura, K., Tolstov, A., Nomoto, K., Hashimoto, M. A., Ono, M., Kawano, T., and Mathews, G. J. (2018). Short-Lived Radioisotope Tc 98 Synthesized by the Supernova Neutrino Process. *Physical review letters*, **121,** 102701.

Heger A., Kolbe E., Haxton W. C., Langanke K., Martinez–Pinedo G., and Woosley S. E., (2005). Neutrino nucleosynthesis. *Phys. Lett. B,* **606**, 258–264

Hewins, R. H., and Zanda, B. (2012). Chondrules: Precursors and interactions with the nebular gas. *Meteoritics and Planetary Science,* **47**, 1120–1138.

Hezel D. C., Harak M. and Libourel G. (2018). What we know about elemental bulk chondrule and matrix compositions: Presenting the ChondriteDB Database. *Chemie der Erde*, **78**, 1–14.

Hibiya, Y., Iizuka, T., Yamashita, K., Yoneda, S., and Yamakawa, A. (2019a) Sequential Chemical Separation of Cr and Ti from a Single Digest for High-Precision Isotope Measurements of Planetary Materials. *Geostandards and Geoanalytical Research*. https://doi.org/10.1111/ggr.12249

Hibiya Y., Archer G. J., Tanaka R., Sanborn M. E., Sato Y., Iizuka T., Ozawa K., Walker R. J., Yamaguchi A., Yin Q-Z., Nakamura T., and Irving, A. J. (2019b). The origin of the unique achondrite Northwest Africa 6704: Constraints from petrology, chemistry and Re–Os, O and Ti isotope systematics. *Geochim. Cosmochim. Acta*, **245**, 597-627. https://doi.org/10.1016/j.gca.2018.04.031

Hirata, T. (2001). Determinations of Zr isotopic composition and U–Pb ages for terrestrial and extraterrestrial Zr-bearing minerals using laser ablation-inductively coupled plasma mass spectrometry: implications for Nb–Zr isotopic systematics. *Chemical Geology*, **176**, 323-342.

Hoffman, R. D., Woosley, S. E., Fuller, G. M., and Meyer, B. S. (1996). Production of the light p-process nuclei in neutrino-driven winds. *The Astrophysical Journal*, **460,** 478.

Holden N. E. (1990). Total half-lives for selected nuclides. *Pure Appl. Chem.,* **62**, 941–958.

Honda M. and Imamura M. (1971). Half-life of Mn–53. *Physical Review C,* **4**, 1182–1188.

Horai, K., and Winkler, J. (1974). Thermal Diffusivity of Lunar Rock Sample 12001, 85. *Lunar Planet. Sci. VI,* Lunar Planet. Inst., Houston. pp. 354–356 (abstract).

Horan M. F., Walker R. J., Morgan J. W., Grossman J. N. and Rubin A. (2003). Highly siderophile elements in chondrites. *Chem. Geol*., **196**, 5–20.

Huss, G. R., Meyer, B. S., Srinivasan, G., Goswami, J. N., and Sahijpal, S. (2009). Stellar sources of the short-lived radionuclides in the early solar system. *Geochimica et Cosmochimica Acta*, **73,** 4922–4945.

Iizuka, T., Kaltenbach, A., Amelin, Y., and Stirling, C. H. (2013). U–Pb systematics of eu- crites in relation to their thermal history. In 4*4th Lunar and Planetary Science Conference*, #1907 (abstract).

Iizuka, T., Amelin, Y., Kaltenbach, A., Koefoed, P., and Stirling, C. H. (2014). U–Pb systematics of the unique achondrite Ibitira: precise age determination and petrogenetic implications. *Geochim. Cosmochim. Acta.,* **132**, 259–273.

Iizuka, T., Yamaguchi, A., Haba, M.K., Amelin, Y., Holden, P., Zink, S., Huyskens, M.H., and Ireland, T.R. (2015). Timing of global crustal metamorphism on Vesta as revealed by high-precision U–Pb dating and trace element chemistry of eucrite zircon. *Earth Planet. Sci. Lett.,* **409**, 182–192.

Iizuka T., Lai Y. J., Akram W., Amelin Y., and Schönbächler M. (2016). The initial abundance and distribution of ^{92}Nb in the Solar System. *Earth and Planet. Sci. Lett.* **439**, 172–181.

Imai N., Terashima S., Itoh S. and Ando A. (1995). 1994 compilation values for GSJ reference samples,"Igneous rock series". *Geochemical Journal,* **29**, 91–95.

Irving A.J., Tanaka R., Steele A., Kuehner S.M., Bunch T.E., Wittke J.H. and Hupé G.M. (2011). Northwest Africa 6704: a unique cumulate permafic achondrite containing sodic feldspar, awaruite and "fluid" inclusions, with an oxygen isotopic composition in the acapulcoite-lodranite field. *74th Annual Meteoritical Society Meeting*, #5231.

Jaffey, A. H., Flynn, K. F., Glendenin, L. E., Bentley, W. C., and Essling, A. M. (1971). Precision measurement of half-lives and specific activities of ^{235}U and ^{238}U: *Physical Review Series C,* v. 4. doi, 10*,* 1889–1906.

Jagoutz, E., Palme, H., Baddenhausen, H., Blum, K., Cendales, M., Dreibus, G., Spettel, B., Lorenz, V., and Wänke, H. (1979). The abundances of major, minor and trace elements in the earth's mantle as derived from primitive ultramafic nodules. *In Lunar and Planetary Science Conference Proceedings* (Vol. 10, pp. 2031–2050).

Jambon, A., Humayun, M., and Barrat, J. A. (2012). Northwest Africa 6693: a unique achondritic cumulate. *In Lunar and Planetary Science Conference Proceedings* (Vol. 43, #2099).

Jarosewich E. (1971) Chemical analysis of the Murchison Meteorite. *Meteoritics.* **6***,* 49–52.

Jarosewich E., Clarke Jr R. S., and Barrows J. N. (1987). Allende meteorite reference sample. *Smithsonian Contributions to the Earth Sciences,* 1–49.

Jenniskens P., Fries M. D., Yin Q. Z., Zolensky M., Krot A. N., Sandford S. A., Sears D., Beauford R., Ebel D. S., Friedrich J. M., Nagashima K., Wimpenny J., Yamakawa A., Nishiizumi K., Hamajima Y., Caffee M. W., Welten K. C., Laubenstein M., K. Davis A. M., Simon S. B., Heck P. R., Young E. D., Kohl I. E., Thiemens M. H., Nunn M. H., Mikouchi T., Hagiya K., Ohsumi K., Cahill T. A., Lawton J. A, Barnes D., Steele A., Rochette P., Verosub K. L., Gattacceca J., Cooper G., Glavin D. P., Burton A. S., Dworkin J. P., Elsila J. E., Pizzarello S., Ogliore R., Schmitt-Kopplin P., Harir M., Hertkorn N., Verchovsky A., Grady M., Nagao K., Okazaki R., Takechi H., Hiroi T., Smith K., Silber E. A., Brown P. G., Albers J., Klotz D., Hankey M., Matson R., Fries J. A., Walker R. J., Puchtel I., Lee C. A., Erdman M. E., Eppich G. R., Roeske S., Gabelica Z., Lerche M., Nuevo M., Girten B., and Worden S. P. (2012). Radar-enabled recovery of the Sutter's Mill meteorite, a carbonaceous chondrite regolith breccia. *Science*, **338,** 1583-1587.

Jessberger, E. K., Christoforidis, A., and Kissel, J. (1988). Aspects of the major element composition of Halley's dust. *Nature,* **332**, 691–695.

Jochum K. P., Weis U., Schwager B., Stoll B., Wilson S. A., Haug G. H., Andreae M. O., and Enzwiler J. (2015). Reference values following ISO guidelines for frequently requested rock reference materials. *Geostandards Geoanal. Res*. **40,** 333–350.

Keil, K. (2014). Brachinite meteorites: Partial melt residues from an FeO-rich asteroid. *Chemie der Erde-Geochemistry*, **74**, 311–329.

Keil K., and McCoy T. J. (in press) Acapulcoite-lodranite meteorites: ultramafic asteroidal partial melt residues. Chemie der Erde-Geochemistry, https://doi.org/10.1016/j.chemer.2017. 04.004.

Kennedy, A. K., Lofgren, G. E., and Wasserburg, G. J. (1993). An experimental study of trace element partitioning between olivine, orthopyroxene and melt in chondrules: equilibrium values and kinetic effects. *Earth and Planetary Science Letters*, **115**, 177–195.

Kimura, K., Lewis, R.S., and Anders, E. (1974). Distribution of gold and rhenium between nickel– iron and silicate melts: implications for the abundance of siderophile elements on the Earth and Moon. *Geochim. Cosmochim. Acta,* **38**, 683–701.

Kleine, T., Mezger, K., Münker, C., Palme, H., and Bischoff, A. (2004). 182 Hf-182 W isotope systematics of chondrites, eucrites, and martian meteorites: Chronology of core formation and early mantle differentiation in Vesta and Mars. *Geochim. Cosmochim. Acta*, **68**, 2935–2946.

Kööp L., Davis A. M., Nakashima D., Park C., Krot A. N., Nagashima K., Tenner T. J., Heck P. R. and Kita N. T. (2016). A link between oxygen, calcium and titanium isotopes in ^{26}Al-poor hibonite-rich CAIs from Murchison and implications for the heterogeneity of dust reservoirs in the solar nebula. *Geochim. Cosmochim. Acta.,* **189**, 70–95.

Kon Y., and Hirata T. (2015). Determination of 10 major and 34 trace elements in 34 GSJ geochemical reference samples using femtosecond laser ablation ICP-MS. *Geochem. J.* **49,** 351–375.

Kretz R. (1966). Interpretation of the shape of mineral grains in metamorphic rocks. *J. Petrol*. **7**, 68–94.

Kruijer T. S., Burkhardt C., Budde G., and Kleine T. (2017). Age of Jupiter inferred from the distinct genetics and formation times of meteorites. *Proc. Natl. Acad. Sci.* **114**, 6712–6716.

Kuehner, S. M., Irving, A. J., (2007). Grain boundary glasses in plutonic angrite NWA 4590: evidence for rapid decompressive partial melting and cooling on Mercury? In 38th *Lunar and Planetary Science Conference*, #1522 (abstract).

Lai Y. J., Henshall T., Cook D. L., Fehr M. A., and Schönbächler M. (2017). The Abundance of ^{92}Nb in the Early Solar System, in *Goldschmidt 2017 conference*, Paris, France, 13 to 18 August 2017.

Larsen K. K., Trinquier A., Paton C., Schiller M., Wielandt D., Ivanova M. A., Connelly J. N., Nordlund A, Krot A. N., and Bizzarro M. (2011). Evidence for magnesium isotope hetero- geneity in the solar protoplanetary disk. *Astrophys. J. Lett*. **735**, 37–44.

Larsen K. K., Wielandt D., Schiller M., and Bizzarro M. (2016). Chromatographic speciation of Cr (III)-species, inter-species equilibrium isotope fractionation and improved chemical purification strategies for high-precision isotope analysis. *Journal of Chromatography A,* **1443,** 162–174.

Larsen K. K., Wielandt D., and Bizzarro, M. (2018). Multi-element ion-exchange chromatography and high-precision MC-ICP-MS isotope analysis of Mg and Ti from sub-mm-sized meteorite inclusions. *Journal of Analytical Atomic Spectrometry*, **33**, 613–628.

Larimer J. W. (1979). The condensation and fractionation of refractory lithophile elements. *Icarus,* **40**, 446–454.

Laubier, M., Grove, T. L., and Langmuir, C. H. (2014). Trace element mineral/melt partitioning for basaltic and basaltic andesitic melts: An experimental and laser ICP-MS study with application to the oxidation state of mantle source regions. *Earth and Planetary Science Letters*, **392**, 265–278.

Le Corre, L., Reddy, V., Cloutis, E. A., Mann, P., Buchanan, P. C., Gabelica, Z., Hupé, G., and Gaffey, M. J. (2014). Identifying Parent Asteroid of Ungrouped Achondrite Northwest Africa 6704: Lessons from Dawn at Vesta. *Lunar Planet. Sci. XLV,* Lunar Planet. Inst., Houston. #1311 (abstract).

Leya, I., Wieler, R., and Halliday, A. N. (2001, March). The influence of cosmic-ray production on extinct nuclide systems. New results from improved model calculations. In *Lunar and Planetary Science Conference* (Vol. 32).

Leya, I., Schönbächler, M., Wiechert, U., Krähenbühl, U., and Halliday, A. N. (2007). High precision titanium isotope measurements on geological samples by high resolution MC-ICPMS. *International Journal of Mass Spectrometry,* **262**, 247–255.

Leya I., Schonbachler M. Wiechert U., Krahenbuhl U., and Halliday A. N. (2008). Titanium isotopes and the radial heterogeneity of the solar system. *Earth Planet. Sci. Lett.* **266,** 233–244.

Leya I., Schönbächler M., Krähenbühl U., and Halliday A. N. (2009). New titanium isotope data for Allende and Efremovka CAIs. *The Astrophysical Journal,* **702**, 1118–1126.

Liccardo, V., Malheiro, M., Hussein, M. S., and Frederico, T. (2018). Nuclear processes in Astrophysics: Recent progress. *arXiv preprint arXiv:1805.10183*.

Lindsley, D. H., and Andersen, D. J. (1983). A two-pyroxene thermometer. *Journal of Geophysical Research: Solid Earth*, **88**.

Lodders, K. (2003) Solar system abundances and condensation temperatures of the elements. *Astrophysical Journal,* **591**, 1220–1247.

Lofgren, G. E. (1980). Experimental studies on the dynamic crystallization of silicate melts, In *Physics of Magmatic Process*, edited by R. B. Hargrave, *Princeton University Press*, Princeton, pp.487–551.

Ludwig, K. R. (2001). Users Manual for Isoplot/Ex version 2.47. A geochronological toolkit for Microsoft Excel. *Berkeley Geochronology Center Special Publication* 1a, 55pp.

Lugaro, M., Pignatari, M., Ott, U., Zuber, K., Travaglio, C., Gyürky, G., and Fülöp, Z. (2016). Origin of the p-process radionuclides ^{92}Nb and ^{146}Sm in the early solar system and inferences on the birth of the Sun. *Proc. Natl. Acad. Sci. U.S.A.* **113**, 907–912.

Lugaro, M., Ott, U., and Kereszturi, Á. (2018). Radioactive nuclei from cosmochronology to habitability. *Progress in Particle and Nuclear Physics*.

Lugmair G. W. and Shukolyukov A. (1998). Early solar system timescales according to ^{53}Mn-^{53}Cr systematics. *Geochimica et Cosmochimica Acta*, **62**, 2863–2886.

Lyons, J. R., and Young, E. D. (2005). CO self-shielding as the origin of oxygen isotope anomalies in the early solar nebula. *Nature*, **435**, 317–320.

Makishima, A., and Nakamura, E. (2006). Determination of Major, Minor and Trace Elements in Silicate Samples by ICP-QMS and ICP-SFMS Applying Isotope Dilution-Internal Standardisation (ID-IS) and Multi-Stage Internal Standardisation. *Geostandards Geoanal. Res.* **30**, 245–271.

Mann, U., Frost, D. J., Rubie, D. C., Becker, H., and Audétat, A. (2012). Partitioning of Ru, Rh, Pd, Re, Ir and Pt between liquid metal and silicate at high pressures and temperatures- Implications for the origin of highly siderophile element concentrations in the Earth's mantle. *Geochim. Cosmochim. Acta,* **84**, 593–613.

Mason, B. (1967). Meteorites. *American Scientist*, **55**, 429–455.

Mattinson, J. M. (2010). Analysis of the relative decay constants of ^{235}U and ^{238}U by multi-step CA-TIMS measurements of closed-system natural zircon samples. *Chemical Geology*, **275**, 186–198.

McCoy, T. J., Keil, K., Clayton, R. N., and Mayeda, T. K. (1993). Classificational parameters for acapulcoites and lodranites: The cases of FRO 90011, EET 84302 and ALH A81187/84190. *Lunar Planet. Sci. XXIV,* Lunar Planet. Inst., Houston. #945 (abstract).

McCoy, T. J., Keil, K., Clayton, R. N., Mayeda, T. K., Bogard, D. D., Garrison, D. H., Huss, G. R., Hutcheon, I. D., and Wieler, R. (1996). A petrologic, chemical, and isotopic study of Monument Draw and comparison with other acapulcoites: Evidence for formation by incipient partial melting. *Geochim. Cosmochim. Acta*, **60**, 2681–2708.

McCoy T. J., Mittlefehldt D. W., and Wilson L. (2006). Asteroid differentiation. In *Meteorites in the Early Solar System II* (D. S. Lauretta and H. Y. McSween Jr., eds.), Univ. of Arizona, Tucson.

McSween, H. Y. (1987). Aqueous alteration in carbonaceous chondrites: Mass balance constraints on matrix mineralogy. *Geochim. Cosmochim. Acta,* **51**, 2469–2477.

McKeegan, K. D., & Davis, A. M. (2003). Early solar system chronology. *Treatise on Geochemistry*, **1**, 711.

Meyer B. S. (2003) Neutrinos, supernovae, molybdenum, and extinct ^{92}Nb. *Nucl. Phys. A* **719**, 13–20.

Mezger, K., Debaille, V., & Kleine, T. (2013). Core formation and mantle differentiation on Mars. *Space science reviews*, **174**, 27-48.

Mittlefehldt, D. W., Lindstrom, M. M., Bogard, D. D., Garrison, D. H., and Field, S. W. (1996). Acapulco-and Lodran-like achondrites: Petrology, geochemistry, chronology, and origin. *Geochim. Cosmochim. Acta*, **60**, 867–882.

Mittlefehldt D. W., McCoy T. J., Goodrich C. A., and Kracher A. (1998). Non-chondritic meteorites from asteroidal bodies. *In Planetary Materials, vol. 36 (ed. J. J. Papike). Rev. Mineralogy*, pp. 4-1–4-195.

Mikouchi, T., McKay, G. A., Miyamoto, M., and Sugiyama, K. (2011, November). Olivine Xenocrysts in Quenched Angrites: The First" Differentiated" Materials in the Solar System?. In *Workshop on Formation of the First Solids in the Solar System* (Vol. 1639, p. 9142).

Minster, J. F., and Allegre, C. J. (1982). The isotopic composition of zirconium in terrestrial and extraterrestrial samples: implications for extinct ^{92}Nb. *Geochim. Cosmochim. Acta,* **46**, 565–573.

Morgan, J. W., Higuchi, H., Takahashi, H., and Hertogen, J. (1978) A “chondritic” eucrite parent body: Inference from trace elements. *Geochimica et Cosmochimica Acta***,** **42**, 27–38.

Münker, C., Weyer, S., Mezger, K., Rehkämper, M., Wombacher, F., and Bischoff, A. (2000). ^{92}Nb-^{92}Zr and the early differentiation history of planetary bodies. *Science,* **289**, 1538–1542.

Münker, C., Weyer, S., Scherer, E., and Mezger, K. (2001). Separation of high field strength elements (Nb, Ta, Zr, Hf) and Lu from rock samples for MC‐ICPMS measurements. *Geochemistry, Geophysics, Geosystems*, **2**.

Münker, C., Fonseca, R. O., and Schulz, T. (2017). Silicate Earth's missing niobium may have been sequestered into asteroidal cores. *Nature Geoscience*, **10,** 822.

Newsom, H.E. (1990). Accretion and core formation in the Earth: evidence from siderophile elements. In *Origin of the Earth* (eds. H.E. Newsom and J.H. Jones) *Oxford Univ. Press, New York*, pp. 273–288.

Newton, J., Franchi, I. A., and Pillinger, C. T. (2000). The oxygen isotopic record in enstatite meteorites. *Meteoritics and Planetary Science*, **35**, 689–698.

O'Neill H.S.C., Dingwell D.B., Borisov A., Spettel B., and Palme H. (1995). Experimental petrochemistry of some highly sidero- phile elements at high temperatures, and some implications for core formation and the mantle's early history. *Chem. Geol.* **120**, 255–273.

Ouellette, N., Desch, S. J., Bizzarro, M., Boss, A. P., Ciesla, F., and Meyer, B. (2009). Injection mechanisms of short-lived radionuclides and their homogenization. *Geochim. Cosmochim. Acta,* **73,** 4946-4962.

Ozawa, K. (1984). Olivine-spinel geospeedometry: Analysis of diffusion-controlled Mg-Fe^{2+} exchange. *Geochim. Cosmochim. Acta,* **48**, 2597-2611.

Pack, A., Tanaka, R., Hering, M., Sengupta, S., Peters, S., and Nakamura, E. (2016). The oxygen isotope composition of San Carlos olivine on the VSMOW2-SLAP2 scale. *Rapid Communications in Mass Spectrometry*, **30**, 1495–1504.

Palme, H. (1981). Abundances of the elements in the solar system. *Astronomy and astrophysics*, 257–272.

Palme, H., and Beer, H. (1993). Abundances of the elements in the Solar System. *In Landolt Bornstein, group VI: astronomy and astrophysics* (ed. H. H. Voigt), vol. 3, pp. 196–221. Springer.

Palme, H. (2000). Are there chemical gradients in the inner Solar System? *Space Sci. Rev.* **92**, 237–264.

Palme, H., and O'Neill, H. (2014). Cosmochemical Estimates of Mantle Composition. Planets, Asteriods, Comets and The Solar System, Volume 2 of *Treatise on Geochemistry*. Edited by Andrew M. Davis.

Papish, O., Nordhaus, J., and Soker, N. (2015). A call for a paradigm shift from neutrino-driven to jet-driven core-collapse supernova mechanisms. *Monthly Notices of the Royal Astronomical Society*, **448**, 2362–2367.

Petitat, M., Birck, J. L., Luu, T. H., and Gounelle, M. (2011). The chromium isotopic composition of the ungrouped carbonaceous chondrite Tagish Lake. *The Astrophysical Journal*, **736**, 23.

Pan, K. C., Ricker, P. M., and Taam, R. E. (2012). Impact of type Ia supernova ejecta on binary companions in the single-degenerate scenario. *The Astrophysical Journal,* **750,** 151.

Prinz, M., Waggoner, D. G., and Hamilton, P. J. (1980). Winonaites: A primitive achondritic group related to silicate inclusions in IAB irons, *Lunar Planet. Sci. XI,* Lunar Planet. Inst., Houston. pp. 902–904 (abstract).

Prinz, M., Nehru, C. E., Delaney, J. S., and Weisberg, M. (1983). Silicates in IAB and IIICD Irons, Winonaites, Lodranites an Brachina: a Primitive and Modified-Primitive Group. *Lunar Planet. Sci. XIV,* Lunar Planet. Inst., Houston. pp. 616–617 (abstract).

Puchtel, I. S., Humayun, M., Campbell, A. J., Sproule, R. A., and Lesher, C. M. (2004). Platinum group element geochemistry of komatiites from the Alexo and Pyke Hill areas, Ontario, Canada. *Geochim. Cosmochim. Acta* **68**, 1361–1383.

Puchtel, I. S., Humayun, M., and Walker, R. J. (2007). Os–Pb–Nd isotope and highly siderophile and lithophile trace element systematics of komatiitic rocks from the

Volotsk suite, SE Baltic Shield. *Precambrian Res.* **158**, 119–137.

Qin, L., Alexander, C. M. O' D., Carlson, R. W., Horan, M. F., and Yokoyama, T. (2010a). Contributions to chromium isotope variations of meteorites. *Geochim. Cosmochim. Acta.,* **74**, 1122-1145.

Qin, L., Rumble, D., Alexander, C. M. O. D., Carlson, R. W., Jenniskens, P., and Shaddad, M. H. (2010b). The chromium isotopic composition of Almahata Sitta. *Meteorit Planet Sci.,* **45**, 1771−1777.

Qin, L., Nittler, L. R., Alexander, C. O. D., Wang, J., Stadermann, F. J., and Carlson, R. W. (2011). Extreme ^{54}Cr-rich nano-oxides in the CI chondrite Orgueil–Implication for a late supernova injection into the solar system. *Geochim. Cosmochim. Acta,* **75**, 629–644.

Rankenburg, K., Humayun, M., Brandon, A. D., and Herrin, J. S. (2008). Highly siderophile elements in ureilites. *Geochim. Cosmochim. Acta,* **72**, 4642–4659.

Rauscher, T., Dauphas, N., Dillmann, I., Fröhlich, C., Fülöp, Z., and Gyürky, G. (2013). Constraining the astrophysical origin of the p-nuclei through nuclear physics and meteoritic data. *Reports on Progress in Physics*, **76,** 066201.

Rehkämper M., and Halliday, A. N. (1997). Development and application of new ion-exchange techniques for the separation of the platinum group and other siderophile elements from geological samples. *Talanta,* **44**, 663–672.

Rehkämper, M., Schönbächler, M., and Stirling, C. H. (2001). Multiple collector ICP-MS: introduction to instrumentation, measurement technique and analytical capabilities. *Geostand. Newsl*. **25**, 23–40.

Reinhard, C. T., Planavsky, N. J., Wang, X., Fischer, W. W., Johnson, T. M., and Lyons, T. W. (2014) The isotopic composition of authigenic chromium in anoxic marine sediments: A case study from the Cariaco Basin. *Earth and Planetary Science Letters,*

407, 9–18.

Riches, A. J. V., Day, J. M. D., Walker, R. J., Simonetti, A., Liu, Y., Neal, C. R., and Taylor, L. A. (2012). Rhenium–osmium isotope and highly-siderophile-element abundance sys- tematics of angrite meteorites. *Earth Planet. Sci. Lett.* **353–354**, 208–218.

Righter, K., and Neff, K. E. (2007). Temperature and oxygen fugacity constraints on CK and R chondrites and implications for water and oxidation in the early solar system. *Polar Science,* **1**, 25–44.

Ringwood, A. E. (1961). Chemical and genetic relationships among meteorites. *Geochim. Cosmochim. Acta*, **24**, 159–197.

Rosman, K. J. R. and Taylor, P. D. P. (1998) Isotopic compositions of the elements 1997 (Technical Report). Pure and Applied Chemistry, **70**, 217–235.

Rubin, A. E. (2006). Shock, post-shock annealing, and post-annealing shock in ureilites. *Meteoritics and Planetary Science*, **41,** 125–133.

Rubin, A. E. (2007). Petrogenesis of acapulcoites and lodranites: A shock-melting model. *Geochim. Cosmochim. Acta*, **71**, 2383–2401.

Rubin, A. E. (2011). Origin of the differences in refractory-lithophile-element abundances among chondrite groups. *Icarus*, **213**, 547–558.

Russell, W. A., Papanastassiou, D. A., and Tombrello, T. A. (1978). Ca isotope fractionation on the Earth and other solar system materials. *Geochim. Cosmochim. Acta*, **42**, 1075–1090.

Sanborn M. E., Yin Q.-Z., and Irving A. J. (2014). Isotope forensics utilizing $\Delta^{17}O$-$\varepsilon^{54}Cr$ systematics provide supporting evidence for differentiated bodies overlain by chondritic veneers: A case for the CR parent body. *Lunar Planet. Sci. XLV,* Lunar

Planet. Inst., Houston. #2032 (abstract).

Sanborn, M. E., and Yin, Q. Z. (2015). Investigating a Common Source for Brachinites and Graves Nunataks 06128 and 06129 Meteorites Using High Precision Chromium Isotopes. *Lunar Planet. Sci. XLVI,* Lunar Planet. Inst., Houston. #2241 (abstract).

Sanborn M. E., Wimpenny J., Williams C. D., Yamakawa A., Amelin Y., Irving A. J., and Yin Q.-Z. (2017). Carbonaceous achondrites Northwest Africa 6704/6693: New anchors for early solar system chronology and genealogy. Submitted to *Geochim. Cosmochim. Acta*.

Sanborn M. E., Wimpenny J., Williams C. D., Yamakawa A., Amelin Y., Irving A. J., and Yin Q.-Z. (2019) Carbonaceous Achondrites Northwest Africa 6704/6693: Milestones for Early Solar System Chronology and Genealogy. *Geochim. Cosmochim. Acta,* in press, https://doi.org/10.1016/j.gca.2018.10.004

Sanloup, C., Blichert-Toft, J., Télouk, P., Gillet, P., and Albarède, F. (2000). Zr isotope anomalies in chondrites and the presence of 92Nb in the early solar system. *Earth and Planetary Science Letters*, **184**, 7581.

Schatz, H., Aprahamian, A., Görres, J., Wiescher, M., Rauscher, T., Rembges, J. F., Thielemann, F. K., Pfeifferc, B., Möller, P., Kratz, K. L., Herndl, H., Brown B. A., and Rebel, H. (1998). rp-Process nucleosynthesis at extreme temperature and density conditions. *Physics reports*, **294**, 167-263.

Schiller M., Handler M. R., and Baker J. A. (2010a) High-precision Mg isotopic systematics of bulk chondrites. *Earth Planet. Sci. Lett.* **297**, 165–173.

Schiller, M., Van Kooten, E., Holst, J. C., Olsen, M. B., and Bizzarro, M. (2014). Precise measurement of chromium isotopes by MC-ICPMS. *Journal of analytical atomic spectrometry*, **29**, 1406–1416.

Schiller M., Connelly J. N., Glad A. C., Mikouchi T., and Bizzarro M. (2015) Early

accretion of protoplanets inferred from a reduced inner solar system 26Al inventory. *Earth Planet. Sci. Lett.* **420**, 45–54.

Schmitz B., Yin Q.-Z., Sanborn M. E., Tassinari M., Caplan C., and Huss G. (2016). A new type of solar-system material recovered from Ordovician marine limestone. *Nature Communications*, **7**, 11851.

Schönbächler, M., Rehkämper, M., Halliday, A. N., Lee, D. C., Bourot-Denise, M., Zanda, B., Hattendorf, B., and Günther, D. (2002). Niobium-zirconium chronometry and early solar system development. *Science*, **295**, 1705–1708.

Schönbächler, M., Lee, D.-C., Rehkämper, M., Halliday, A.N., Fehr, A., Hattendorf, B., and Günther, D. (2003). Zirconium isotope evidence for incomplete admixing of *r*-process components in the solar nebula. *Earth Planet. Sci. Lett.* **216**, 467–481.

Schönbächler, M., Rehkämper, M., Lee, D.-C., and Halliday, A.N. (2004). Ion exchange chromatography and high precision isotopic measurements of zirconium by MC-ICP-MS. *Analyst* **129**, 32–37.

Schönbächler, M., Lee, D.-C., Rehkämper, M., Halliday, A.N., Hattendorf, B., and Günther, D. (2005). Nb/Zr fractionation on the Moon and the search for extinct ^{92}Nb. *Geochim. Cosmochim. Acta* **69**, 775–785.

Schoenberg R., Zink S., Staubwasser M., and von Blanckenburg F. (2008). The stable Cr isotope inventory of solid Earth reservoirs determined by double spike MC-ICP-MS. *Chemical Geology*, **249**, 294–306.

Schoenberg, R., Merdian, A., Holmden, C., Kleinhanns, I. C., Haßler, K., Wille, M., and Reitter, E. (2016). The stable Cr isotopic compositions of chondrites and silicate planetary reservoirs. *Geochim. Cosmochim. Acta*, **183**, 14–30.

Schrader, D. L., Franchi, I. A., Connolly, H. C., Greenwood, R. C., Lauretta, D. S., and Gibson, J. M. (2011). The formation and alteration of the Renazzo-like carbonaceous

chondrites I: Implications of bulk-oxygen isotopic composition. *Geochim. Cosmochim. Acta*, **75**, 308–325.

Schramm, L. S., Brownlee, D. E., and Wheelock, M. M. (1989). Major element composition of stratospheric micrometeorites. *Meteoritics,* **24,** 99–112.

Schulze, H., Bischoff, A., Palme, H., Spettel, B., Dreibus, G., and Otto, J. (1994). Mineralogy and chemistry of Rumuruti: The first meteorite fall of the new R chondrite group. *Meteoritics and Planetary Science,* **29**, 275–286.

Schwartz, A. J., Kumar, M., Adams, B. L., and Field, D. P. (Eds.). (2009). *Electron backscatter diffraction in materials science* (Vol. 2). New York: Springer.

Scott, E. R., Greenwood, R. C., Franchi, I. A., and Sanders, I. S. (2009). Oxygen isotopic constraints on the origin and parent bodies of eucrites, diogenites, and howardites. *Geochim. Cosmochim. Acta*, **73**, 5835–5853.

Sharp, Z. D. (1990). A laser-based microanalytical method for the in situ determination of oxygen isotope ratios of silicates and oxides. *Geochim. Cosmochim. Acta*, **54**, 1353–1357.

Shields W. R., Murphy T. J., Catanzaro E. J. and Garner E. L. (1966) Absolute isotopic abundance ratios and the atomic weight of a reference sample of chromium. *Journal of Research of the National Bureau of Standards*, **70,** 193–197.

Shirey S. B., and Walker R. J. (1995). Carius tube digestion for low blank rhenium-osmium analysis. *Anal. Chem.* **67**, 2136–2141.

Shukolyukov, A., and Lugmair, G. W. (2006a). Manganese–chromium isotope systematics of carbonaceous chondrites. *Earth Planet. Sci. Lett.* **250**, 200–213.

Shukolyukov, A., and Lugmair G. W. (2006b). The Mn–Cr isotope systematics in the ureilites Kenna and LEW85440, *Lunar Planet. Sci. XXXVII,* Lunar Planet. Inst.,

Houston. #1478 (abstract).

Shukolyukov, A., Lugmair, G. W., and Irving, A. J. (2009). Mn-Cr isotope systematics of angrite northwest Africa 4801. *Lunar Planet. Sci. XL,* Lunar Planet. Inst., Houston. #1381 (abstract).

Shukolyukov, A., Lugmair, G. W., and Irving, A. J. (2011). Mn-Cr isotope systematics and excess of ^{54}Cr in metachondrite Northwest Africa 3133. *Lunar Planet. Sci. XLII,* Lunar Planet. Inst., Houston. #1527 (abstract).

Spitz, A. H., and Boynton, W. V. (1991). Trace element analysis of ureilites: new constraints on their petrogenesis. *Geochim. Cosmochim. Acta*, **55**, 3417–3430.

Spivak-Birndorf L., Wadhwa M., and Janney P. (2009). ^{26}Al-^{26}Mg systematics in D'Orbigny and Sahara 99555 angrites: Implica- tions for high-resolution chronology using extinct chronome- ters. *Geochim. Cosmochim. Acta* **73**, 5202–5211.

Srinivasan, G., Ulyanov, A. A., and Goswami, J. N. (1994). Ca-41 in the early solar system. *The Astrophysical Journal*, **431**, L67-L70.

Sugiura N. and Fujiya W. (2014). Correlated accretion ages and ε^{54}Cr of meteorite parent bodies and the evolution of the solar nebula. Meteoritics & Planetary Science, 49, 772–787.

Tachibana, S., and Huss, G. R. (2003). The initial abundance of 60Fe in the solar system. *The Astrophysical Journal Letters*, **588**, L41.

Takagi Y., Noguchi T., Kimura M., and Yamaguchi A. (2014). Crystallization and subsolidus processes of the NWA 6704 ungrouped achondrite. *Japan Geoscience Union Meeting 2014*, Japan Geoscience Union, Yokohama. #PPS22-P03 (abstract)

Takigawa, A., Miki, J., Tachibana, S., Huss, G. R., Tominaga, N., Umeda, H., and Nomoto, K. (2008). Injection of short-lived radionuclides into the early solar system

from a faint supernova with mixing fallback. *The Astrophysical Journal*, **688,** 1382.

Tanaka, R., and Nakamura, E. (2013). Determination of ^{17}O-excess of terrestrial silicate/oxide minerals with respect to Vienna Standard Mean Ocean Water (VSMOW). *Rapid Communications in Mass Spectrometry*, **27**, 285–297.

Terashima S., Taniguchi M., Mikoshiba M. and Imai N. (1998). Preparation of two new GSJ geochemical reference materials: basalt JB-1b and coal fly ash JCFA-1. *Geostandards Geoanal. Res.* **22**, 113–117.

Tiepolo, M., Bottazzi, P., Foley, S. F., Oberti, R., Vannucci, R., and Zanetti, A. (2001). Fractionation of Nb and Ta from Zr and Hf at mantle depths: the role of titanian pargasite and kaersutite. *Journal of Petrology*, 42, 221-232.

Thielemann, F. K., Arcones, A., Käppeli, R., Liebendörfer, M., Rauscher, T., Winteler, C., Fröhlich, C. Dillmann, I. Fischer, T. Martinez-Pinedo, G. Langanke K. Farouqid K. Kratz K.-L. Panov I. and Langanke, I. K. (2011). What are the astrophysical sites for the r-process and the production of heavy elements?. *Progress in Particle and Nuclear Physics*, **66**, 346-353.

Tomeoka, K., and Buseck, P. R. (1985). Indicators of aqueous alteration in CM carbonaceous chondrites: Microtextures of a layered mineral containing Fe, S, O and Ni. *Geochim. Cosmochimica Acta,* **49**, 2149–2163.

Touboul M., Kleine T., Bourdon B., Van Orman J. A., Maden C., and Zipfel J. (2009). Hf–W thermochronometry: II. Accretion and thermal history of the acapulcoite–lodranite parent body. *Earth and Planetary Science Letters*, **284**, 168–178.

Travaglio, C., Röpke, F. K., Gallino, R., and Hillebrandt, W. (2011). Type Ia supernovae as sites of the p-process: two-dimensional models coupled to nucleosynthesis. *The Astrophysical Journal*, **739,** 93.

Travaglio C., Gallino R., Rauscher T., Dauphas N., Röpke F. K., and Hillebrandt W.

(2014). Radiogenic p-isotopes from Type Ia supernova, nuclear physics uncertainties, and galactic chemical evolution compared with values in primitive meteorites. *Astrophys. J.* **795**, 141

Trinquier A., Birck J-.L., and Allègre C. (2007). Widespread ^{54}Cr heterogeneity in the inner solar system. *Astrophysical Journal,* **655**, 1179–1185.

Trinquier, A., Birck, J. L., and Allègre, C. J. (2008a). High-precision analysis of chromium isotopes in terrestrial and meteorite samples by thermal ionization mass spectrometry. *Journal of Analytical Atomic Spectrometry*, **23**, 1565–1574.

Trinquier A., Birck J.-L., Allègre C. J., Göpel C., and Ulfbeck D. (2008b). ^{53}Mn-^{53}Cr systematics of the early Solar System revisited. *Geochim. Cosmochim. Acta,* **72**, 5146–5163.

Trinquier A., Elliott T., Ulfbeck D., Coath C., Krot A. N., and Bizzarro M. (2009). Origin of nucleosynthetic isotope heterogeneity in the solar protoplanetary disk. *Science,* **324**, 374–376.

Tsuchiyama, A. (1986). Experimental-study of olivine-melt reaction and its petrological implications, *Journal of Volcanology and Geothermal Research*, **29**, 245–264.

Ueda T., Yamashita K., and Kita N. (2006) Chromium isotopic systematics of ureilite. *NIPR Sympos. Antarct. Meteorit.* XXX, 117–118 (abstr.).

Van Kooten, E. M., Wielandt, D., Schiller, M., Nagashima, K., Thomen, A., Larsen, K. K., Olsen, M. B., Nordlund, A., Krot, A. N., and Bizzarro, M. (2016). Isotopic evidence for primordial molecular cloud material in metal-rich carbonaceous chondrites. *Proceedings of the National Academy of Sciences*, **113**, 2011–2016.

Vernon, R. H. (1968). Microstructures of high-grade metamorphic rocks at Broken Hill, Australia. *Journal of Petrology,* **9**, 1–22.

Vernon, R. H. (1970). Comparative grain-boundary studies of some basic and ultrabasic

granulites, nodules and cumulates. *Scottish Journal of Geology,* **6**, 337–351.

Vetere, F., Iezzi, G., Behrens, H., Holtz, F., Ventura, G., Misiti, V., Cavallo, A., Mollo, S., and Dietrich, M. (2015). Glass forming ability and crystallisation behaviour of sub-alkaline silicate melts. *Earth-Science Reviews*, **150**, 25–44.

Wadhwa, M., Amelin, Y., Bogdanovski, O., Shukolyukov, A., Lugmair, G. W., and Janney, P. (2009). Ancient relative and absolute ages for a basaltic meteorite: Implications for timescales of planetesimal accretion and differentiation. *Geochimica et Cosmochimica Acta*, **73**, 5189–5201.

Walton, E. L., and Herd, C. D. (2007). Dynamic crystallization of shock melts in Allan Hills 77005: implications for melt pocket formation in Martian meteorites. *Geochim. Cosmochim. Acta*, **71**, 5267–5285.

Walker, R. J., Storey, M., Kerr, A. C., Tarney, J., and Arndt, N. T. (1999). Implication of ^{187}Os isotopic heterogeneities in a mantle plume: evidence from Gorgona Island and Curacao. *Geochim. Cosmochim. Acta,* **63**, 713–728.

Walker, R. J., Horan, M. F., Morgan, J. W., Becker, H., Grossman, J. N., and Rubin, A. (2002). Comparative ^{187}Re–^{187}Os systematics of chondrites: Implications regarding early solar system processes. *Geochim. Cosmochim. Acta,* **66**, 4187–4201.

Walsh, K. J., Morbidelli, A., Raymond, S. N., O'brien, D. P., and Mandell, A. M. (2011). A low mass for Mars from Jupiter/'s early gas-driven migration. *Nature,* **475**, 206–209.

Wanajo, S. (2006). The rp-process in neutrino-driven winds. *The Astrophysical Journal*, **647,** 1323.

Wang X., Planavsky N. J., Reinhard C. T., Zou H., Ague J. J., Wu Y., Gill B. C., Schwarzenbach E. M., P., and eucker-Ehrenbrink, B. (2016). Chromium isotope fractionation during subduction-related metamorphism, black shale weathering, and hydrothermal alteration. *Chemical Geology*, **423**, 19–33.

Warren, P. H., Ulff-Møller, F., Huber, H., and Kallemeyn, G. W. (2006). Siderophile geochemistry of ureilites: a record of early stages of planetesimal core formation. *Geochimica et Cosmochimica Acta*, **70**, 2104–2126.

Warren, P. H., and Rubin, A. E. (2010). Pyroxene-selective impact smelting in ureilites. *Geochim. Cosmochim. Acta*, **74**, 5109–5133.

Warren P. H. (2011). Stable-isotopic anomalies and the accretionary assmlage of the Earth and Mars: A subordinate role for carbonaceous chondrites. *Earth Planet. Sci. Lett.* **311**, 93–100.

Warren P. H., Rubin A. E., Isa J., Brittenham S., Ahn I., and Choi B.-G. (2013). Northwest Africa 6693: A new type of FeO-rich, low-$\Delta^{17}O$, poikilitic cumulate achondrite. *Geochim. Cosmochim. Acta,* **107**, 135–154.

Wasserburg, G. J., Busso, M., and Gallino, R. (1996). Abundances of actinides and short-lived nonactinides in the interstellar medium: diverse supernova sources for the r-processes. *The Astrophysical Journal Letters*, **466**, L109.

Wasson, J. T., and Kallemeyn, G. W. (1988). Compositions of chondrites. Philosophical Transactions of the Royal Society of London A: *Mathematical, Physical and Engineering Sciences*, **325**, 535–544.

Wasserburg, G. J., Busso, M., and Gallino, R. (1996). Abundances of actinides and short-lived nonactinides in the interstellar medium: diverse supernova sources for the r-processes. *The Astrophysical Journal Letters*, ***466***, L109.

Wasserburg, G. J., Wimpenny, J., & YIN, Q. Z. (2012). Mg isotopic heterogeneity, Al-Mg isochrons, and canonical $^{26}Al/^{27}Al$ in the early solar system. *Meteoritics & Planetary Science*, **47,** 1980-1997.

Weisberg, M. K., McCoy, T. J., and Krot, A. N., (2006). *Systematics and evaluation of meteorite classification*, In, *Meteorites and the Early Solar System II*, edited by D. S. Lauretta and H. Y. McSween Jr, University of Arizona Press, Tucson, pp.19–52.

Weiss, B. P., and Elkins-Tanton, L. T. (2013). Differentiated planetesimals and the parent bodies of chondrites. *Annual Review of Earth and Planetary Sciences*, **41,** 529–560.

Welsch, B., Faure, F., Famin, V., Baronnet, A., and Bachèlery, P. (2012). Dendritic crystallization: A single process for all the textures of olivine in basalts?. *Journal of Petrology*, egs077.

Wiechert, U., Halliday, A. N., Lee, D. C., Snyder, G. A., Taylor, L. A., and Rumble, D. (2001). Oxygen isotopes and the Moon-forming giant impact. *Science*, **294,** 345–348.

Wiechert, U. H., Halliday, A. N., Palme, H., and Rumble, D. (2004). Oxygen isotope evidence for rapid mixing of the HED meteorite parent body. *Earth and Planetary Science Letters*, **221**, 373–382.

Wiik, H. B. (1972). The chemical composition of the Haverö meteorite and the genesis of the ureilites. *Meteoritics,* **7**, 553–558.

Wombacher, F., and Rehkämper, M. (2003). Investigation of the mass discrimination of multiple collector ICP-MS using neodymium isotopes and the generalised power law. *Journal of Analytical Atomic Spectrometry*, **18**, 1371–1375.

Wombacher F., Eisenhauer A., Heuser A., and Weyer S. (2009). Separation of Mg, Ca and Fe from geological reference materials for stable isotope ratio analyses by MC-ICP-MS and double-spike TIMS. *Journal of Analytical Atomic Spectrometry,* **24**, 627–636.

Woosley, S., and Howard, W. (1978). The p-process in supernovae. *Astrophys J* 36:285–304

Woosley, S. E., Hartmann, D. H., Hoffman, R. D., and Haxton, W. C. (1990). The nu-process. *The Astrophysical Journal*, **356,** 272–301.

Woosley, S. E., and Hoffman, R. D. (1992). The alpha-process and the r-process. *The Astrophysical Journal*, **395,** 202–239.

Yamaguchi, A., Barrat, J. A., Greenwood, R. C., Shirai, N., Okamoto, C., Setoyanagi, T., Ebihara, M., Franchi, I.A., Bohn, M., (2009). Crustal partial melting on Vesta: evidence from highly metamorphosed eucrites. *Geochim. Cosmochim. Acta* **73**, 7162–7182.

Yamakawa, A., Yamashita, K., Makishima, A., and Nakamura, E. (2009). Chemical separation and mass spectrometry of Cr, Fe, Ni, Zn, and Cu in terrestrial and extraterrestrial materials using thermal ionization mass spectrometry. *Anal. Chem.,* **81,** 9787–9794.

Yamakawa, A., Yamashita, K., Makishima, A., and Nakamura, E. (2010). Chromium isotope systematics of achondrites: Chronology and isotopic heterogeneity of the inner solar system bodies. *The Astrophysical Journal,* **720**, 150–154.

Yamashita, K., Ueda, T., Nakamura, N., Kita, N. and Heaman, L. M. (2005). Chromium isotopic study of mesosiderite and ureilite: evidence for ε^{54}Cr deficit in differentiated meteorites. *NIPR Symposium Antarctic Meteorite*, **29**, 100–101.

Yamashita, K., Maruyama, S., Yamakawa, A., and Nakamura, E. (2010). ^{53}Mn-^{53}Cr chronometry of CB chondrite: evidence for uniform distribution of ^{53}Mn in the early solar system. *The Astrophysical Journal*, **723**, 20–24.

Yang, G., Zimmerman, A., Stein, H., and Hannah, J. (2015). Pretreatment of nitric acid with hydrogen peroxide reduces total procedural Os blank to femtogram levels. *Analytical chemistry*, **87**, 7017–7021.

Yin, Q. Z., Jacobsen, S. B., McDonough, W. F., Horn, I., Petaev, M. I., and Zipfel, J. (2000). Supernova sources and the ^{92}Nb-^{92}Zr p-process chronometer. The *Astrophysical Journal Letters,* **536**, L49.

Yin Q.-Z., Yamashita K., Yamakawa A., Tanaka R., Jacobsen B., Ebel D., Hutcheon I. D. and Nakamura E. (2009) ^{53}Mn–^{53}Cr systematics of Allende chondrules and $\varepsilon^{54}Cr$–$\Delta^{17}O$ correlation in bulk carbonaceous chondrites. *Lunar Planet. Sci.* **40**, #2006 (abstr.).

Yokoyama, T., Fukami, Y., Okui, W., Ito, N., and Yamazaki, H. (2015). Nucleosynthetic strontium isotope anomalies in carbonaceous chondrites. *Earth and Planetary Science Letters,* **416**, 46–55.

Yokoyama, T., and Walker, R. J. (2016). Nucleosynthetic isotope variations of siderophile and chalcophile elements in the Solar System. *Reviews in Mineralogy and Geochemistry*, **81**, 107–160.

Young, E. D., and Galy, A. (2004) The isotope geochemistry and cosmochemistry of magnesium. *Rev. Mineral. Geochem.* **55**, 197–230.

Young, E. D. (2014). Inheritance of solar short-and long-lived radionuclides from molecular clouds and the unexceptional nature of the solar system. *Earth and Planetary Science Letters*, **392,** 16–27.

Yurimoto, H., and Kuramoto, K. (2004). Molecular cloud origin for the oxygen isotope heterogeneity in the solar system. *Science*, **305,** 1763–1766.

Zhang, J., Dauphas, N., Davis, A. M., and Pourmand, A. (2011). A new method for MC-ICPMS measurement of titanium isotopic composition: Identification of correlated isotope anomalies in meteorites. *Journal of Analytical Atomic Spectrometry,* **26**, 2197–2205.

Zhang, J., Dauphas, N., Davis, A. M., Leya, I., and Fedkin, A. (2012). The proto-Earth as a significant source of lunar material. *Nature Geoscience,* **5**, 251–255.